

الجمهورية الجزائرية الديمقراطية الشعبية  
République Algérienne Démocratique et Populaire  
وزارة التعليم العالي و البحث العلمي

Ministère de l'enseignement supérieur et de la recherche scientifique  
Université Mohamed Khider – Biskra  
Faculté des Sciences et de la Technologie  
Département de Génie Civil et Hydraulique  
Référence :.....

جامعة محمد خيضر - بسكرة  
كلية العلوم و التكنولوجيا  
قسم الهندسة المدنية و الري  
المرجع:.....

Thèse de Doctorat  
Spécialité: Génie Civil  
Option: Matériaux de Construction

---

# Élaboration et caractérisation des structures stratifiées/sandwich, matrice organique/ renfort fibreux.

---

Présentée par

***Amina MASMOUDI***

Soutenue publiquement le :

11/06/2025

Devant le jury composé de :

Nom et prénom	Grade	Etablissement d'affiliation	Désignation
Mr. Abdelouahab TATI	Professeur	University of Biskra	Président
Mr. Ahmed BOUAZIZ	Professeur	Univeristé de Biskra	Directeur de thèse
Mr. Abdelhak KHECHAI	MCA	Univeristé de Biskra	Co-Directeur de thèse
Mr. Mohamed Ouejdi BELARBI	Professeur	University of Biskra	Examineur
Mr. Fares Mohamed Laid REKBI	MRA	Centre de recherche en technologies industrielles - CRTI	Examineur

الجمهورية الجزائرية الديمقراطية الشعبية  
République Algérienne Démocratique et Populaire  
وزارة التعليم العالي و البحث العلمي

Ministère de l'enseignement supérieur et de la recherche scientifique  
Université Mohamed Khider – Biskra  
Faculté des Sciences et de la Technologie  
Département de Génie Civil et Hydraulique  
Référence :.....

جامعة محمد خيضر - بسكرة  
كلية العلوم و التكنولوجيا  
قسم الهندسة المدنية و الري  
المرجع:.....

Thesis presented with a view to obtaining  
Doctorate in Civil Engineering  
Option: CONSTRUCTION MATERIALS

---

## **Elaboration and characterization of laminated/sandwich structures, organic matrix/fibrous reinforcement**

---

Presented by:

***Amina MASMOUDI***

Defended publicly on:

11/06/2025

**The jury composed of:**

<b>First and last name</b>	<b>Grade</b>	<b>Institution of affiliation</b>	<b>Designation</b>
Mr. Abdelouahab TATI	Professor	University of Biskra	President
Mr. Ahmed BOUAZIZ	Professor	University of Biskra	Supervisor
Mr. Abdelhak KHECHAI	MCA	University of Biskra	Co-Supervisor
Mr. Mohamed Ouejdi BELARBI	Professor	University of Biskra	Examiner
Mr. Fares Mohamed Laid REKBI	MRA	Research Center in Industrial Technologies, CRTI	Examiner

*To my beloved parents*

*To my brothers*

*To my friends and colleagues*

*...To ME.*

# ACKNOWLEDGMENTS

---

To start, praise and thanks be to ALLAH Almighty who blessed me with a such journey. Thank you, ALLAH, for the patience, the power and the courage you gave me to start and finish my childhood dream.

My parents, *Mohamed and Rachida*, thank you for always believing in me. I cannot find the words to describe my gratitude for you. My dream would not be completed without your strength, sacrifice and support. You have been always the guide in my life, ALLAH bless you. Also, I would like to thank my brothers *Nassim* and *Toufik* for their patience and support. My source of strength was and will be always my family.

I would like to express my gratitude to my supervisor, *Pr. Ahmed BOUAZIZ*, for his guidance, feedback, and support throughout this journey. I extend my thanks to my co-supervisor, *Dr. Abdelhak KHECHAI*, for his valuable input, encouragement, and advice.

I would like to thank *Pr. Abdelouahab TATI* and *Pr. Mohamed Ouejdi BELARBI*, from university of Biskra, and *Dr. Fares Mohamed Laid REKBI* from Research Centre in Industrial Technologies -CRTI- for their interest in this work by accepting to be examiners and jury members.

I would like to express my appreciation for the LRGC laboratory; its previous director *Pr. GUETTALA Abdelhamid* and current director *Pr. MABROUKI Abdelhak*, as well, *Mrs. SAIDI Warda* who was very helpful. Also, many thanks to all the Doctors and professors of the Civil Engineering department. My thanks extend to my PhD colleagues for their feedbacks and help in every way. I would like to acknowledge the staff of Laboratory of Mechanical Engineering for their help and guidance.

A special acknowledgment to *Pr. Said TAIBI* and the LOMC laboratory at Le Havre, France, for kindly accepting me to work in their laboratory. I am grateful for the opportunity to work with such a distinguished team, and I truly appreciate the valuable assistance and support provided.

A sweet friendship refreshes the soul. My heartfelt thanks go to my dearest friends; *Hana, Imane, Assia*, and *Aicha* for their unwavering support. I deeply appreciate your time, patience, and constant presence in my life. A special note of gratitude to *Dr. Afaf ZEROUAL*, whose



support was truly invaluable. This journey would not have been as smooth without her care, help and encouragement. I am profoundly thankful for the paths that led to our friendship.

I appreciate those who believed in me, as well as those who brought difficulties to my way, you made the achievement even more satisfying.

*Amina MASMOUDI.*

"لا يزال المرء عالماً ما دام في طلب العلم،

فإذا ظن أنه قد علم، فقد جهل."

# Abstract

---

Sandwich structures have become indispensable in modern engineering applications due to their exceptional strength-to-weight ratio and capacity to combine materials that enhance each other's structural performance. By combining high-stiffness outer face sheets with low-density core materials, these structures provide enhanced flexural rigidity and load-bearing capacity while maintaining minimal weight. Polyurethane (PU) and polystyrene (PS) foams are prevalent core choices, prized for their excellent thermal insulation and manufacturability. However, their mechanical response under both static and cyclic loading is significantly influenced by core density and cellular microstructure, necessitating further investigation. This thesis investigates the mechanical performance of sandwich composite structures comprising glass fiber reinforced polymer (GFRP) skins and polymeric foam cores, alongside innovative hybrid cores incorporating embedded reinforcing pins. A comprehensive experimental analysis was carried out to characterize the structural response of these sandwich composites including flatwise and edgewise compression tests, shear testing, and both static and cyclic three-point bending tests. Digital Image Correlation (DIC) was employed to obtain full-field strain measurements, while Scanning Electron Microscopy (SEM) was used to analyze failure mechanisms and evaluate the quality of fiber–matrix adhesion and skin–core bonding. The results of tests revealed that sandwich structure with foam core, PU and PS, almost responded similarly in edgewise and flatwise compression loadings. A combination of failure modes was detected. The incorporation of reinforced pins enhances key mechanical properties, including core shear stress, shear modulus, and flexural stiffness.

## Keywords

Panel Elaboration, Sandwich Structure, Laminated Structures, Mechanical Behavior, Digital Image Correlation (DIC).

أصبحت الهياكل الساندويتشية مكونا لا غنى عنه في التطبيقات الهندسية، نظرا لنسبة القوة الى الوزن الاستثنائية وقدرتها على دمج مواد تعزز الأداء الهيكلي لبعضها البعض. من خلال دمج صفائح خارجية عالية الصلابة مع أنوية خفيفة الوزن، تُحقق هذه الهياكل صلابة محسنة وقدرة أكبر على تحمل الأحمال مع الحفاظ على وزن منخفض. تُستخدم رغوات البولي يوريثان (PU) والبوليستيرين (PS) عادةً كأنوية لما تتمتع به من خصائص عزل حراري وسهولة في المعالجة. ومع ذلك، فإن أداءها الميكانيكي تحت الأحمال الساكنة والدورية يتأثر بكثافة النواة وبنية الخلايا، مما يستدعي مزيداً من البحث. تهدف هذه الأطروحة إلى دراسة الأداء الميكانيكي لهياكل الساندويتش المركبة التي تتكون من صفائح البوليمر المقوى بالألياف الزجاجية (GFRP) ونوى الرغوة البوليمرية، بالإضافة إلى أنوية هجينة مبتكرة تحتوي على دعائم تقوية مدمجة. تم إجراء برنامج تجريبي شامل لتقييم الاستجابة الإنشائية لهذه التكوينات الساندويتشية. وقد شمل البرنامج اختبارات الضغط المسطح والجانبية، واختبارات القص، إلى جانب اختبارات الانحناء ثلاثي النقاط في كل من الحالات الساكنة والدورية. تم استخدام تقنية ارتباط الصور الرقمية (DIC) لقياس التشوهات، كما تم تحليل آليات الفشل وتقييم جودة الالتصاق بين الألياف والمصفوفة، وكذلك بين الأوجه والنواة، باستخدام المجهر الإلكتروني الماسح (SEM). كشفت النتائج أن الهياكل الساندويتشية ذات أنوية رغوية أظهرت استجابات ميكانيكية عند إخضاعها لتجارب الضغط الجانبي و المصطح، مع ملاحظة مجموعة مختلفة من أنماط الفشل. أما إضافة الدعائم المقواة فقد عززت الخصائص الميكانيكية الرئيسية، بما في ذلك إجهاد القص للنواة، معامل القص وكذلك صلابة الإنحناء.

### الكلمات المفتاحية

تصنيع الألواح، الهياكل الساندويتشية، هياكل متعددة الطبقات، السلوك الميكانيكي، ارتباط الصور الرقمية.

# Résumé

---

Les structures sandwich sont devenues indispensables dans les applications d'ingénierie modernes en raison de leur excellent rapport résistance/poids et de leur capacité à associer des matériaux dont les propriétés mécaniques se complètent. En combinant des peaux externes à haute rigidité avec des âmes à faible densité, ces structures offrent une rigidité en flexion accrue et une capacité portante améliorée, tout en conservant un poids minimal. Les mousses de polyuréthane (PU) et de polystyrène (PS) sont des choix d'âme habituels, appréciés pour leurs excellentes propriétés d'isolation thermique et leur facilité de mise en œuvre. Cependant, leur comportement mécanique sous chargements statique et cyclique est fortement influencé par la densité d'âme et la microstructure cellulaire, ce qui nécessite des investigations approfondies. Cette thèse étudie les performances mécaniques de structures composites sandwich composées de peaux en polymère renforcé de fibres de verre (GFRP) et d'âmes en mousse polymère, ainsi que d'âme hybride innovant intégrant des connecteurs renforcés. Une analyse expérimentale complète a été menée afin de caractériser le comportement structural de ces composites sandwich, incluant des essais de compression à plat et sur chant, des essais de cisaillement, ainsi que des essais de flexion trois points en régime statique et cyclique. La corrélation d'images numériques (DIC) a été utilisée pour obtenir des mesures de déformation en champ complet, tandis que la microscopie électronique à balayage (MEB) a permis d'analyser les mécanismes de rupture et d'évaluer la qualité de l'adhésion fibre–matrice et de l'interface peau–âme. Les résultats des essais ont montré que les structures sandwich avec un cœur en mousse, PU ou PS, présentent un comportement similaire sous chargement en compression. Une combinaison de modes de rupture a été observée. L'incorporation des connecteurs renforcés améliore les propriétés mécaniques clés, notamment la contrainte de cisaillement de l'âme, le module de cisaillement et la rigidité en flexion.

## MOTS-CLES :

Élaboration des panneaux, Structure sandwich, Structures stratifiées, Comportement mécanique, Corrélation d'images numériques (DIC)

# Content

---

<b>ACKNOWLEDGMENTS .....</b>	<b>i</b>
<b>Abstract .....</b>	<b>iv</b>
<b>ملخص.....</b>	<b>v</b>
<b>Résumé .....</b>	<b>vi</b>
<b>LIST OF FIGURES .....</b>	<b>x</b>
<b>LIST OF TABLES .....</b>	<b>xiv</b>
<b>LIST OF ABBREVIATIONS AND SYMBOLS .....</b>	<b>xv</b>
<b>GENERAL INTRODUCTION .....</b>	<b>1</b>
<b>CHAPTER 01. LITERATURE REVIEW .....</b>	<b>4</b>
1.1 Introduction .....	4
1.2 Composite Materials .....	5
1.2.1 Identification and Classification of Composite Materials .....	6
1.2.2 Glass fiber reinforcement .....	11
1.3 Glass fiber reinforced polymers (GFRP) .....	13
1.3.1 Manufacturing of GFRP Composites .....	14
1.3.2 Applications of GFRP composites .....	17
1.4 Sandwich structures .....	23
1.4.1 Constituents of sandwich structure .....	26
1.4.2 Foam core .....	28
1.4.3 Hybrid core .....	36
1.4.4 Incorporation of GFRP in Sandwich Composites .....	40
1.5 Failure mode of sandwich structures .....	44
1.6 Application of digital image correlation for studying the behavior of materials .....	46
1.7 conclusion .....	48
<b>CHPTER 02. MATERIALS AND EXPERIMENTAL METHODS .....</b>	<b>49</b>
2.1 Introduction .....	49
2.2 Materials used .....	49
2.2.1 Skin .....	49
2.2.2 Core .....	53
2.3 Manufacturing of sandwich structure .....	55

2.3.1 Sandwich structure with PU and PS core (SPU and SPS) .....	55
2.3.2 Sandwich structure with hybrid core (SRP) .....	55
2.4 Digital image correlation .....	56
2.5 Mechanical testing .....	57
2.5.1 UP resin properties .....	57
2.5.2 GFRP mechanical testing .....	58
2.5.3 Mechanical testing of sandwich structures .....	61
2.6 Scanning electron microscopy .....	65
2.7 Conclusion .....	65
<b>CHAPTER 03. CHARACTERIZATION OF THE CONSTITUENTS OF SANDWICH STRUCTURES .....</b>	<b>67</b>
3.1 Introduction .....	67
3.2 UP resin .....	67
3.3 GFRP skin characterization .....	70
3.3.1 Tensile test .....	70
3.3.2 Compression test .....	72
3.3.3 Flexural test .....	75
3.4 Flatwise compression test of PU and PS foams .....	80
3.5 Conclusion .....	81
<b>CHAPTER 04. MECHANICAL BEHAVIOR OF SPU AND SPS .....</b>	<b>82</b>
4.1 Introduction .....	82
4.2 Edgewise compression test of SPU and SPS .....	82
4.3 Flatwise compression test of SPU and SPS .....	88
4.3 Shear test of SPS .....	93
4.4 Flexural test of SPS .....	96
4.5 Conclusion .....	99
<b>CHAPTER 05. MECHANICAL BEHAVIOR OF SRP .....</b>	<b>100</b>
5.1 Introduction .....	100
5.2 Shear test of SRP .....	100
5.2 Flexural test of SRP .....	103
5.4 Conclusion .....	109
<b>GENERAL CONCLUSION AND PERSPECTIVES .....</b>	<b>110</b>
General conclusion .....	110
Perspectives .....	111

<b>BIBLIOGRAPHY .....</b>	<b>113</b>
<b>LIST OF PUBLICATIONS AND COMMUNICATIONS .....</b>	<b>123</b>
<b>ANNEX. PRODUCT DATASHEETS OF THE MATERIALS USED .....</b>	<b>125</b>



# LIST OF FIGURES

<b>Figure 1. 1:</b> a) Composites, b) polymer composites, c) ceramic composites, d) metal composites, e) carbon composites, f) organic-inorganic hybrid materials, g and h) super molecular hybrid structure [11] .....	6
<b>Figure 1. 2:</b> Classification of composite materials. (a) Based on matrix materials and (b) based on reinforcement materials.[13] .....	7
<b>Figure 1. 3:</b> Shares (%) of thermoplastic and thermoset resins in the FRP industry. [16].....	8
<b>Figure 1. 4:</b> The application of FRP composites in various sectors [22] .....	10
<b>Figure 1. 5:</b> Types of glass fibers according form(a), long threaded (b), chopped (c) and finely chopped (d) fiber [27] .....	11
<b>Figure 1. 6:</b> Architectural Marvel in Basel, 1998: Structural Frames and Bolted Joints [31].	14
<b>Figure 1. 7:</b> Molding sequence: material loading, pressure forming, and part removal [27]..	15
<b>Figure 1. 8:</b> Illustration shows the process behind the open molding hand lay-up technique [36]. .....	16
<b>Figure 1. 9:</b> Schematic of the spray lay-up process [20].....	16
<b>Figure 1. 10:</b> Typical filament winding process [27].....	17
<b>Figure 1. 11:</b> Typical compressive stress vs. strain curves for HL-6, VL-6, and VH-6 samples[41] .....	18
<b>Figure 1. 12:</b> Typical stress-strain curves for the HL and VI samples [42].....	19
<b>Figure 1. 13:</b> Load v/s extension curve for (a) 90° (b) 45° and (c) 30°orientation[43]. .....	20
<b>Figure 1. 14:</b> Graphical representation of the mathematical models (a) Low Plate thin $e = 0.6$ mm, (b) Plate thin in center $e = 1.8$ mm, (c) High Plate thin $e = 3$ mm (a) [44].....	21
<b>Figure 1. 15:</b> Pile rehabilitation with GFRP composites, Load vs. shear strain rehabilitated specimen.[45] .....	22
<b>Figure 1. 16:</b> Front perspective and overall view of the footbridge taken at the Gdansk University of Technology campus [56].....	24
<b>Figure 1. 17:</b> Front view of specimen studied [57]. .....	25
<b>Figure 1. 18:</b> Schematic diagram of specimen and test setup [58].....	26
<b>Figure 1. 19:</b> Classification of sandwich structures based on core [61].....	27
<b>Figure 1. 20:</b> Different core structures in sandwich composites [55] .....	27
<b>Figure 1. 21:</b> Foam Synthesis Process: (a) Mixing Polyol and Isocyanate, (b) Hand-Homogenization, (c) Pouring into Mold with Expansion and Transverse Directions, (d) Final Expanded Foam [76]. .....	29
<b>Figure 1. 22:</b> Sandwich composites panel of glass fiber and polyurethane foam core (GFRP - PU) [77].....	29
<b>Figure 1. 23:</b> Experimental, simulated and theoretical load–deflection behavior of the composite sandwich panel [78] .....	30
<b>Figure 1. 24:</b> Applied force as a function of crosshead displacement for a four-point quarter-span loading test [80] .....	31
<b>Figure 1. 25:</b> Variation of compressive strength on type of rigid PUF in compression. [81].	32
<b>Figure 1. 26:</b> Three important forms of EPS. Beads formed via the expansion of resin are molded into the desired shape [89].....	33
<b>Figure 1. 27:</b> Road embankment with EPS-blocks at Passo del Brattello during the construction phase (2002) and at present (2019) [90]. .....	34
<b>Figure 1. 28:</b> Cement/polystyrene core and cement sheet facing sandwich panels [91].....	35

<b>Figure 1. 29:</b> Produced EPS core and reinforcement panel [92].	35
<b>Figure 1. 30:</b> a) Schematic of sandwich panel studied, b) Flexural behavior of FCS and PRFCS panels [94].	36
<b>Figure 1. 31:</b> Transverse bending behavior of empty and foam-filled sandwich beams with corrugated cores (short specimens e and E, with $L = 112$ mm; Table 1): (a) force versus displacement curve; and (b) photographs illustrating the deformation history and evolution of failure at selected points marked in (a) [96].	38
<b>Figure 1. 32:</b> Illustration of sandwich composite panel (a) and density of the reinforcement rods (15 and 30 mm) (b). [97].	39
<b>Figure 1. 33:</b> Stress–strain behavior of sandwich composites subjected to flexural loading: carbon face (a) and glass face (b) sandwich composites [97].	39
<b>Figure 1. 34:</b> Load-displacement curves of S4D with different GFRP layers on the compressive region. [106].	41
<b>Figure 1. 35:</b> GFRP-bamboo-wood sandwich specimen (a) schematic plot and (b) fabricated specimen. [107].	42
<b>Figure 1. 36:</b> Tensile strength of sandwich composite produced with different core[108].	42
<b>Figure 1. 37:</b> Comparison between test result and FEA result. (a) load displacement curve, (b) load strain curve [109].	43
<b>Figure 1. 38:</b> Failure mechanisms of sandwich structure [60].	45
<b>Figure 1. 39:</b> DIC analysis of the final condition of the structure following damage tolerance testing [120].	47
<b>Figure 1. 40:</b> Distribution of Shear Strains on the Surface of (a) PET Foam Core (Airex T92.100), (b) PVC Foam Core (Airex C70.55), and (c) Balsa Core (Baltek SB.50) Sandwich Beams at Different Mid-Load Levels.	48
<b>Figure 2. 1:</b> E-glass CSM fibers a) 300g/m <sup>2</sup> , b) 600g/m <sup>2</sup> .	50
<b>Figure 2. 2:</b> a) Process of making GFRP plate, b) Molded GFRP plate.	51
<b>Figure 2. 3:</b> SEM of manufactured GFRP plate.	51
<b>Figure 2. 4:</b> a) sample of 2x2 mm for calcination, b) sample after calcination, c) fibers after calcination.	52
<b>Figure 2. 5:</b> a) Mold used for PU foam, b) Sample of PU foam.	53
<b>Figure 2. 6:</b> PS foam.	53
<b>Figure 2. 7:</b> Process of fabricating the GFRP pins.	54
<b>Figure 2. 8:</b> Sample of reinforced pin after calcination.	55
<b>Figure 2. 9:</b> GFRP skin, PU and PS foams.	55
<b>Figure 2. 10:</b> Position of reinforced Pins in SRP.	56
<b>Figure 2. 11:</b> Experimental setup for DIC analysis adopted, a) GFRP skin compression test, b) Flatwise compression for sandwich.	57
<b>Figure 2. 12:</b> a) Mold of silicone, b) Specimen, c) Specimen dimensions (in mm).	58
<b>Figure 2. 13:</b> Geometry of GFRP skin samples used for tensile test, dimensions are in mm.	59
<b>Figure 2. 14:</b> a) Geometry of GFRP skin samples used for compressive test, dimensions are in mm. b) Modified compression test fixture.	60
<b>Figure 2. 15:</b> a) Three-points test. b) Four-points test.	61
<b>Figure 2. 16:</b> a) Edgewise compression setup, b) S-60, c) S-200.	62
<b>Figure 2. 17:</b> Sandwich compressive setup for flatwise compression.	63
<b>Figure 2. 18:</b> Shear test setup.	64

<b>Figure 2. 19:</b> Flexure test fixture.....	65
<b>Figure 3. 1:</b> Stress strain curves of tensile test of UP resin [136] .....	68
<b>Figure 3. 2:</b> DIC engineering displacement and strain fields for tensile test of the specimens. [136] .....	69
<b>Figure 3. 3:</b> virtual extensometers to obtain: a) Transverse strain $\epsilon_t$ , b) Longitudinal strain $\epsilon_l$ . [136] .....	69
<b>Figure 3. 4:</b> Transverse strain-longitudinal strain curves for evaluating Poisson $\nu_{12}$ [136] .....	70
<b>Figure 3. 5:</b> a) Stress-strain curves for tensile test of GFRP skin. b) Specimens after tensile test.[137].....	71
<b>Figure 3. 6:</b> SEM of fracture surface of GFRP skin under tensile failure. [137] .....	71
<b>Figure 3. 7:</b> DIC engineering strain fields for tensile test of GFRP skin [137]. .....	72
<b>Figure 3. 8:</b> a) Stress-strain curves for compression test of GFRP skin. b) Specimens after compression test. ....	73
<b>Figure 3. 9:</b> SEM of fracture surface of GFRP skin under compressive failure. ....	74
<b>Figure 3. 10:</b> Region of interest studied in DIC and DIC engineering fields for compression test of GFRP skin. ....	74
<b>Figure 3. 11:</b> Three-point test a) Specimen after test. b) Load-displacement curves.....	76
<b>Figure 3. 12:</b> DIC engineering for Three-point bending of GFRP skin. ....	77
<b>Figure 3. 13:</b> a) Specimens after four-points flexural test, b) Load-displacement curves. ....	78
<b>Figure 3. 14:</b> SEM analysis of GFRP specimen after four-point bending. ....	79
<b>Figure 3. 15:</b> DIC engineering for Four-point bending of GFRP skin.....	79
<b>Figure 3. 16:</b> Comparison of four-point and three-point flexural strength and flexural modulus. ....	80
<b>Figure 3. 17:</b> Load-displacement curve of flatwise compression test; a) PU foam, b) PS foam .....	81
<b>Figure 4. 1:</b> Specimens after edgewise compression test for S-60: a) SPU, b) SPS. ....	84
<b>Figure 4. 2:</b> Edgewise compression load-displacement curves for SPU and SPS; S-60.....	84
<b>Figure 4. 3:</b> DIC engineering displacement and strain fields after edgewise compression test for S-60: a) SPU, b) SPS. ....	85
<b>Figure 4. 4:</b> Specimens after edgewise compression test for S-200; a) SPU, b) SPS. ....	86
<b>Figure 4. 5:</b> Edgewise compression load-displacement curves for SPU and SPS; S-200.....	86
<b>Figure 4. 6:</b> DIC engineering displacement and strain fields after edgewise compression test for S-200: a) SPU, b) SPS. ....	87
<b>Figure 4. 7:</b> Flatwise compression Load-Displacement curves.....	90
<b>Figure 4. 8:</b> Specimens after Flatwise compression test. ....	90
<b>Figure 4. 9:</b> SEM micrographs of SPU subjected to flatwise compression samples. ....	91
<b>Figure 4. 10:</b> SEM micrographs of SPS subjected to flatwise compression samples. ....	91
<b>Figure 4. 11:</b> DIC engineering displacement and strain fields for flatwise compression test of a) SPU, b) SPS .....	92
<b>Figure 4. 12:</b> Load-displacement curves for SPS specimens subjected to shear test. ....	94
<b>Figure 4. 13:</b> Samples after shear test of SPS .....	95
<b>Figure 4. 14:</b> DIC engineering displacement and strain fields of SPS after shear test. ....	95
<b>Figure 4. 15:</b> Load-displacement curves for SPS specimens subjected to static and cyclic bending tests. ....	96

<b>Figure 4. 16:</b> SPS specimen after test; a) S-L, b) C-L.....	97
<b>Figure 4. 17:</b> DIC analysis of vertical displacement of specimen; a) S-L, b) C-L.....	98
<b>Figure 5. 1:</b> Load-displacement curves for SPS and SRP subjected to shear test.....	101
<b>Figure 5. 2:</b> Comparison of $\tau_{\max}$ and G for SRP and SPS. ....	102
<b>Figure 5. 3:</b> SRP specimens after shear test. ....	102
<b>Figure 5. 4:</b> DIC engineering displacement and strain fields of SRP specimens under shear load.....	103
<b>Figure 5. 5:</b> Load-displacement curves for SRP specimens subjected to static and cyclic bending tests. ....	105
<b>Figure 5. 6:</b> a) SRP specimen after flexural test, b) Failure of reinforced pins. ....	105
<b>Figure 5. 7:</b> Load-displacement curves for SRP and SPS samples: a) Static loading, b) Cyclic loading.....	106
<b>Figure 5. 8:</b> Comparison of flexural Young's modulus of SRP and SPS. ....	106
<b>Figure 5. 9:</b> DIC engineering of vertical displacement of SRP subjected to cyclic flexural loading.....	107
<b>Figure 5. 10:</b> DIC engineering of strain fields of SRP. ....	108
<b>Figure 5. 11:</b> virtual extensometers to obtain vertical strain $\epsilon_y$ . ....	108
<b>Figure 5. 12:</b> The vertical strain evolution of SRP and SPS specimens under cyclic loading. ....	108

# LIST OF TABLES

---

<b>Table 1. 1:</b> Typical Composition and Properties of Glass Fibers [14] .....	12
<b>Table 1. 2</b> Research on the application of GFRP in Engineering Sectors. ....	22
<b>Table 1. 3</b> Summary of more research on sandwich panels with different hybrid core. ....	40
<b>Table 2.1</b> Fiber fraction for GFRP skins. ....	52
<b>Table 2. 2</b> Fiber content for reinforced pins. ....	54
<b>Table 2. 3</b> Dimensions of sandwich structure samples.....	65
<b>Table 3. 1</b> Mechanical parameters obtained through tensile test of GFRP skin.....	72
<b>Table 3. 2</b> Mechanical parameters obtained through compressive test of GFRP skin. ....	75
<b>Table 3. 3</b> Results obtained through three-point bending.....	76
<b>Table 3. 4</b> Results obtained through four-point bending .....	80
<b>Table 3. 5</b> Mechanical properties of PU and PS foams .....	81
<b>Table 4. 1</b> The results obtained through edgewise compression tests for SPU and SPS.....	88
<b>Table 4. 2</b> Mechanical parameters obtained through flatwise compressive test of SPU and SPS .....	93
<b>Table 4. 3</b> Mechanical parameters obtained through shear test of SPS.....	94
<b>Table 4. 4</b> Summary of main results from static and cyclic bending test for SPS specimens. ....	97
<b>Table 5. 1</b> Mechanical parameters obtained from shear test of SRP samples. ....	101
<b>Table 5. 2</b> Summary of main results from static and cyclic bending test for SRP specimens. ....	106

# LIST OF ABBREVIATIONS AND SYMBOLS

---

**EPS:** Expanded polystyrene.

**UP:** Unsaturated polyester.

**GFRP:** Glass fiber reinforced polymer.

**PU:** Polyurethane

**PS:** Polystyrene.

**CSM:** Chopped strand mat glass fiber.

**SPS:** Sandwich structure with PS foam core.

**SPU:** Sandwich structure with PU foam core.

**SRP:** sandwich structure with hybrid foam/reinforced pins.

**SPS-60:** Sandwich structure with PS foam core with 60 mm in width.

**SPS-200:** Sandwich structure with PS foam core with 200 mm in width.

**SPU-60:** Sandwich structure with PU foam core with 60 mm in width.

**SPS-200:** Sandwich structure with PU foam core with 200 mm in width.

**DIC:** Digital Image Correlation.

**SEM:** Scanning Electron Microscopy.

**S-L:** Static loading.

**C-L:** Cyclic loading.

$w_f$ : Weight of fiber.

$w$ : Specimen width.

$L$ : Specimen length.

$t_t$ : Total thickness of sandwich structure.

$t_c$ : Core thickness.

$t_s$ : Skin thickness.

$L'$ : Support span length for three-point flexural test

$L''$ : Outer support span length for four-point flexural test

$L'''$ : Inner support span length for four-point flexural test

$U$ : Horizontal displacement.

$V$ : vertical displacement.

$\epsilon_x$ : Strain along axis x.

$\epsilon_{xy}$ : Shear strain.

$\epsilon_y$ : Strain along axis y.

$E_t$ : Tensile young's modulus.

$E_c$ : Compressive young's modulus.

$E_f$ : Flexural young's modulus.

$\sigma_f$ : Flexural stress.

$\sigma_{EC}$ : Ultimate edgewise compression strength.

$\sigma_{fc}$ : Ultimate flatwise compression strength.

$\tau_{max}$ : Shear strength.

$G$ : Shear modulus.



# GENERAL INTRODUCTION

---

Sandwich structures belong to the category of multilayer panels, distinguished by their combination of materials with differing mechanical properties. These structures are designed to optimize mechanical performance, enhance rigidity, and improve load-bearing capacity by strategically distributing materials in alignment with stress patterns within the panel. A typical sandwich panel consists of two rigid outer skins bonded to a lightweight core with relatively low mechanical properties [1].

Composite materials have revolutionized numerous industries, and their adoption in civil engineering is rapidly expanding. Among these, Fiber-Reinforced Polymer (FRP) has played a pivotal role since its aerospace applications in World War II, marking a major advancement in lightweight structural design. By integrating a lightweight core between high-strength skins, sandwich panels achieve a significantly higher moment of inertia without added weight. The success of FRP sandwich panels in aerospace has spurred their use in civil engineering, enabling innovative applications such as facade systems, roofing solutions, and pedestrian bridges. These structures offer multiple advantages, including efficient prefabrication, which accelerates construction and reduces labor costs. Moreover, their durability and low maintenance enhance long-term cost-effectiveness, making them an increasingly attractive choice for modern infrastructure [2].

Among the various core materials used in sandwich structures, polyurethane (PU) and polystyrene (PS) foams are widely favored for their excellent thermal insulation and ease of processing. However, their mechanical performance, particularly under static and cyclic loading, is highly dependent on foam density and cell structure, necessitating further research to optimize these properties. To address these limitations, reinforced pins have been introduced as an effective solution for enhancing structural integrity. These pins serve as mechanical connectors, bridging the core-skin interface, a critical region susceptible to delamination under shear stresses. By anchoring the skins to the core, they strengthen the bond, reducing the risk of interfacial failure. Moreover, the pins create additional load-transfer pathways, promoting more uniform stress distribution across the structure.



## Thesis objectives

The thesis focuses on studying different configurations of sandwich panels and their mechanical behavior under various loading conditions. It aims to comprehensively analyze the mechanical performance of Glass Fiber Reinforced Polymer (GFRP) composites, including their strength, stiffness, and failure mechanisms, while investigating the influence of using cores such as polyurethane (PU) and polystyrene (PS). Additionally, the study aims to compare and evaluate the effect of incorporating reinforced pins into the foam core, examining how these mechanical connectors enhance load distribution, damage tolerance, and resistance to delamination under static, and cyclic loading scenarios.

The thesis is divided into five chapters; each contributing to the achievement of the stated objectives and aims.

- **Chapter 01** introduces an overview of fiber composite polymers and sandwich structures. It begins with a definition of these structures and their areas of application, followed by a discussion of their components, and finally, the damage mechanisms associated with these structures. Also, previous studies on FRP and sandwich structures have been reviewed.
- **Chapter 02** is dedicated to establishing a clear understanding of the experimental methodology adopted in this study. It provides a thorough and systematic description of the materials utilized and preparation processes. The chapter elaborates on the fabrication techniques for the GFR plates, PU foam, hybrid core, sandwich structures, and detailing the steps involved to ensure consistency and quality. Additionally, it describes the experimental procedures in depth, covering the mechanical testing methods used to assess properties such as compressive strength, shear strength, and flexural behavior. Furthermore, the techniques for scanning electron microscopy (SEM) analysis to evaluate microstructural features.
- **Chapter 03** provides an in-depth discussion of the detailed results obtained from the experimental characterization of the individual components of the sandwich structures. This includes an analysis of the UP resin, focusing on its mechanical properties, as well as the performance of the GFRP skin, highlighting its tensile, compressive and flexural strength and stiffness. Additionally, the chapter examines the compressive properties of the PU and PS foam cores. The findings from these characterizations form the

foundation for understanding the role of each component in the overall behavior and performance of the sandwich structures under various loading.

- **Chapter 04** presents a comprehensive analysis of the results obtained from the mechanical characterization of sandwich structures with PU and PS foam cores. These results are based on a series of tests conducted under various loading conditions, including edgewise compression, flatwise compression, shear, as well as static and cyclic flexural loading. Each test was designed to evaluate specific mechanical properties such as strength, stiffness, and failure modes under different stress conditions.
- **Chapter 05** focuses on the mechanical behavior of the sandwich structure with hybrid core/reinforced pins (SRP) under various loading conditions. The study examines the performance of this configuration when subjected to shear loading and analyzing the effect of hybrid reinforced core on shear properties. Furthermore, the chapter examines the structural response under both static and cyclic flexural loading, characterizing the specimen's stiffness degradation, load-bearing capacity, and failure modes under each loading regime.

Finalizing the thesis with a conclusion and future perspectives of the study.

***CHAPTER 01***  
**LITERATURE**  
**REVIEW**

# CHAPTER 01. LITERATURE REVIEW

---

## 1.1 Introduction

Sandwich structures are extensively used as structural materials across a wide range of industries, including aerospace, automotive, marine, and civil engineering applications. Their growing adoption is primarily attributed to their exceptional strength-to-weight ratio, high corrosion resistance, and long-term durability, which make them particularly suitable for load-bearing components where weight savings are critical. The fundamental design of sandwich structures, comprising two thin, high-strength face sheets bonded to a thick, lightweight core, enables efficient load distribution and enhanced structural performance. The face sheets are primarily responsible for carrying in-plane tensile and compressive loads, while the core resists transverse shear forces and prevents the face sheets from buckling [3]. This configuration results in a structure that offers excellent stiffness and strength under compressive, tensile, flexural, and buckling conditions, all while maintaining a relatively low overall density. Furthermore, sandwich composites provide excellent energy absorption and thermal insulation characteristics, which further expand their usefulness in multifunctional applications [4].

The incorporation of Fiber Reinforced Polymers (FRPs) as face sheets in sandwich structures has significantly advanced the performance and application range of these composites. Reinforcing materials, such as glass fiber, carbon fiber and Kevlar fibers offer high specific strength and stiffness, excellent fatigue resistance, and superior corrosion behavior compared to traditional materials like metals or wood. When used as the outer skins in sandwich panels, FRPs enhance the structural capacity to withstand in-plane and out-of-plane loads, particularly in flexure and impact scenarios, while maintaining a lightweight profile [5,6].

The core of a sandwich composite is a critical component that significantly influences the overall mechanical and functional performance of the structure. It provides both insulation properties and mechanical strength, including compressive and shear resistance to the structure [7,8]. Among various core configurations, foam cores are the most commonly utilized due to their favorable balance of weight and performance. In addition to foam, numerous alternative core designs have been investigated such as truss, honeycomb and corrugated cores, as well as more advanced concepts like bioinspired, hybrid, and folded cores [2].

This chapter examines the design, development, and application of sandwich composite structures, with a particular emphasis on fiber-reinforced polymers (FRPs). Special focus is given to glass fiber-reinforced polymer (GFRP) face sheets combined with polymeric foam core materials, such as polyurethane (PU) and polystyrene (PS). In addition, recent advancements in innovative hybrid foam cores for enhanced sandwich performance are also discussed.

## 1.2 Composite Materials

A brief definition would be that composite materials are multi-phase mixtures of two or more distinct components, each with unique properties and forms, combined through various compounding processes. These materials retain the essential properties of their original components while also exhibiting enhanced characteristics that are not present in any of the individual constituents on their own.[9] Generally, composite materials exhibit the following characteristics: Microscopically, composite materials are non-homogeneous and have distinct interfaces. The performance of their component materials differs significantly, leading to a substantial improvement in the overall performance of the composite. Typically, the volume fraction of the component materials exceeds 10%. According to this definition, a wide range of materials, such as straw-mud walls, steel-reinforced concrete, and tire cords, fall under the category of composite materials [10]. A composite material consists of multiple phases, primarily involving a matrix material and a reinforcing material. The matrix, which forms the continuous phase, can be categorized into metal matrix composites, inorganic non-metallic matrix composites, or polymer matrix composites, based on the type of matrix used *Fig.1.1* [11]. The reinforcing material, which constitutes the dispersed phase, often includes fibrous materials like glass fibers, organic fibers, and others. The matrix not only ensures even distribution of applied loads but also transfers them to the fibers. Moreover, certain properties of composite materials are significantly affected by the matrix material's characteristics. Hence, the overall performance of composite materials is directly linked to the properties of the fibers, the matrix, and the interface between them [12].

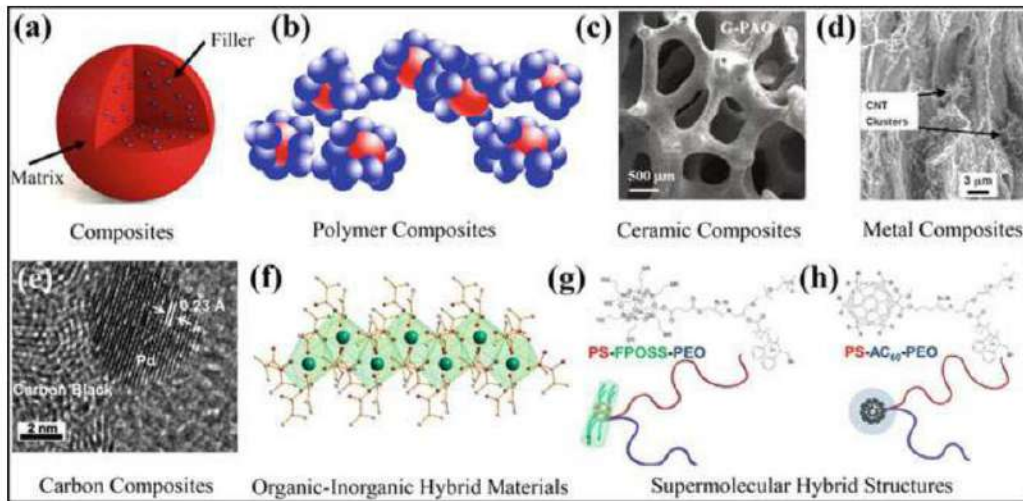


**Figure 1. 1:** *a) Composites, b) polymer composites, c) ceramic composites, d) metal composites, e) carbon composites, f) organic-inorganic hybrid materials, g and h) super molecular hybrid structure [11].*

### 1.2.1 Identification and Classification of Composite Materials

In general, composite materials can be summarized into three main categories commonly used across a wide range of engineering applications: polymer matrix composites (PMCs), metal matrix composites (MMCs), and ceramic matrix composites (CMCs). Based on the type of reinforcement, composites are further categorized into particulate composites, fiber-reinforced composites, and structural composites [13]. These two classification systems are shown in *Fig1.2*.

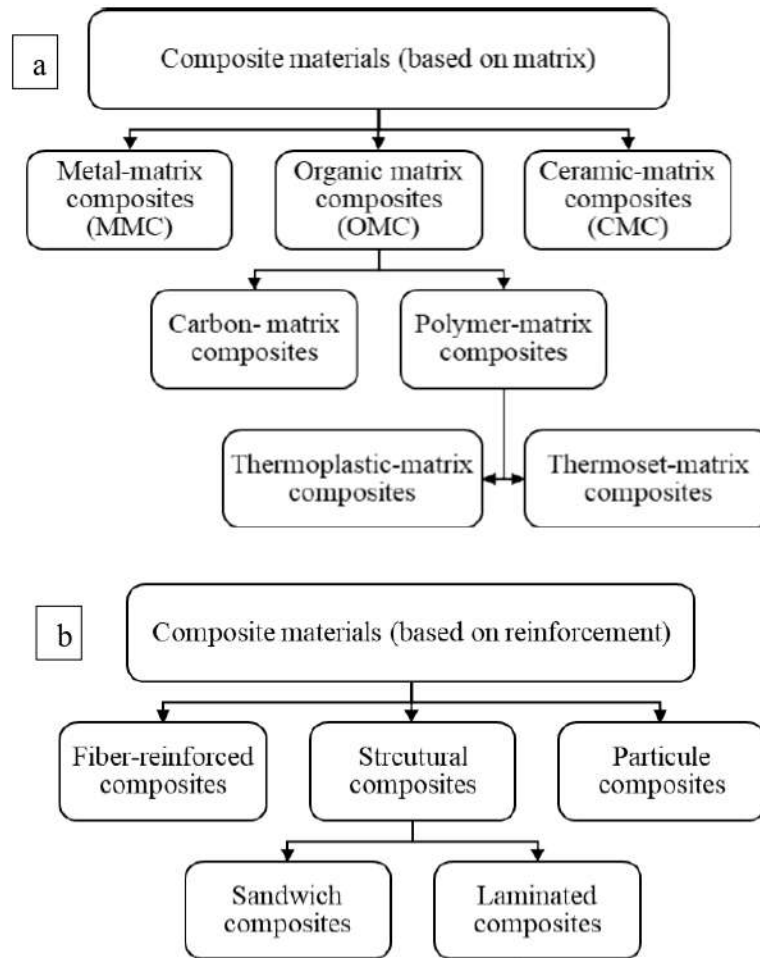


**Figure 1. 2:** Classification of composite materials. (a) Based on matrix materials and (b) based on reinforcement materials [13].

### 1.2.1.1 Classification Based on Matrix

- **Polymer Matrix Composites (PMC)**

PMCs consist a polymer resin matrix reinforced with fibers. Including reinforcing fibers enhances the stiffness and strength of polymer matrix composites. Polymers used as matrix materials are classified into thermosets and thermoplastics. The primary concern when selecting a matrix is its maximum service temperature. As temperature increases, the strength and elastic properties of polymers decrease. Above this temperature, polymers are expected to lose some stiffness and strength. However, advancements have led to the development of polymers with enhanced high-temperature properties that can rival various metals. Moisture sensitivity is another crucial factor in selecting polymer matrices, as water absorption by resins can reduce stiffness and strength, leading to dimensional changes [11,14]. Thermosetting polymers are extensively used in structural applications due to their superior resistance to chemicals and



corrosive environments, outperforming thermoplastics in many cases. The selection of a specific resin is influenced by various factors, including cost, design requirements, and manufacturing constraints. Among thermosets, epoxy resins are particularly important in aerospace applications for their excellent structural and thermal properties, functioning effectively up to 200 °C. Other commonly used thermosetting resins include polyimides, which operate between 250–290 °C and are suitable for extreme environments, along with vinyl esters, phenolics, bismaleimides, polyesters, cyanate esters, and benzoxazines. Continuous research aims to improve their high-temperature capabilities. In contrast, thermoplastic polymers are appreciated for their versatility and unique biological and mechanical properties, with their absorption and desorption behavior highly dependent on temperature. Thermoplastics are generally classified into three categories: amorphous, crystalline, and liquid crystalline. Examples of amorphous thermoplastics include polystyrene, polycarbonate, and ABS, while crystalline thermoplastics include PEEK, nylon, and polypropylene [14,15].

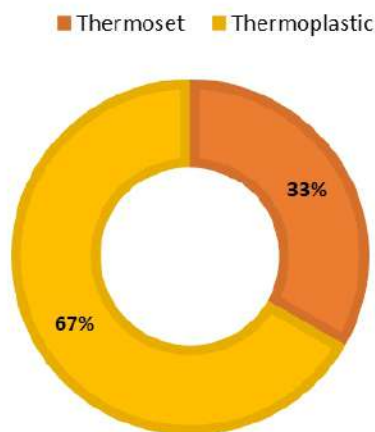


**Figure 1. 3:** Shares (%) of thermoplastic and thermoset resins in the FRP industry [16].

- **Metal Matrix Composites (MMCs)**

Alloys were originally used in metal matrix composites (MMCs). Over the past few decades, specialized matrix materials have been developed to enhance their performance. Common metallic matrices include alloys of Fe, Si, and Al, which are widely utilized in structural MMCs. Additionally, metals such as Pb, Mg, Cu, Ag, and Co have been employed as matrix materials, with their in-situ properties influenced by the manufacturing process. MMCs are commonly used in engineering applications where temperatures range between 250°C and 750°C. MMCs encompass a diverse range of materials defined by the metal matrix, reinforcement type, and geometry. Aluminum matrix composites dominate the field due to their versatility. Ceramics



are the most commonly used reinforcements, offering a desirable balance of stiffness, strength, and low density. Popular ceramic reinforcements include SiC, Al<sub>2</sub>O<sub>3</sub>, B<sub>4</sub>C, TiC, TiB<sub>2</sub>, and graphite, though metallic reinforcements like tungsten and steel fibers have also been explored. The morphology of the reinforcement material is a critical factor affecting the performance of MMCs [11,17].

- ***Ceramic Matrix Composites (CMCs)***

Ceramic materials possess a highly appealing set of properties, including high strength, stiffness at elevated temperatures, chemical inertness, and low density. However, this impressive combination is significantly undermined by a critical weakness: their lack of toughness. Ceramics are highly vulnerable to catastrophic failures due to surface or internal flaws, as well as thermal shock, and can be easily damaged during fabrication or use. To address this, ceramic matrix composites (CMCs) are designed to enhance the toughness of ceramics by incorporating fibers. This approach allows for the utilization of ceramics' high-temperature strength and environmental resistance while minimizing the risk of catastrophic failure. It is important to note that CMCs differ fundamentally from other composites. In non-ceramic matrix composites, the design philosophy often involves the fibers carrying a larger share of the applied load [18].

#### **1.2.1.2 Classification Based on Reinforcement**

Composite materials can be classified according to the type of reinforcement used to enhance their properties. The reinforcement phase is typically dispersed within the matrix material and can significantly influence the mechanical, thermal, and physical characteristics of the composite. *Fig.1.2* shows the mechanism of strengthening, which depends on the geometry and shape of the reinforcements.

- **Particulate Reinforced Composites**

This involves small particles such as ceramics or metals that are dispersed within the matrix to improve properties like wear resistance and thermal stability. these composites are not designed to improve the strength but to produce unusual combinations of properties [19].

- **Structural Composites**

Structural composites are made from materials like glass, plastic, carbon fiber, and wood. These composites can be either homogeneous or a mix of different materials. Their properties are

influenced by the geometric design of structural elements and the characteristics of the materials used. Commonly used types include laminated composites and sandwich structures [20].

*(a) Laminated Composites*

Laminated composites consist of two-dimensional sheets or layers that have a preferred direction of strength. These panels are designed to achieve high strength by aligning the layers in such a way that the direction of maximum strength varies with each successive layer. An example of this is plywood, which is made by gluing together thin layers of wood in alternating directions [21].

*(b) Sandwich Structures*

Sandwich structures are created by combining two or more individual components with different properties, resulting in high-performance materials. Typically, the outer layers (skin) have high stiffness, while the core provides shear strength. When combined, these structures exhibit a high flexural modulus [21].

- **Fiber-Reinforced Composites (FRCs)**

Fiber-reinforced composites (FRCs) are advanced materials created by cross-linking cellulosic fiber molecules with resins. These composites can be either continuous or discontinuous and consist of three main components:

- ✓ **The Matrix:** Acts as the continuous phase.
- ✓ **The Inter-phase Region:** A thin layer between the matrix and the fibers.
- ✓ **The Fibers:** Serve as the discontinuous or dispersed phase.

Continuous reinforcement gives FRCs high stiffness and strength, while discontinuous fibers are mainly used for cost-effective manufacturing methods. **Fig 1.4** demonstrates the use of FRP composites in various sectors.

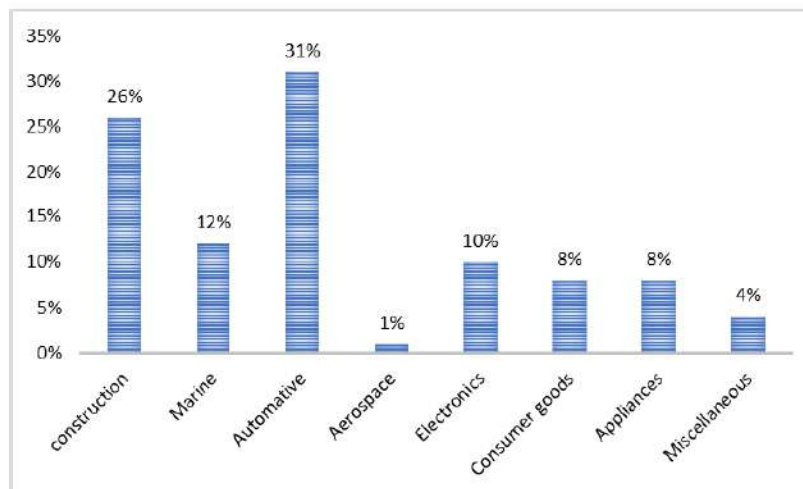


**Figure 1. 4:** The application of FRP composites in various sectors [22].

### 1.2.2 Glass fiber reinforcement

Glass fiber is one of the most commonly used reinforcement materials in polymer matrix composites (PMCs), valued for its combination of strength, affordability, and versatility. It is produced by drawing molten glass into fine, flexible filaments and is extensively applied across industries due to its high tensile strength, excellent durability, and resistance to heat, chemicals, and corrosion. In addition to its structural benefits, glass fiber offers excellent electrical insulation, thermal stability, impact resistance, and a high elongation-to-break ratio. Its favorable strength-to-weight ratio, particularly when compared to carbon fiber in certain contexts, along with resistance to moisture, friction, and environmental conditions, makes it a preferred material for numerous engineering and industrial applications [23,24]. *Fig1.5* shows different types of glass fibers according to form.

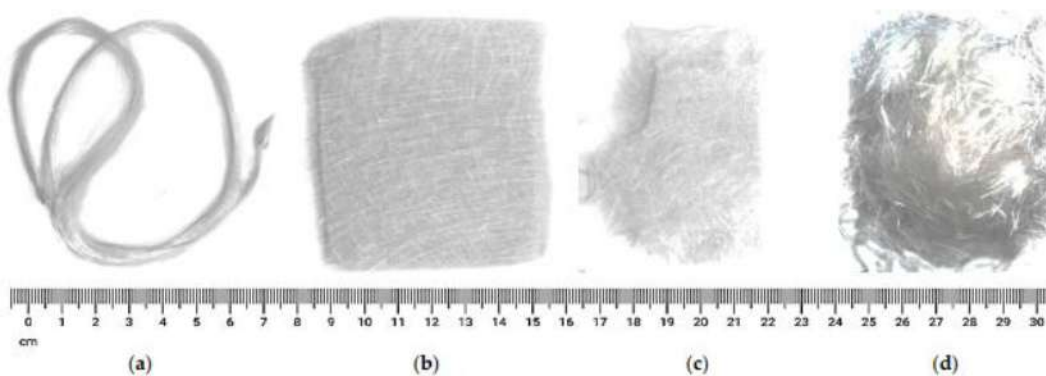


*Figure 1. 5:Types of glass fibers according form(a), long threaded (b), chopped (c) and finely chopped (d) fiber [25].*

There are several types of glass fibers, each with distinct compositions, manufacturing methods, and applications based on their mechanical, chemical, and thermal properties:

- **A-glass** is manufactured from cullet (recycled bottle glass) and has an alkali-lime composition with little to no boron oxide. It is not particularly resistant to alkalis and is typically used in applications where alkali resistance is not a critical requirement.
- **AR-glass** (alkali-resistant glass) is also produced from cullet but is formulated specifically to withstand alkaline environments. It is used where alkali resistance is essential, such as in concrete reinforcement.
- **C-glass**, also known as T-glass, is made from used glass staple fibers. It offers good resistance to chemical attack and most acids that can degrade E-glass. This type is

suitable for environments requiring higher chemical resistance, particularly against acids.

- **D-glass** is characterized by a high dielectric constant, making it ideal for electrical applications where such a property is important.
- **E-glass** a borosilicate type with high boron oxide content, is the most widely used fiber for glass-reinforced plastics. It was originally developed for electrical insulation applications. Although it is not resistant to chloride ions and its surface is soluble, it is commonly used in general structural applications due to its balanced properties and cost-effectiveness.
- **E-CR-glass** is similar to E-glass but with higher acid resistance, making it more suitable for environments with corrosive exposure.
- **R-glass** is an alumino silicate fiber that does not contain calcium oxide but includes high levels of magnesium oxide. It has excellent mechanical strength and is used in applications with high structural demands.
- **S-glass**, an alumino silicate without magnesium or calcium oxides, has the highest tensile strength of all glass fiber types. It is used in advanced applications such as aircraft components and missile casings, where superior mechanical performance is required [26].

The compositions of most used glass fibers are given in *Table 1.1*.

*Table 1. 1: Typical Composition and Properties of Glass Fibers [15]*

	<b>E- glass (%)</b>	<b>S-glass (%)</b>	<b>AR-glass (%)</b>
SiO <sub>2</sub>	54	65	64
TiO <sub>2</sub>			3
ZrO <sub>2</sub>			13
Al <sub>2</sub> O <sub>3</sub>	14	25	1
B <sub>2</sub> O <sub>3</sub>	9		
MgO	5	10	
CaO	18		5
Na <sub>2</sub> O			14
Modulus (GPa)	70	80	75
Strength	2200	2600	1700
Density (Mg/m <sup>3</sup> )	2.54	2.46	2.70



### 1.3 Glass fiber reinforced polymers (GFRP)

Glass Fiber Reinforced Polymer (GFRP), is a composite material made by combining fine glass fibers with a polymer resin matrix. This combination results in a material that boasts high strength, durability, and resistance to corrosion, making it suitable for a wide range of industrial applications. GFRP is commonly used in construction, aerospace, marine, and automotive industries due to its lightweight and versatile properties [27]. GFRP composites are increasingly used in bridge and building construction due to their advantageous properties compared to traditional materials [28,29]. Currently, pultruded GFRP profiles are primarily utilized in pedestrian bridges and the decks of road bridges [3]. For pedestrian bridges with larger spans, truss or cable-stayed systems are commonly employed. These systems function mainly in axial tension and compression, with minimal bending and shear, making them well-suited to the anisotropic properties of GFRP profiles.

In bridge decks, the profiles are typically arranged in the transverse direction, functioning as one-way slabs. The span, usually limited to 2–3 meters (depending on the system), dictates the spacing and number of main (longitudinal) girders required. In building construction, GFRP profiles are well-suited for structures in corrosive environments (e.g., wastewater treatment, indoor swimming pools, cooling towers) [30]. The use of GFRP profiles in housing and office buildings is less successful. However, they can offer significant advantages such as low weight in rehabilitating or transforming existing buildings. The tallest building with a primary load-bearing structure composed of pultruded GFRP profiles is shown in *Fig 1.6*. Since it is a mobile building, which can be (and was already once) dismantled and re-erected, the low weight of the profiles is a significant advantage[30].



*Figure 1. 6: Architectural Marvel in Basel, 1998: Structural Frames and Bolted Joints [30].*

### 1.3.1 Manufacturing of GFRP Composites

Manufacturing methods of GFRP composites are generally classified as open mold, closed mold, and other special processes. Thermoset resin-based FRP composites are mostly fabricated by hand lay-up, spray-up, vacuum bagging, filament winding, pultrusion, resin film infusion (RFI), resin transfer molding (RTM), vacuum-assisted resin transfer molding (VARTM) and compression molding process[31,32]. Whereas thermoplastic FRP composites are fabricated by injection molding and compression molding techniques. The selection of a manufacturing process depends on the type of resin, and fiber used and the target application of the final product. Each manufacturing process is developed for a certain purpose [33]. Here are some methods:

#### 1.3.1.1 Compression Molding Process

Compression molding (CM) is a manufacturing technique for fiber-reinforced polymers (FRP). In this process, the reinforcement package, which may be preheated or not, is placed in an open, heated mold cavity. This mold is installed on a mechanical or hydraulic molding press. The two heated metal halves of the mold are then closed, and high pressure is applied. This pressure ensures the FRP material conforms to the mold's shape. The applied pressure and heat are maintained until the reinforced material cures. The curing duration varies significantly, depending on the thickness and size of the part, ranging from a few tens of seconds to several minutes. The CM process employs thermosetting resins in a partially cured state, typically in

the form of putty-like masses, granules, or preforms. **Fig 1.7** illustrates the CM process, where the FRP package is compressed between two heated metal mold halves [25].

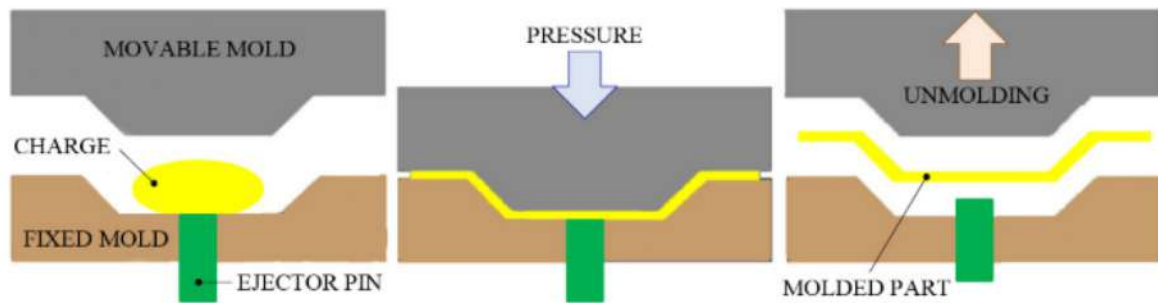


**Figure 1. 7:** Molding sequence: material loading, pressure forming, and part removal [25].

### 1.3.1.2 Hand Lay-Up Process

The hand lay-up (HLU) process is the most straightforward and oldest method for manufacturing FRP composites. It is commonly used for low-volume production of large structures in industries such as marine (boat hulls), automotive (car body panels), energy (wind turbine blades), transport (large containers), and household (swimming pools, bathtubs). Initially, a pigmented gel coat is sprayed on the mold to ensure a high-quality surface and to protect it from moisture. This gel coat also acts as an anti-adhesive, making it easier to remove the final composite part. Once the gel coat cures, a reinforcing mat is placed on the coated mold. Then, a thermosetting liquid resin (typically epoxy or catalyzed polyester) is poured onto the reinforcement material. Manual rolling is used to remove air trapped between the reinforcements, enhancing the interaction between the matrix and the reinforcement. This process also densifies the FRP composite and thoroughly wets the reinforcements with resin. To achieve the desired thickness, additional layers of resin and reinforcement are added successively. Finally, a catalyst or accelerator can be used to harden the composite without the need for an external heating system [34].



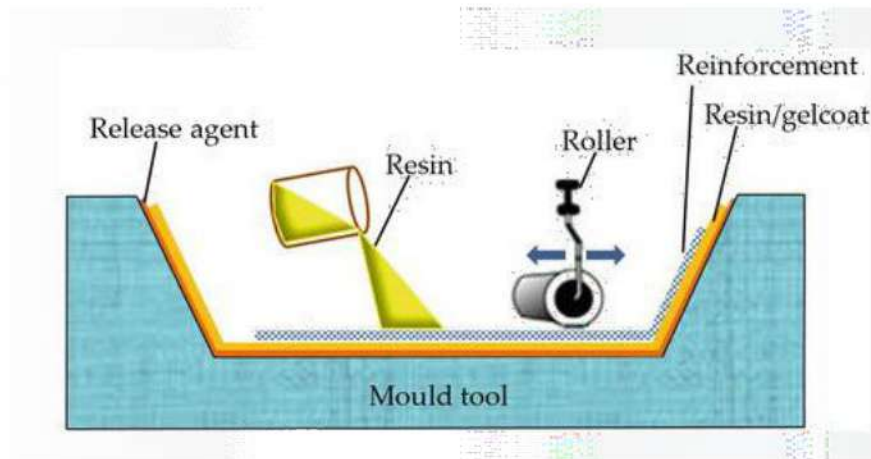


**Figure 1. 8:** Illustration shows the process behind the open molding hand lay-up technique [35].

### 1.3.1.3 Spray Lay-Up Process

Similar to the HLU process in its simplicity, the spray lay-up (SLU) technique enables faster FRP production and allows for more complex shapes. It also utilizes a low-cost open mold with one finished part surface, and the resin typically cures at room temperature, although the curing process can be sped up with moderate heat. The SLU technique is ideal for producing large FRP composite parts, such as bathroom units (shower and bathtub components) and ventilation hoods, in small to medium quantities. This method is suitable for low to moderate production volumes [36,37]. **Fig1.9** illustrates the SLU process.

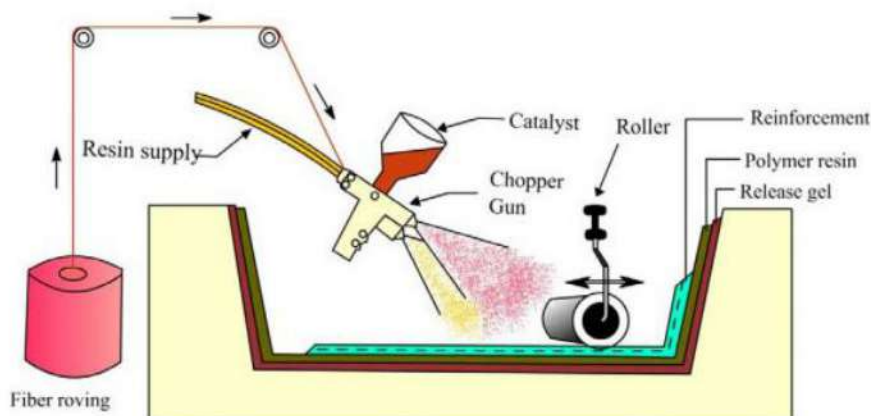


**Figure 1. 9:** Schematic of the spray lay-up process [20].

### 1.3.1.4 Filament Winding Process

The filament winding (FW) process is a well-established manufacturing technique highly suitable for automating fabrication processes. Generally, the FW process incorporates three winding patterns: helical, circumferential, and polar winding. This technique can produce both open structures (such as cylinders, pipes, bicycle forks, and rims) and closed-end structures



(like fuel storage and chemical tanks, stacks, rocket motor cases, pressure vessels, and drive shafts) with exceptionally high tensile strength. FW is capable of manufacturing both axisymmetric and non-axisymmetric parts by cross-weaving prepreg sheets, monofilaments, and roving of glass fiber (GF), carbon fiber (CF), or Kevlar fiber around a rotating mandrel [38].

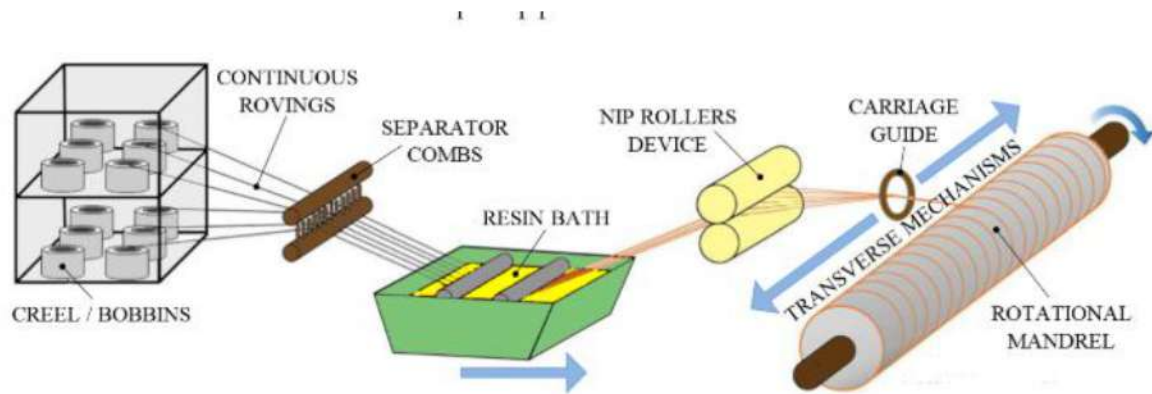


*Figure 1. 10: Typical filament winding process [25].*

### 1.3.2 Applications of GFRP composites

GFRP composites are known for their high strength-to-weight ratio, corrosion resistance, and versatility, making them ideal for applications in aerospace, automotive, construction, and marine industries. Their ability to withstand harsh environmental conditions and resist corrosion has led to their widespread use in infrastructure projects, such as bridges, pipelines, and wind turbine blades. The benefits of GFRP composites include their excellent fatigue resistance, ease of molding into complex shapes, and low maintenance costs. However, challenges remain in areas like cost, recycling, and manufacturing processes. Ongoing research continues to focus on improving the properties of GFRP composites and making them more sustainable and cost-effective for a broader range of applications [39].

Kim et al.[40] investigated the effects of different fabrication processes on the mechanical properties of glass fiber reinforced polymer (GFRP) composites used in yacht hull structures. Their study aimed to assess how hand lay-up (HL), vacuum infusion (VI), and hybrid (HL+VI) methods influence the strength, stiffness, and overall performance of these composites. In the experimental setup, GFRP composites were fabricated using the three processes, with samples prepared under varying vacuum pressures (0, 20, and 28 inches of mercury (Hg)) to evaluate the impact on void content and mechanical properties. Mechanical tests included tensile testing to measure tensile modulus, tensile strength, and strain at failure, as well as compression tests

to determine compressive strength and modulus. Additionally, ignition loss tests were conducted to assess fiber and resin weight percentages, sample density, and void content. The result shows that increasing vacuum pressure from 0 to 28 inches of Hg reduced void volume by 71%, resulting in a 36% increase in fiber weight percentage per unit volume. Higher vacuum pressures significantly enhanced mechanical properties: ultimate tensile strength (UTS) increased by 147%, and the tensile modulus improved markedly. Similarly, compressive properties saw an average modulus increase of 43% between the HL and VH-6 samples (0 and 28 inches of Hg). Hybrid composites outperformed those made with HL or VI processes alone, combining the benefits of both methods to achieve superior tensile and compressive properties, thereby demonstrating improved overall performance.

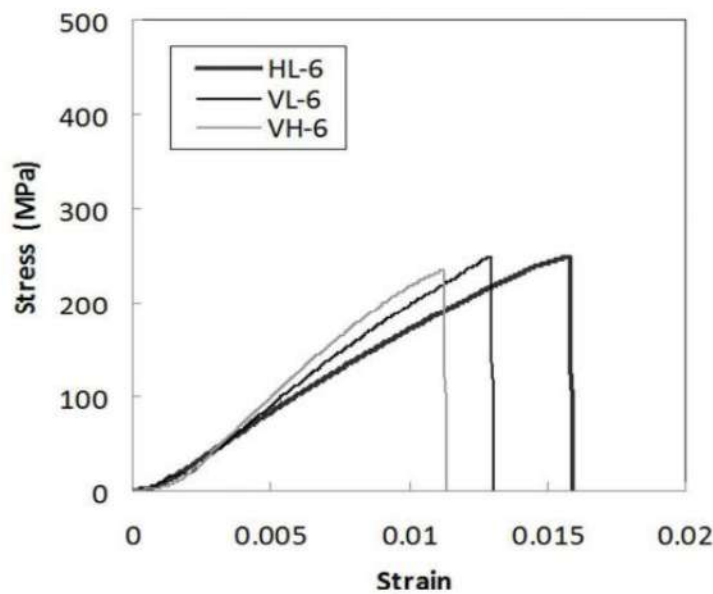


**Figure 1. 11:** Typical compressive stress vs. strain curves for HL-6, VL-6, and VH-6 samples [40].

Another study by Kim et al. [41] investigated the mechanical properties and failure mechanisms of hybrid glass fiber reinforced polymer (GFRP) composites, which are formed by combining hand lay-up (HL) and vacuum infusion (VI) processes. The goal was to enhance structural performance and ease of manufacturing for marine structures. The experimental setup examined three types of GFRP composites: HL, VI, and a hybrid method combining both HL and VI. The materials were fabricated from three different production batches, and mechanical property tests, including tensile, compressive, and in-plane shear tests, were conducted to evaluate the performance of the composites. The results showed that the VI process significantly improved the tensile properties of GFRP composites compared to HL, with hybrid composites demonstrating a combination of the benefits from both methods. Additionally, the compressive



strength and modulus increased with higher vacuum pressure, and hybrid composites exhibited better performance in terms of compressive properties compared to HL. Higher vacuum pressure also reduced void content, leading to better mechanical properties and more efficient use of matrix material. The study concluded that hybrid GFRP composites, particularly those with three sets of VI layers, showed the highest tensile properties, while those with two sets had the highest compressive properties. The batch homogeneity of the VI samples was better compared to HL samples, but hybrid composites had lower batch homogeneity due to the combination of HL and VI processes.

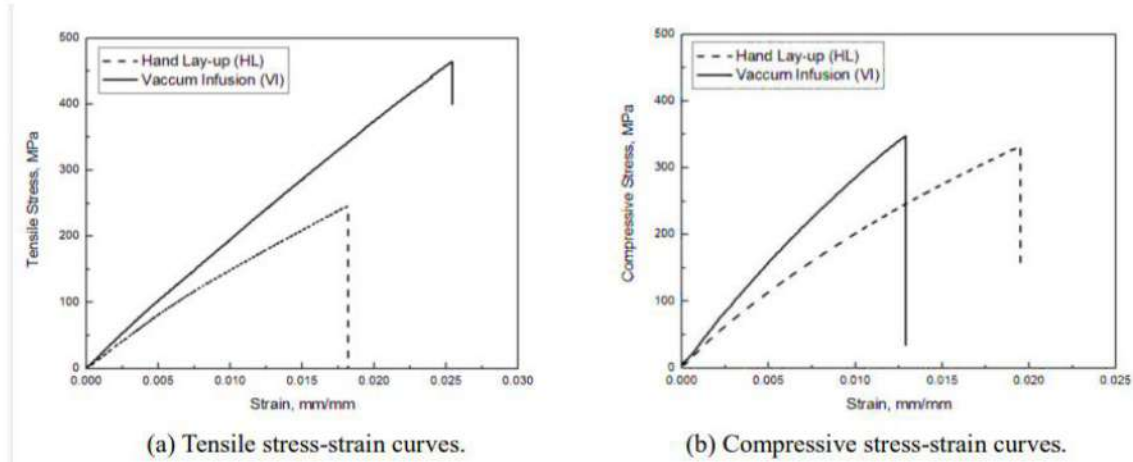


**Figure 1.12:** Typical stress-strain curves for the HL and VI samples [41].

The study by Prashant S et al. [42] aimed to develop a new polymer-based composite material with varying reinforcement angle orientations and examine its tensile behavior. The composite was created using E-2 glass fibers and epoxy resin through the hand lay-up. Layers of glass fibers were alternately coated with a mixture of epoxy resin and hardener until the desired laminate thickness was achieved, followed by curing in ambient conditions. Additionally, specimens were cut from the laminate based on ASTM D3039 standards, with fiber orientations set at  $90^\circ$ ,  $45^\circ$ , and  $30^\circ$ . Moreover, tensile tests were conducted on these specimens using a Lloyd Universal Testing Machine (UTM), applying a gradually increasing load at a rate of 2 mm/min until failure. The results revealed that tensile properties depended on fiber orientation. Specifically, specimens with  $90^\circ$  fiber orientation demonstrated the highest tensile strength, followed by those with  $45^\circ$  and  $30^\circ$  orientations. Furthermore, experimental findings aligned closely with theoretical predictions and finite element analysis (FEA), confirming the accuracy of the calculated ultimate tensile stress. In conclusion, the study showed that the load-bearing capacity increases with the number of layers, while maximum stress rises as the number of layers decreases.

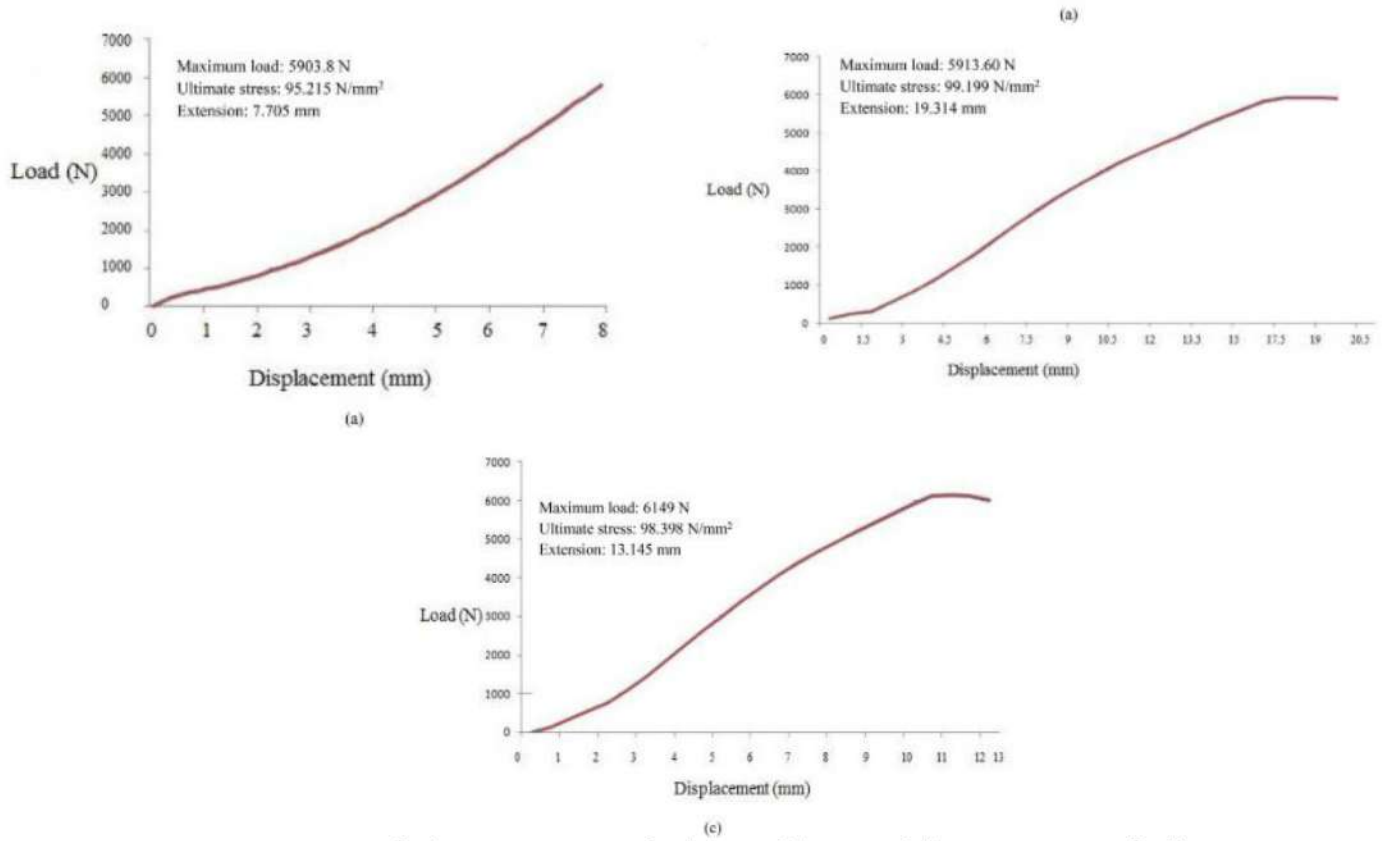


**Figure 1.13:** Load v/s extension curve for (a) 90° (b) 45° and (c) 30° orientation [42].

Mokhtar et al. [43] evaluated the mechanical and optical properties of glass fiber-reinforced polyester composites for agricultural greenhouse construction. Using Response Surface Methodology (RSM), they examined how fiber content, fiber length, and plate thickness affect mechanical properties like stress and elasticity modulus, as well as light transmittance. Samples were prepared through manual contact molding with varying fiber content (20%–40%), fiber lengths (35–45 mm), and plate thicknesses (0.6–3 mm). Mechanical tests, including three-point bending, were performed using a universal testing machine to measure stress and elasticity modulus. Moreover, optical properties were assessed with a spectrophotometer, focusing on light transmittance in UV, visible, and near-IR spectra. The results showed that optimal mechanical performance occurred with fiber content between 20%–40%, fiber lengths of 35–45 mm, and plate thicknesses of 0.6–3 mm. Furthermore, while higher fiber content and thickness improved strength, they reduced light transmittance. The study concluded that balancing mechanical strength and light transmission is crucial for effective greenhouse construction, with moderate fiber content and thickness offering the best performance. Additionally, using UV plastic films can further enhance the optical properties of these composites.

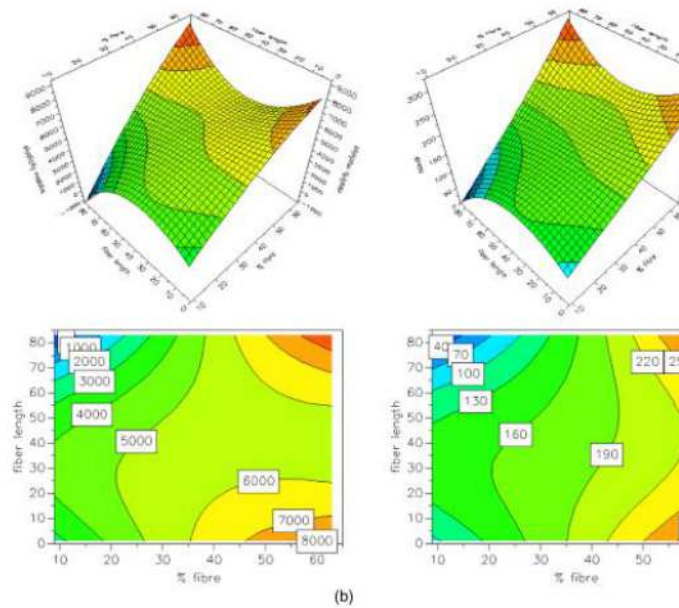


**Figure 1. 14:** Graphical representation of the mathematical models (a) Low Plate thin  $e = 0.6$  mm, (b) Plate thin in center  $e = 1.8$  mm, (c) High Plate thin  $e = 3$  mm (a) [43].

Hota et al.[44] investigated the rehabilitation of timber railroad bridges using GFRP composites. The research evaluates the application of GFRP composite wraps as a viable rehabilitation alternative for piles on in-service 1900s timber bridges, focusing on two methods: spraying chopped fibers on resin-wet timber members and vacuum bagging of GFRP-wrapped decayed timber bridge members (**Fig 1.15**). The study aims to develop safer, faster, and more practical methods for in-situ rehabilitation of timber railroad bridges without interrupting rail traffic. the rehabilitation resulted in significant improvements in their mechanical properties, with shear moduli increasing by 41% and 267% for two of the stringers after repair. The load testing revealed that the repaired specimens exhibited enhanced flexural rigidity and shear capacity, demonstrating the effectiveness of the GFRP and SGFRP techniques in restoring the structural integrity of damaged timber members. Field rehabilitation of the bridge showed a notable reduction in strain, with a 43% reduction in the piles and a 46% reduction in the pile cap after applying GFRP composite wraps. This indicates that the GFRP rehabilitation not only



improved the load distribution but also contributed to the overall stability and performance of the bridge structure over time.

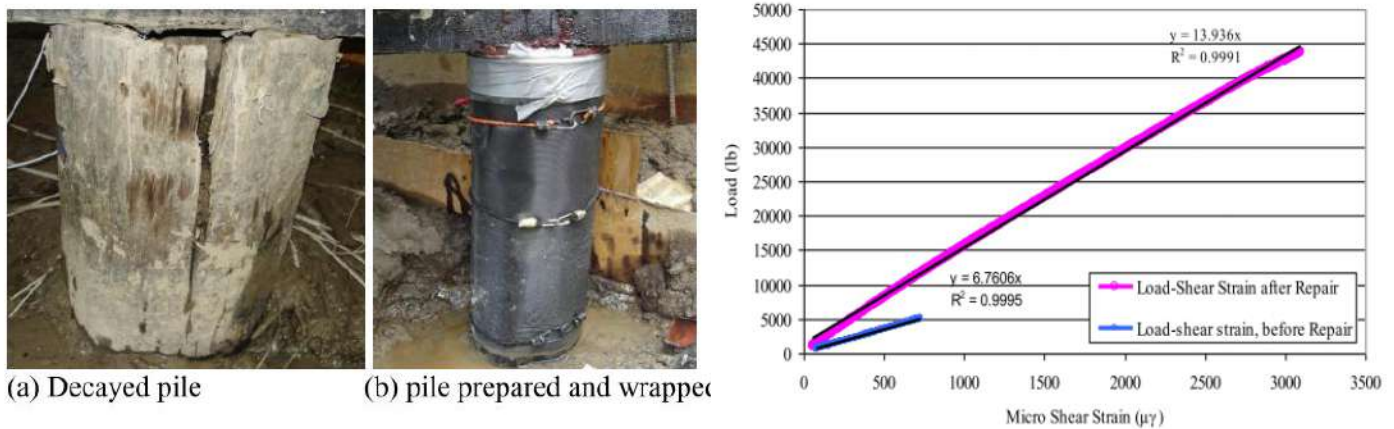


**Figure 1. 15:** Pile rehabilitation with GFRP composites, Load vs. shear strain rehabilitated specimen [44].

**Table 1. 2** Research on the application of GFRP in Engineering Sectors.

Sector	Application	Key Findings	Representative studies
Construction	The paper investigates the use of incorporating Glass GFRP as a skin reinforcement for reinforced concrete (RC) ties, with the goal of enhancing crack control and performance in concrete elements especially in demanding environments such as pipelines and tunnel linings.	GFRP skin reinforcement proves to be an effective approach for controlling crack patterns and is particularly beneficial for structures where ensuring adequate concrete cover over the steel reinforcement is challenging such as in precast tunnel lining segments.	Coccia et al. [45]
	The research aims to investigate GFRP as a replacement for steel rebars in concrete, focusing on its lightweight nature, corrosion resistance, superior tensile strength, and ease of installation.	The GFRP rebars exhibit higher tensile strength, higher corrosion resistance, and moderate flexural strength compared to steel rebars, making them a suitable alternative for foundation applications.	Jabbar and Farid [46]

Electrical industry	The application of GFRP in the power equipment at substation, power transmission, and distribution network is discussed, where the loadbearing insulator tubes are made of epoxy resin reinforced with electrical grade fiberglass using a wet filament-winding technique.	GFRP composites exhibit mechanical properties that are comparable to steel in strength and superior to aluminum in stiffness, making them suitable for demanding applications in power equipment.	Chen 2021 [47]
Marine	The study involved designing and fabricating GFRP composites for surfboard production. The composites were prepared using both unidirectional and bidirectional laminates,	The results highlight the potential of GFRP composites reinforced with semimetals for use in marine applications, particularly in terms of their mechanical properties and resistance to environmental factors.	Reddy et al. [48]
Automotive	The study provides meaningful insights into applying Long Glass Fiber Thermoplastics in the automotive sector, highlighting its mechanical benefits and potential to improve vehicle efficiency while promoting environmental sustainability.	Long Glass Fiber Reinforced Thermoplastics demonstrate strong mechanical performance with high strength-to-weight ratios, making them ideal for automotive applications focused on weight reduction to enhance fuel economy and reduce emissions.	Du et al. [49]

#### 1.4 Sandwich structures

According to Noor, Burton, and Bert [50], the idea of sandwich construction can be traced back to Fairbairn in 1849 . In the UK, this construction technique was notably applied in the Mosquito night bomber during World War II. In 1943, engineers at Wright Patterson Air Force Base created the Vultee BT-15 fuselage, incorporating fiberglass-reinforced polyester faces with either glass-fabric honeycomb or balsa wood as core materials [51]. Building upon this early foundation, recent decades have seen significant advancements in the design and application of sandwich structures, particularly driven by innovations in materials and fabrication techniques[52]. Numerous studies have explored their performance in sectors such as aerospace, automotive, civil engineering, and renewable energy, highlighting their



exceptional strength-to-weight ratio, thermal insulation properties, and structural efficiency under complex loading conditions [53]. In civil engineering applications, sandwich structures have emerged as high-performance alternatives to conventional construction systems, particularly in the design of lightweight flooring systems, roofing panels, and precast structural elements. Their multilayered configuration enables a substantial reduction in self-weight while enhancing load-bearing efficiency, thermal insulation, and overall structural integrity under complex loading scenarios.

Chróścielewski et al. [54] presents a comprehensive examination of a novel sandwich composite footbridge, highlighting the practical application of laminated composites in civil engineering. The bridge design incorporates GFRP skins paired with a polyethylene terephthalate (PET) foam core, forming a lightweight yet durable sandwich structure. Spanning 14 meters and featuring a U-shaped cross-section, the structure was developed with a focus on manufacturing simplicity and ease of installation, presenting a cost-efficient alternative to conventional construction materials. Through in situ static testing and complementary numerical analysis, the study confirms the structural integrity and suitability of the bridge for real-world application. These findings support the broader adoption of laminated composite technologies in future bridge construction projects.



**Figure 1.16:** Front perspective and overall view of the footbridge taken at the Gdansk University of Technology campus [54].

Obaid and Jaafer [55] explored the development of an innovative ferrocement sandwich composite system to replace traditional jack arch slabs, which typically use clay bricks and gypsum mortar. The new system incorporates precast lightweight panels composed of two 15 mm ferrocement face layers reinforced with four layers of steel wire mesh, and a lightweight core made of either expanded polystyrene (styropor) or cellular concrete blocks (thermostone). A total of eight slabs were tested: one traditional control and seven composite variants. The slabs were subjected to three-point bending tests to evaluate flexural behavior, with variations in span, depth, core material, and the use of shear connectors. Results showed that the composite slabs significantly improved load-bearing capacity, stiffness, and ductility compared to the

traditional slab. The best performance was observed in specimens with thermostone cores and increased section depth, demonstrating the viability of the proposed system for modern civil engineering applications.

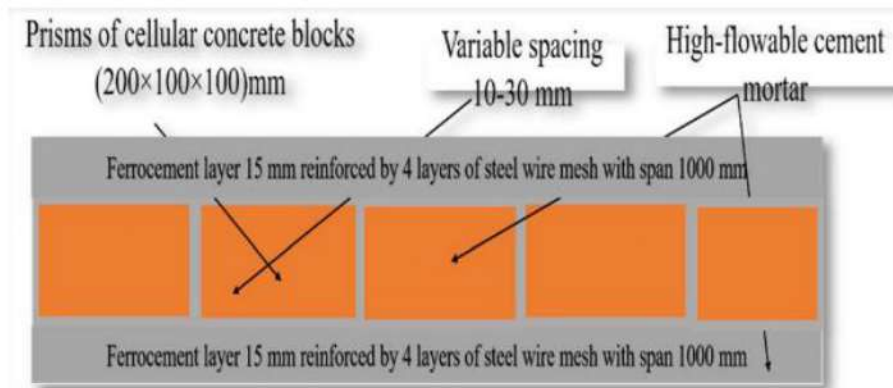


**Figure 1. 17:** Front view of specimen studied [55].

The study by Zhang.Y et al. [56] presents the development and mechanical evaluation of a novel composite sandwich structure tailored for construction applications. This structure integrates GFRP face sheets, a balsa wood core, and an internally placed cold-formed profiled steel plate. The components are connected using stainless steel core rivets, forming a hybrid panel that leverages the lightweight, high-strength, and corrosion-resistant properties of its constituent materials. To assess mechanical performance, the authors conducted three-point bending tests on eleven full-scale specimens, analyzing the influence of (1) the shear span-to-depth ( $a/d$ ) ratio, (2) the thickness of the steel plate, and (3) the spacing of rivets. Results showed that decreasing the  $a/d$  ratio significantly increased the ultimate load capacity due to enhanced shear performance. Increasing the steel plate thickness improved both stiffness and strength, while reducing the rivet spacing contributed to better stress distribution and delayed delamination or debonding failures. The combination of balsa core and profiled steel reinforcement led to superior bending resistance, shear performance, and failure stability, making the system promising for use in modular flooring, bridge decks, and prefabricated building elements.



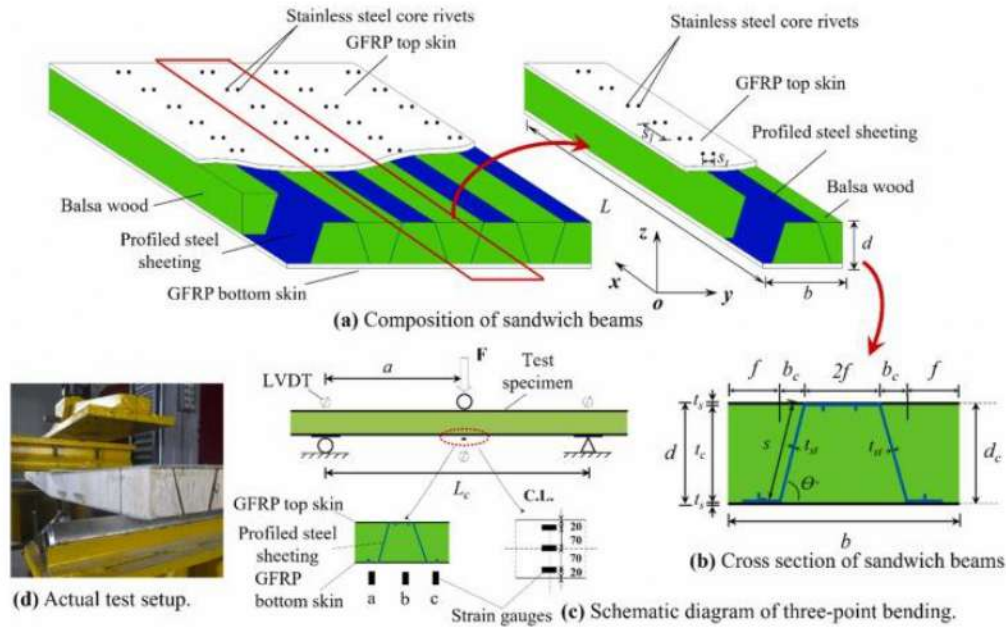


**Figure 1.18:** Schematic diagram of specimen and test setup [56].

### 1.4.1 Constituents of sandwich structure

Sandwich structures are primarily categorized based on the configuration and material of their core, which significantly influences their mechanical and functional properties. The main classifications include honeycomb, foam, corrugated, and truss core sandwich structures (**Fig 1.20**). Honeycomb cores feature a hexagonal cell pattern, offering high stiffness-to-weight ratios and are commonly utilized in aerospace applications due to their excellent mechanical performance. Foam cores, such as polyurethane or polystyrene foams, provide good energy absorption and thermal insulation, making them suitable for automotive and building industries. Corrugated cores consist of wavy or sinusoidal sheets that deliver directional stiffness and are often used in packaging and construction. Truss cores are composed of interconnected struts forming a lattice structure, offering high shear strength and are employed in applications requiring lightweight and high-load-bearing capabilities. Each core type is selected based on specific application requirements, balancing factors like weight, strength, and thermal properties. [57]

The face sheets of sandwich structures play a critical structural role by carrying the majority of the in-plane and bending loads. Positioned on either side of the lightweight core, they act as the flanges in a beam, resisting tensile and compressive stresses generated under flexural loading. Their stiffness and strength significantly influence the global performance of the sandwich panel, especially in terms of flexural rigidity and buckling resistance [58]. They can be made from a variety of materials depending on the design requirements, including polymer matrix

composites (PMC), metal matrix composites (MMC), and fiber-reinforced polymers (FRP). The selection of face sheet materials is guided by factors such as stiffness, strength, weight, and environmental resistance, ensuring the structural integrity and performance of the sandwich component.

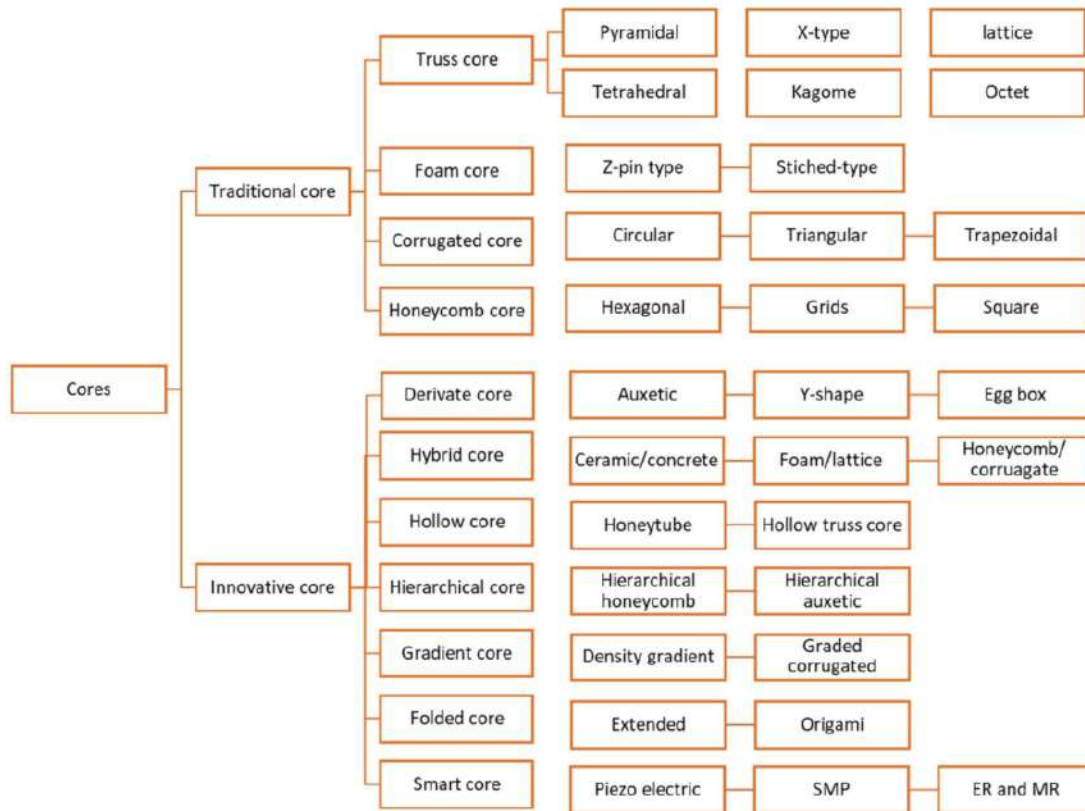


**Figure 1. 19:** Classification of sandwich structures based on core [59].

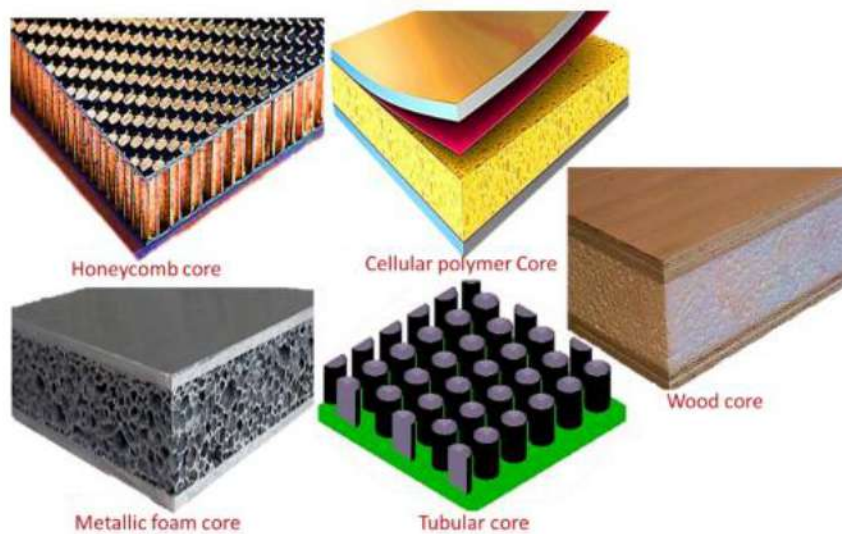


**Figure 1. 20:** Different core structures in sandwich composites [60].

### 1.4.2 Foam core

#### 1.4.2.1 Polyurethane foam

Sandwich composites featuring a polyurethane foam (PU) core are highly versatile materials, used in a wide range of applications from basic construction components to sophisticated engineering solutions. This versatility has established them as prominent materials in modern engineering. PU foams stand out as one of the most extensively studied and utilized materials within the polymer family, owing to their exceptional properties, including light weight, eco-friendliness, low density, excellent impact and shock absorption, ease of processing, and remarkable elasticity. Similar to other cellular solids, PU foams consist of a cellular structure where polyhedral cells are arranged in three dimensions to occupy space, forming what is commonly referred to as foam [61,62].

PU foams are primarily produced through a polyaddition reaction involving various types of polyols and isocyanates, which serve as fundamental components of polymeric materials. PUs are polymers that are formed by the reaction between the OH (hydroxyl) groups of a polyol with the NCO (isocyanate functional group) groups of an isocyanate, and the name is associated with the resulting urethane linkage [63,64]. The wide range of available raw materials (polyols and isocyanates) and the ability to modify their proportions during production enable the creation of numerous types of PU foams with tailored properties [65,66]. This adaptability in PU foams synthesis allows manufacturers to achieve specific characteristics to meet varied requirements. Based on chemical composition and mechanical properties such as rigidity, strength, and flexibility, PU foams are commonly classified into rigid polyurethane foams (RPUFs), semi-rigid foams, and flexible or viscoelastic foams. These classifications have led to diverse applications over time, including use in furniture, construction, footwear, household appliances, automotive components, refrigeration, and insulation. RPUFs, in particular, are widely used as core materials in sandwich structures for numerous engineering and industrial applications [67]. The sequential process for preparing PU foam is illustrated in *Fig 1.17*. Sandwich composites are advanced materials used in a variety of industries due to their exceptional strength-to-weight ratio. These structures consist of two strong outer layers (skins) and a lightweight core. When PU foam is used as the core material, it provides excellent thermal insulation and good mechanical properties [68]. In recent years, much research has examined the mechanical behavior of PU foam sandwich composites under mechanical loads. Various numerical, analytical, and experimental approaches have been employed to study their flexural



properties, with particular attention to the influence of different parameters on their overall mechanical performance [69–74].

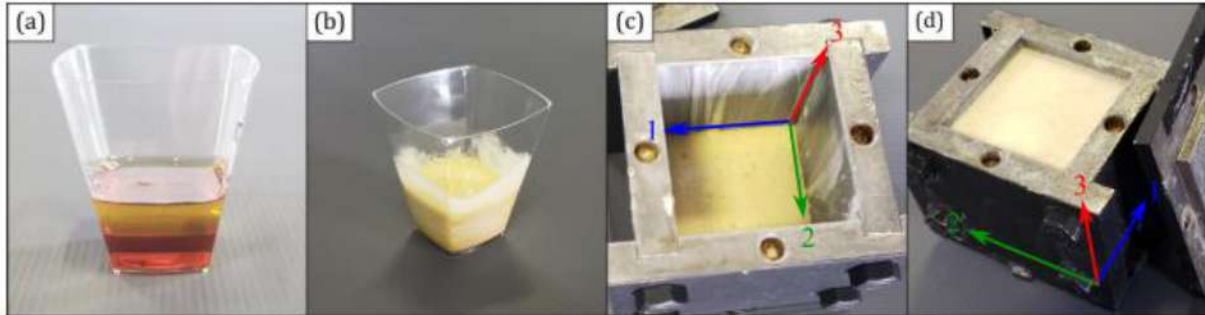


**Figure 1. 21:** Foam Synthesis Process: (a) Mixing Polyol and Isocyanate, (b) Hand-Homogenization, (c) Pouring into Mold with Expansion and Transverse Directions, (d) Final Expanded Foam [75].

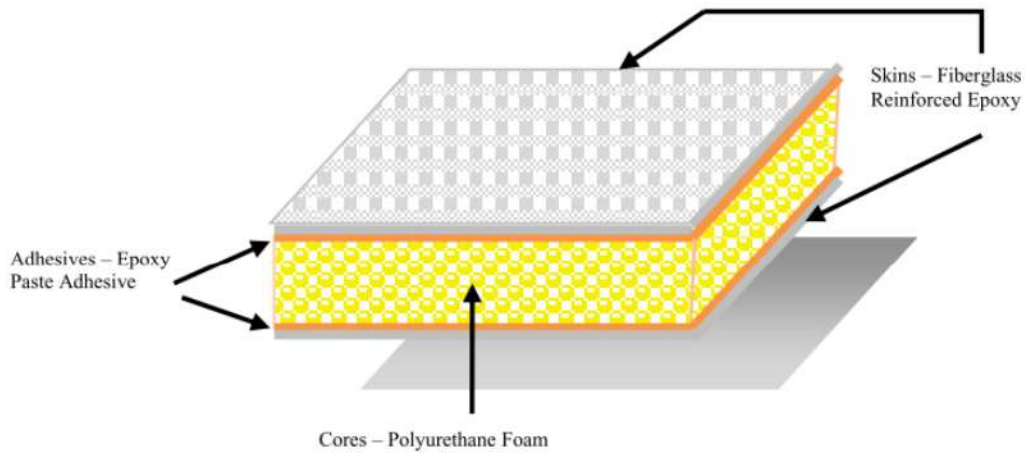


**Figure 1. 22:** Sandwich composites panel of glass fiber and polyurethane foam core (GFRP - PU) [76].

Mostafa et al. [77] analyzed PU-foam/glass-fibre composite sandwich panels under flexural static load. The study focused on the flexural behavior of sandwich structures with cohesive skin-core interaction under four-point bending loading. The experimental results indicated that the panels exhibited an initial linear elastic behavior followed by non-linear behavior. The finite element analysis showed good agreement with the experimental response up to failure. The study concluded that the cohesive nature of the skin-core interaction significantly influenced the flexural behavior of the sandwich panels.

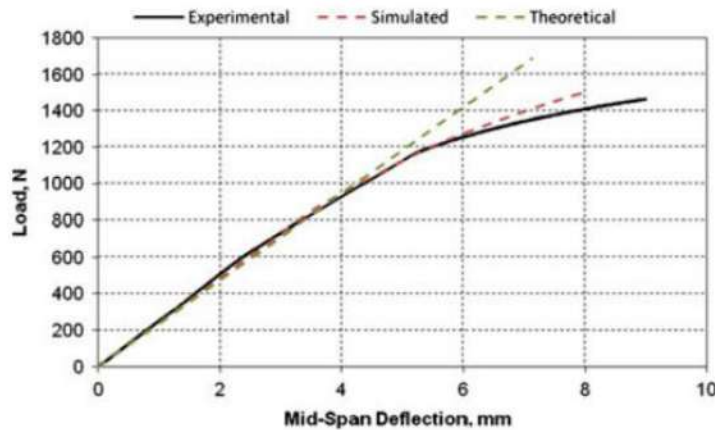


**Figure 1. 23:** *Experimental, simulated and theoretical load–deflection behavior of the composite sandwich panel [77].*

Tuwair et al. [78] aimed to evaluate the structural performance of an innovative low-cost small-scale prototype deck panel under monotonic and fatigue bending. The study focused on the flexural stiffness, strength, and shear stiffness of the panels. The panels consisted of two glass fiber-reinforced polymer (GFRP) facings with webs of bidirectional E-glass-woven fabric, separated by a trapezoidal-shaped low-density polyurethane foam core. The GFRP panels were manufactured using a one-step vacuum-assisted resin transfer molding process. Small-scale prototype deck panels were tested in four-point bending to investigate their flexural behavior, and the ultimate bearing capacity was determined through flatwise compressive tests. The experimental results indicated that the panels exhibited a higher structural performance in terms of flexural stiffness, strength, and shear stiffness. The initial failure mode for all panels was localized outward-compression skin wrinkling of the top facing, and the ultimate failure was caused by local crushing of the top facing under the loading point due to excessive compressive stresses. The study concluded that the polyurethane foam core significantly influenced the flexural behavior of the sandwich panels.

Sharaf et al. [79] proposed an innovative sandwich panel for structural walls in post-disaster housing and load-bearing panels for modular construction. The study focused on the flexural and shear behavior of the panels, which consist of two 3-D high-density polyethylene (HDPE) skins and a high-density polyurethane (PU) foam core. The objective was to validate the panel's effectiveness in increasing ultimate bending strength. Experimental tests on medium-scale specimens characterized core shear behavior and determined flexural and shear stiffness. Numerical and experimental investigations showed that the 3-D HDPE sheets with a studded surface significantly enhance pull-out and delamination strength. The results demonstrated that



using 3-D skins with 1200 studs per square meter resulted in a strong and stable composite section. The foam core and skins displacement were in sync under flexure, indicating well-integrated and ductile behavior of the composite panel.

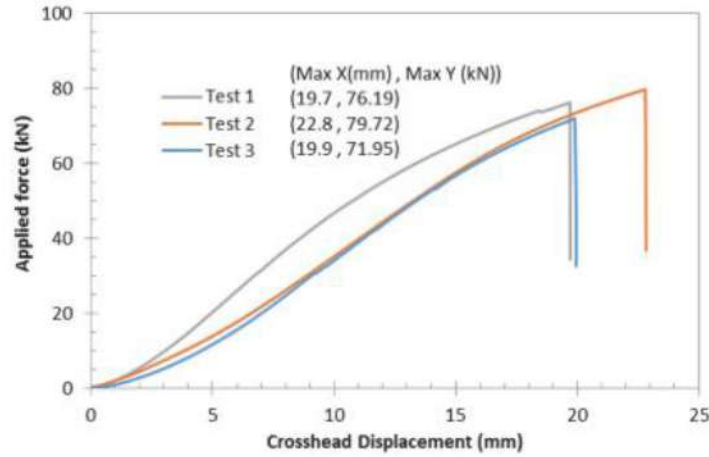


**Figure 1. 24:** Applied force as a function of crosshead displacement for a four-point quarter-span loading test [79].

Yadav et al. [80] investigated the moisture absorption capability, compressive properties, and collapse modes of various types of composite sandwich structures under compressive load. The study aimed to understand the behavior of sandwich structures with different hybridized skin materials and core compositions. The core material used was rigid polyurethane foam prepared in four different compositions by varying the weight fractions of methylene di-isocyanate (MDI) and polyether polyol. The skin materials used were S-glass, jute, and bamboo fibers in epoxy resin. Experimental tests, including moisture absorption and compressive tests, were conducted according to ASTM standards. The results indicated that Type II rigid PUF foam, containing 50% MDI and 50% polyol, exhibited the lowest moisture absorption and the highest compressive strength in both flatwise and edgewise compression tests. The study also observed two modes of collapse in the edgewise compression test: progressive end-crushing and unstable collapse. The bonding strength between the core and face materials significantly influenced the compressive properties and failure modes of the sandwich structures.

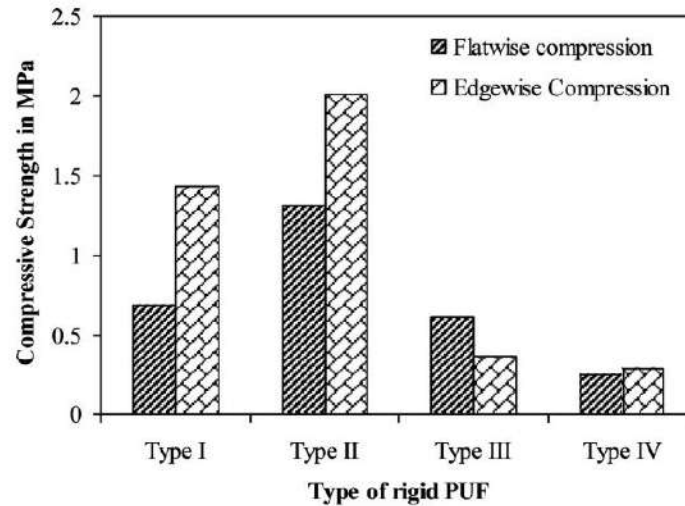


*Figure 1. 25: Variation of compressive strength on type of rigid PUF in compression [80].*

#### 1.4.2.2 Polystyrene foam

Polystyrene (PS) is an aromatic hydrocarbon polymer formed through the polymerization of styrene monomers. It can be produced in both solid and foam forms, serving a wide range of consumer applications. In its foamed state, polystyrene is lightweight, soft, and compressible, consisting of approximately 95% to 98% air. This structure makes it ideal for use in protective and food packaging, insulation materials, automotive components, surfboards, and architectural models [81]. Several studies have demonstrated that incorporating PS foam is highly effective in various applications [82–87]. In the construction industry, PS foam is widely used as an insulation material in walls, roofs, and foundations due to its excellent thermal resistance and lightweight nature. Additionally, it serves as a water and vapor barrier, preventing moisture infiltration that can lead to structural damage and mold growth, thereby contributing to a healthier indoor environment and enhancing the durability of buildings [88]. Given its excellent properties has also found widespread use as a core material in sandwich structures. Its ability to provide structural support while minimizing overall weight makes it an ideal candidate for applications where both mechanical performance and thermal efficiency are essential, such as in building panels, prefabricated walls.

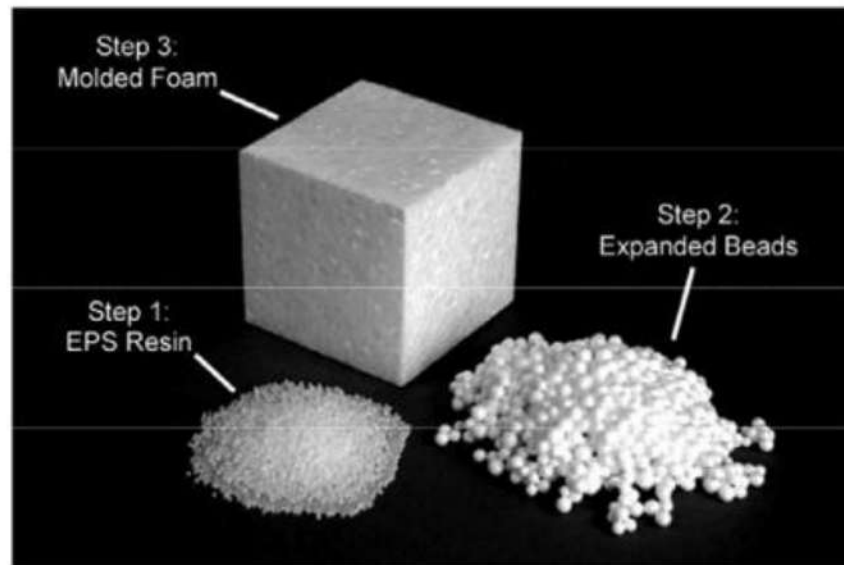


**Figure 1. 26:** Three important forms of EPS Beads formed via the expansion of resin are molded into the desired shape [88].

Giuliani et al. [89] presented a detailed review of over two decades of experience in Italy with the use of expanded polystyrene (EPS) geofoam in road construction. EPS had proven to be an effective lightweight fill material, particularly suited for geotechnical applications in soft soil areas where traditional materials would lead to excessive settlement or instability. The study highlighted its use in a variety of applications such as road embankments, slope stabilization, bridge abutments, and retaining wall backfill. One of the main advantages emphasized is the low density of EPS (about 1% of traditional soil weight), which significantly reduced vertical and lateral stresses on underlying soils and adjacent structures. The research outlined EPS's role in accelerating construction times, especially in urban or constrained environments, due to its ease of handling, quick installation, and minimal ground disturbance. In addition, the researchers examined long-term performance through various Italian case studies, showing that EPS has maintained its mechanical stability and resistance to environmental degradation over time. Despite its relatively higher initial cost compared to conventional fills, EPS often results in overall cost efficiency thanks to reduced labor, faster construction, and lower long-term maintenance demands. Overall, this comprehensive review confirms that EPS geofoam is a reliable, mature, and efficient solution in modern geotechnical engineering, particularly valuable in addressing challenges related to weak subsoils and strict project timelines.



**Figure 1. 27:** Road embankment with EPS-blocks at Passo del Brattello during the construction phase (2002) and at present (2019) [89].

Tabatabaiefar et al. [90] examined the mechanical properties of sandwich panels constructed from polystyrene/cement mixed cores and thin cement sheet facings. The objective of the study was to understand the mechanical behavior and properties of these sandwich panels. A series of experimental tests were performed to determine the modulus of elasticity and ultimate strength of the panels in both dry and saturated conditions. The results showed that the sandwich panels exhibited improved mechanical properties when the polystyrene/cement cores were combined with thin cement sheet facings. The study concludes that these sandwich panels can provide structural load-bearing capacity, insulation properties, weatherproofing, and durability, making them suitable for various building applications.





**Figure 1. 28:** Cement/polystyrene core and cement sheet facing sandwich panels [90]

Ahmed and Singh [91] investigated the in-plane structural performance of expanded polystyrene (EPS) core reinforced concrete sandwich panels (RCSPs) under axial and in-plane shear loading. Through a combination of experimental testing and finite element analysis (FEA), the study evaluated the panels' load-bearing capacity and failure mechanisms. The results demonstrated that the RCSPs possess sufficient strength for use in load-bearing wall applications, with common failure modes including vertical cracking, transverse splitting of the concrete wythes, and concrete crushing. The FEA models closely matched the experimental data, confirming the accuracy of numerical simulations in predicting the panels' behavior. This study highlights the potential of EPS core RCSPs in lightweight construction and contributes valuable data for the design and analysis of such structural systems.



**Figure 1. 29:** Produced EPS core and reinforcement panel [91].

### 1.4.3 Hybrid core

Hybrid core, as one of the innovated cores, in sandwich structures refers to a core composed of two or more different materials or core architectures combined to exploit the benefits of each component. This configuration aims to improve mechanical performance, such as strength, stiffness, energy absorption, or thermal resistance, beyond what a single core material could offer on its own. Hybrid cores may combine, for example, polymer foams with reinforced elements (like rods or lattice structures), or different types of foams, honeycombs, or composite inserts, to create a tailored response under specific loading or environmental conditions [92].

Abdi et al. [93] examined the mechanical performance of sandwich panels reinforced with through-thickness polymer pins. These panels consist of GFRP face sheets and a closed-cell polyurethane foam core, with cylindrical polymer pins connecting the face sheets through the core. Experimental evaluations, including flatwise compression and three-point bending tests, revealed that the incorporation of polymer pins significantly enhances the panels' mechanical properties. Specifically, the pin-reinforced PRFCS exhibited increased flatwise compression strength and flexural stiffness compared to unreinforced counterparts FCS. The study also found that the diameter of the polymer pins plays a crucial role in determining the extent of these improvements. These findings suggest that through-thickness polymer pin reinforcement is an effective method for improving the structural integrity and load-bearing capacity of foam core composite sandwich panels, making them suitable for applications requiring enhanced mechanical performance.

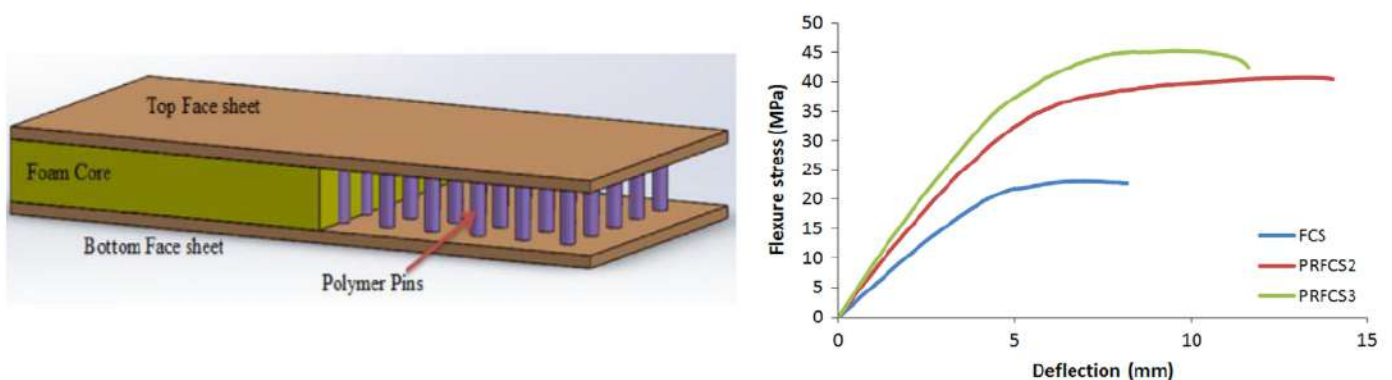


**Figure 1. 30:** a) Schematic of sandwich panel studied, b) Flexural behavior of FCS and PRFCS panels [93].

Similar study by Balıkoğlu et al. [94] investigated the impact of through-thickness resin pin reinforcement on the mechanical behavior of marine-grade sandwich panels. These panels comprised E-glass/vinyl ester face sheets and a polyvinyl chloride (PVC) foam core. To

enhance structural performance, the researchers introduced circular perforations through the foam core in twelve different square-pattern arrangements. During the vacuum-assisted resin infusion molding (VARTM) process, these perforations were filled with resin, forming solid resin pins that connect the face sheets through the core thickness. Experimental evaluations, including flatwise compression and three-point bending tests, revealed that the incorporation of resin pins significantly improved the panels' mechanical properties. Specifically, increasing the diameter of the resin pins led to over a 133.8% increase in maximum failure load during bending tests, albeit with a weight increase of up to 67%. Additionally, the flatwise compression strength required to induce core crushing was markedly enhanced by the presence of resin pins.

Yan et al. [95] studied the mechanical performance of sandwich beams featuring corrugated steel cores filled with aluminum foam. The primary objective was to assess how foam filling influences the bending behavior and failure mechanisms of these composite structures under quasi-static three-point bending loads. In the experimental setup, sandwich beams with both empty and aluminum foam-filled corrugated cores were subjected to three-point bending tests. The results demonstrated that foam filling significantly enhanced the bending resistance of the beams. Specifically, the foam-filled cores exhibited increased load-bearing capacity and stiffness compared to their unfilled counterparts. Additionally, the presence of foam altered the failure modes, shifting from local buckling in unfilled cores to more global deformation patterns in foam-filled cores.



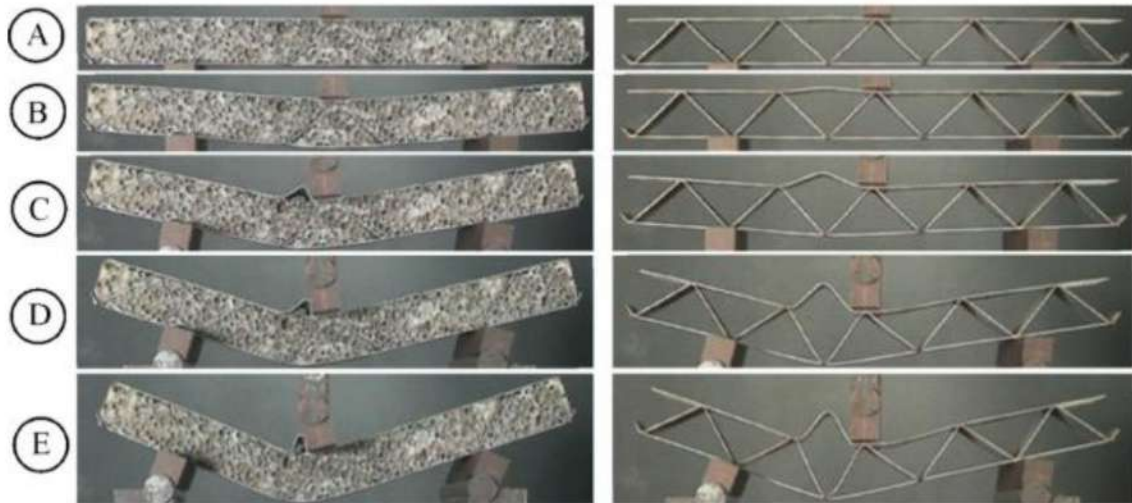
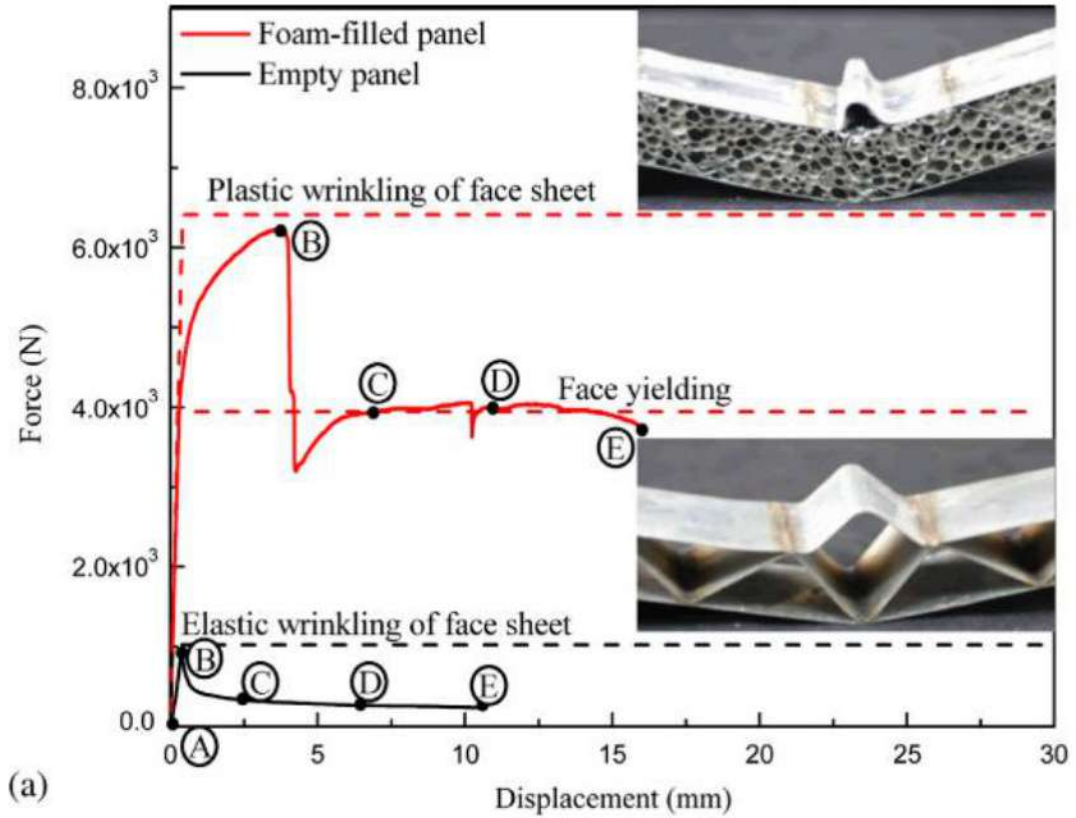


**Figure 1.31:** Transverse bending behavior of empty and foam-filled sandwich beams with corrugated cores (short specimens *e* and *E*, with  $L = 112$  mm; Table 1): (a) force versus displacement curve; and (b) photographs illustrating the deformation history and evolution of failure at selected points marked in (a) [95]

Selver E and Kaya G [96] examined the enhancement of flexural properties in sandwich composites through the insertion of glass and carbon fiber Z-pins. The sandwich panels were fabricated with glass or carbon fiber face sheets and extruded polystyrene (XPS) foam cores reinforced by 3 mm glass and carbon fiber rods. The insertion of reinforcing fibers along the

thickness direction (Z-direction) at two different densities (15 mm and 30 mm) to assess their effect on the flexural properties of the composites. The results demonstrated that the insertion of Z-pins significantly improved the flexural strength and stiffness of the sandwich composites. The enhancement was more pronounced in composites with carbon fiber face sheets compared to those with glass fiber face sheets. Additionally, increasing the Z-pin density further augmented the flexural performance, highlighting the importance of pin density in optimizing the mechanical properties of sandwich composites.

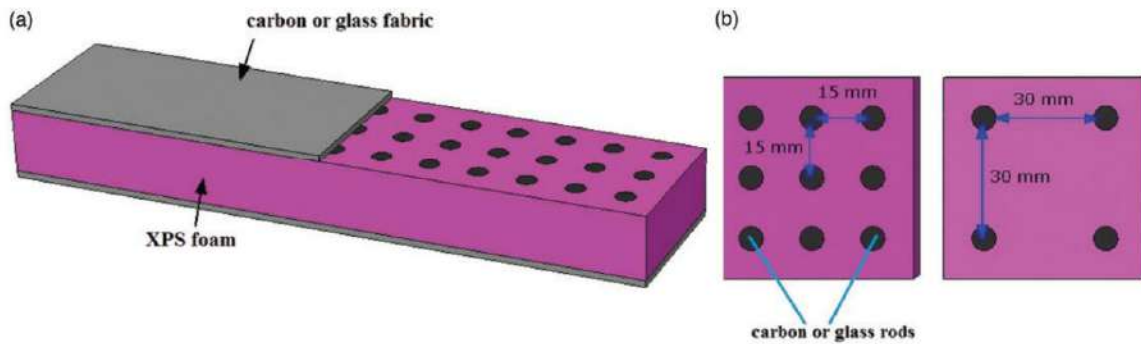


**Figure 1.32:** Illustration of sandwich composite panel (a) and density of the reinforcement rods (15 mm and 30 mm) (b). [96]

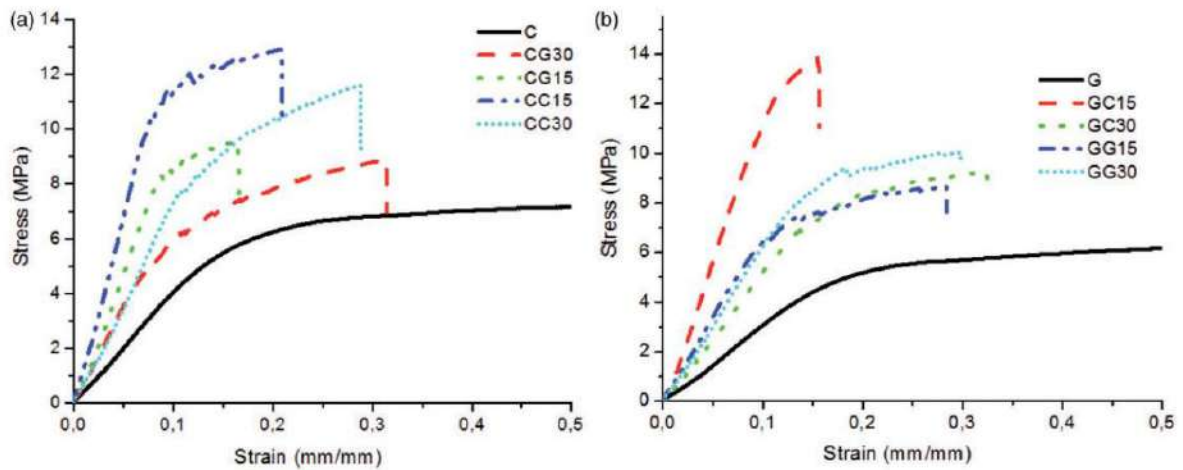


**Figure 1.33:** Stress-strain behavior of sandwich composites subjected to flexural loading: carbon face (a) and glass face (b) sandwich composites [96].

**Table 1. 3** Summary of more research on sandwich panels with different hybrid core.

Refs	Hybrid core configuration	Facesheets	Mechanical effects observed
Lei,H et al. [97]	PVC foam core with z-pins	GFRP-CFRP	Increased compressive strength and energy absorption, delayed core shear
Sayahlatifi, S et al. [98]	Corrugated GFRP layer bonded to balsa wood	GFRP	Hybrid core increased flexural rigidity and damage tolerance
Yungwirth, C.J et al. [99]	Foam or honeycomb core with interlayer hybrids or FGM	Kevlar/carbon hybrid fabrics	Enhanced impact energy absorption and resistance to delamination
Montazeri, A et al. [100]	Auxetic or conventional honeycombs filled with PU foam	3D printed PLA (integrated)	Foam filling increased stiffness and energy absorption
Djama K et al. [101]	GFRP truss core+ PU foam	Hybrid mineral-GFRP skin	High load-carrying capacity, stable progressive failure, and improved energy absorption under both compression and bending.

#### 1.4.4 Incorporation of GFRP in Sandwich Composites

Introducing GFRP as skins in sandwich structures enhances the interaction between the core and face sheets by carrying in-plane and flexural loads, while also protecting the core from damage. Their adjustable fiber orientation and compatibility with various manufacturing processes allows for performance optimization and reliable bonding. Several researchers have examined the inclusion of GFRP skins, confirming their role in improving structural performance and durability [102–104].

Li.J et al. [105] examined the flexural behavior of slab-rib integrated bridge decks with glass fiber-reinforced polymer (GFRP) skin and polyurethane foam core. The study aims to investigate the influences of layers of GFRP face sheets, foam densities, and the existence of webs and cross beams on the flexural performance of these composite decks. The experimental setup involved testing nine slab-rib integrated sandwich decks under four-point flexural loads.



The specimens varied in the number of GFRP layers foam densities, and the presence of vertical and horizontal webs and cross beams. The results showed that the existence of vertical webs significantly improved the debonding resistance of the face sheets from the foam core, increasing the ultimate load by 59% compared to specimens without webs. Increasing the number of GFRP layers from 2 to 4 and 6 resulted in 100% and 214% increments in ultimate loads, respectively. The study concluded that the addition of vertical webs and increasing the number of GFRP layers are effective methods to enhance the load-carrying capacity and rigidity of slab-rib integrated sandwich decks.

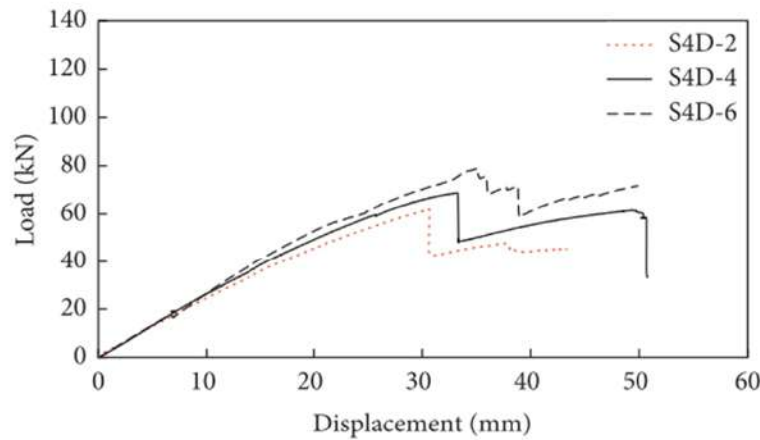


**Figure 1. 34:** Load-displacement curves of S4D with different GFRP layers on the compressive region [105].

Fang et al. [106] investigated the mechanical performance of innovative glass fiber-reinforced polymer (GFRP)-bamboo-wood sandwich beams through experimental and modeling studies. The research aimed to examine the effects of GFRP and bamboo layer thicknesses on the structural performance under bending loads. The experimental program involved testing nine specimens with varying GFRP and bamboo layer thicknesses and different fiber orientations within the wood core. Results indicated that increasing the thickness of both the bamboo and GFRP layers significantly enhanced the flexural stiffness and ultimate load capacity of the sandwich beams. The study identified optimal thicknesses of 6 mm for the bamboo layer and 4.5 mm for the GFRP layer, achieving the best material efficiency in stiffness improvement. Additionally, the modeling results, validated through experiments, confirmed that the proposed sandwich beam design could minimize self-weight and cost while maintaining satisfactory mechanical performance.

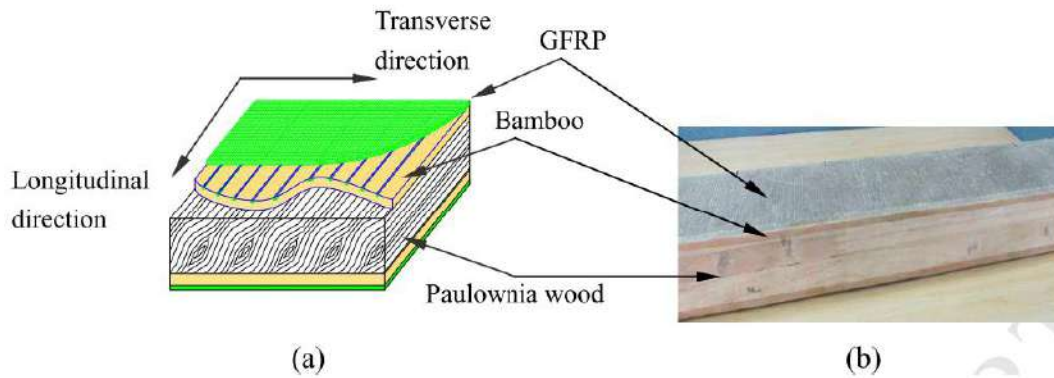


**Figure 1. 35:** GFRP-bamboo-wood sandwich specimen (a) schematic plot and (b) fabricated specimen [106].

Ridlwan et al. [107] conducted a study examining the mechanical properties of sandwich composites composed of Glass Fiber Reinforced Polymer (GFRP) as the skin and 3D-printed Polylactic Acid (PLA) as the core. The research aimed to investigate the tensile and flexural strength of these composites under varying configurations of core and skin thickness. The experimental procedure adhered to ASTM D638 and ASTM D790 standards for tensile and bending tests, respectively. The findings revealed that incorporating GFRP skin significantly enhanced the tensile strength of the composites, with the highest value of 55.74 MPa achieved using four layers of GFRP. However, the addition of GFRP skin had a minimal impact on flexural strength, with the highest value recorded at 50.36 MPa using three layers of GFRP. The study concluded that while GFRP skin is highly effective in improving tensile strength, its influence on flexural strength remains limited.

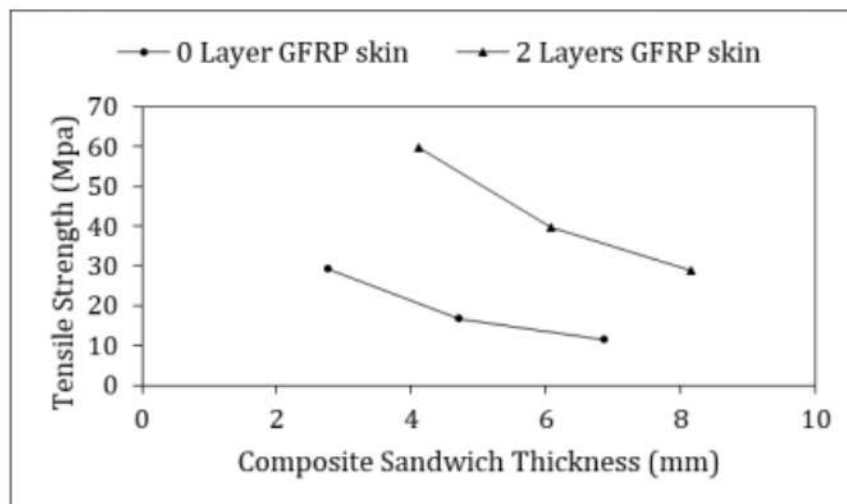


**Figure 1. 36:** Tensile strength of sandwich composite produced with different core [107]

Xie H et al. [108] conducted a study on the development of an innovative composite sandwich matting featuring glass fiber-reinforced polymer (GFRP) face sheets and a paulownia wood core. The primary objective was to design, fabricate, and experimentally validate a novel composite sandwich structure tailored for applications in military engineering, emergency rescue, and large-scale infrastructure construction. The sandwich matting was fabricated using the vacuum infusion molding process (VIMP), and its flexural properties were assessed through four-point bending tests. Experimental results demonstrated that the matting exhibited strong structural integrity under transverse loading, characterized by a substantial plateau phase post-initial failure, effectively mitigating the risk of catastrophic collapse. Additionally, finite element analysis (FEA) closely aligned with the experimental findings, accurately predicting the load- displacement behavior.

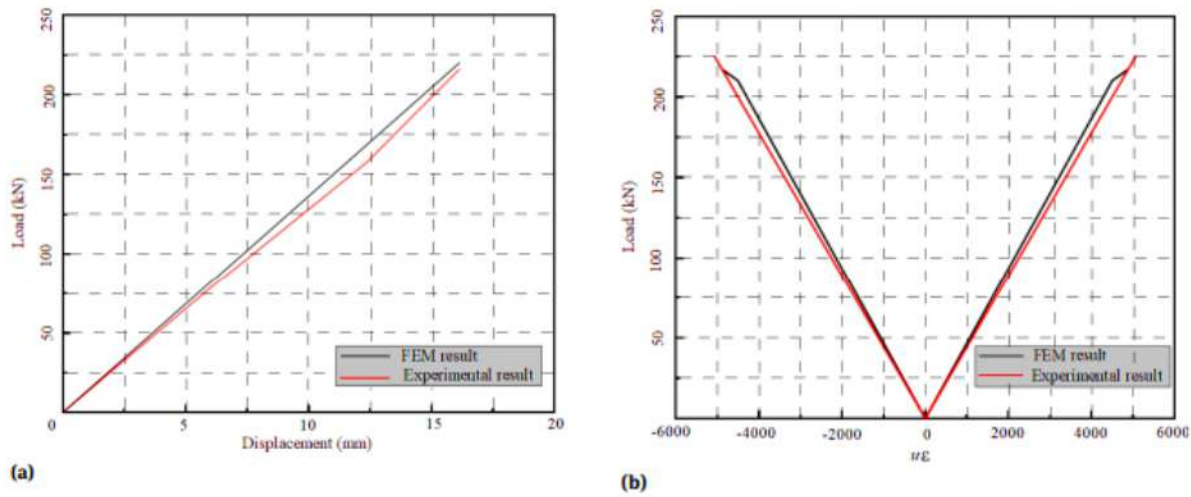


**Figure 1. 37:** Comparison between test result and FEA result. (a) load displacement curve, (b) load strain curve [108].

The study of Dalfi HK and AL-Obaidi [92] investigated how incorporating thermoplastic particles into the core of sandwich composites affects their mechanical properties. The researchers fabricated sandwich panels using GFRP face sheets produced through vacuum bagging, paired with cores hybridized by adding varying percentages of high-density polyethylene (HDPE). The objective was to assess the impact of core hybridization on the panels' flexural strength and energy absorption capabilities. Experimental results demonstrated that increasing HDPE content in the core led to significant improvements in mechanical performance. Specifically, sandwich samples with 8%, 12%, and 16% HDPE in their cores exhibited increases in specific absorbed energy by 413%, 520%, and 620%, respectively, compared to non-hybrid counterparts. These enhancements are attributed to the synergistic



effect of the GFRP face sheets and the hybridized core, which together improve load distribution and energy dissipation under stress. The study concludes that the combination of GFRP face sheets with HDPE-hybridized cores results in sandwich composites with superior mechanical properties, making them suitable for applications requiring high strength-to-weight ratios and enhanced energy absorption.

### **1.5 Failure mode of sandwich structures**

Sandwich panels may experience various types of failure, each imposing a distinct limitation on the panel's load-bearing capability. The dominant failure mode is influenced by factors such as the panel's geometry and the type of loading applied. Failure of the sandwich may be driven by strength of the face sheets, core material, or the adhesive interface. It may also result from local instability phenomena like face wrinkling or dimpling, or from global instability mechanisms such as general buckling or shear crimping [58,109]. These possible failure modes are depicted in *Fig 1.38*.

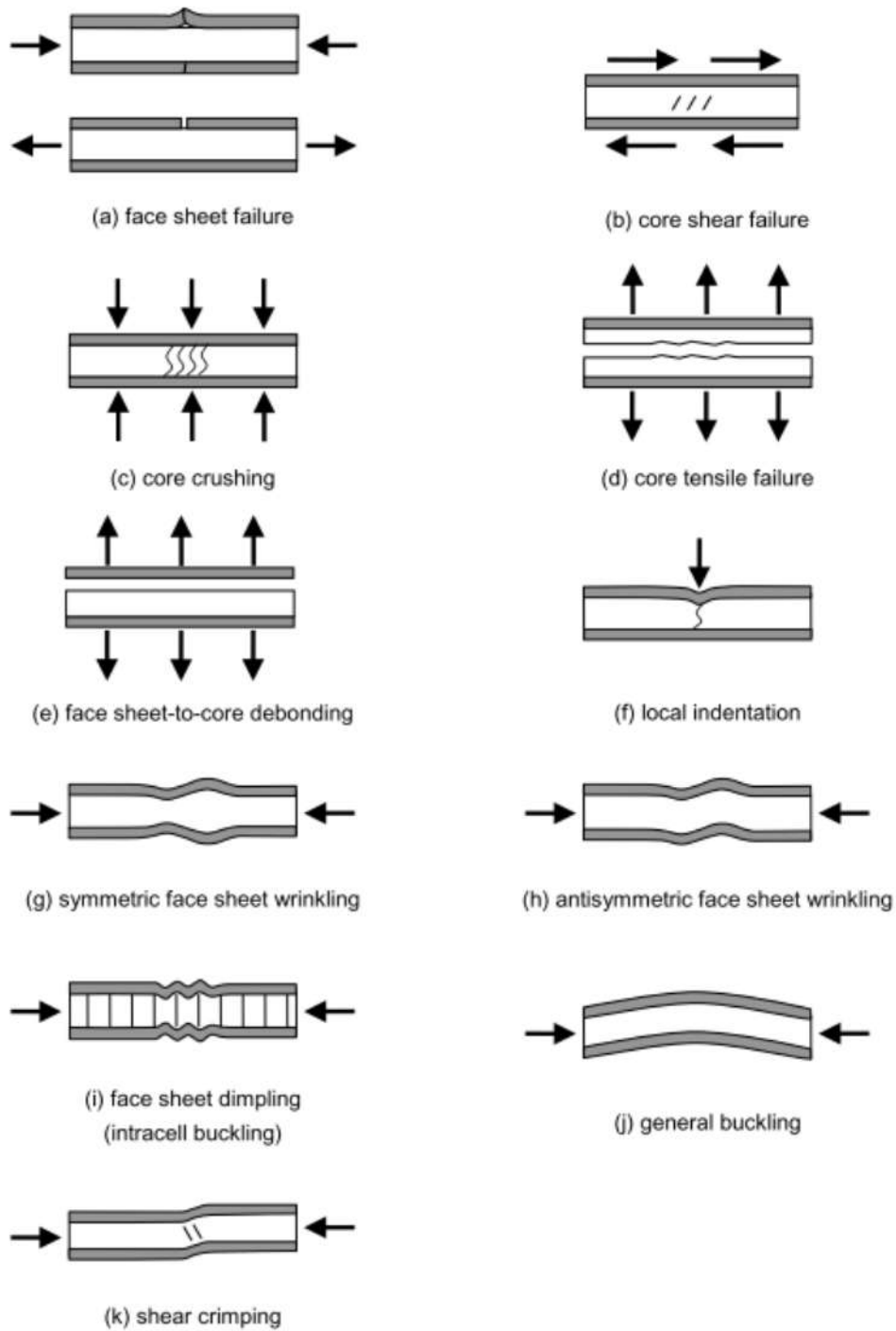


**Figure 1. 38:** Failure mechanisms of sandwich structure [58].

### 1.6 Application of digital image correlation for studying the behavior of materials

In order to comprehend and study the deformation and failure mechanisms of composites and sandwich structures, full field measurement is widely used. DIC is one of the used methods. DIC is a non-contact, optical measurement technique based on computer vision. Unlike the classical methods for displacement and deformation measuring such as pointwise strain gauge that only provide local strain at a selected point, DIC detects full field deformation on all over the surface of the sample[110]. The process begins with preparing the specimen surface by applying a random speckle pattern to ensure accurate image tracking. High-resolution images of the specimen are then captured before and during mechanical loading using one or more cameras, depending on whether 2D or 3D measurements are required. These images are analyzed by dividing them into small subsets, and the movement of each subset is tracked using correlation algorithms to calculate displacement fields. From this displacement data, strain distributions are derived through numerical differentiation. The resulting full-field maps provide detailed insights into the material's deformation behavior and are used to analyze mechanical response and identify failure mechanisms[111,112] Recently, numerous researchers have employed DIC to study the deformation of composite plates and sandwich structures[113–118].

Garc et al. [119] investigated damage mechanisms in sandwich structures critical to safety-sensitive components using non-destructive testing methods: Acoustic Emission (AE) and Digital Image Correlation (DIC) *Fig 1.32*. The study analyzed damage initiation during fatigue tests on samples representing the core of an aircraft heat exchanger, composed of alternating hot and cold fins separated by parting sheets. Three geometrically identical samples (25 mm<sup>2</sup> section, 30 mm height) were tested under accelerated, non-accelerated, and damage tolerance fatigue conditions using an MTS Landmark Servohydraulic Test System with a 100 kN capacity. The DIC system, incorporating a Basler acA1300-75gm camera synchronized at 20 fps and a stochastic pattern applied to the samples, identified strain redistributions as damage indicators. AE monitoring, conducted using XARION microphones (Eta250 Ultra and Eta450 Ultra) with broadband frequency detection (up to 1 MHz and 2 MHz), captured acoustic signals correlating with damage progression. Accelerated fatigue tests showed early high-frequency acoustic events, signaling rapid damage initiation. In non-accelerated tests, damage developed more gradually but escalated before rupture. In damage tolerance tests, pre-existing cracks exhibited high acoustic activity near failure. AE demonstrated superior sensitivity to early damage detection, while DIC effectively highlighted strain evolution at later stages.

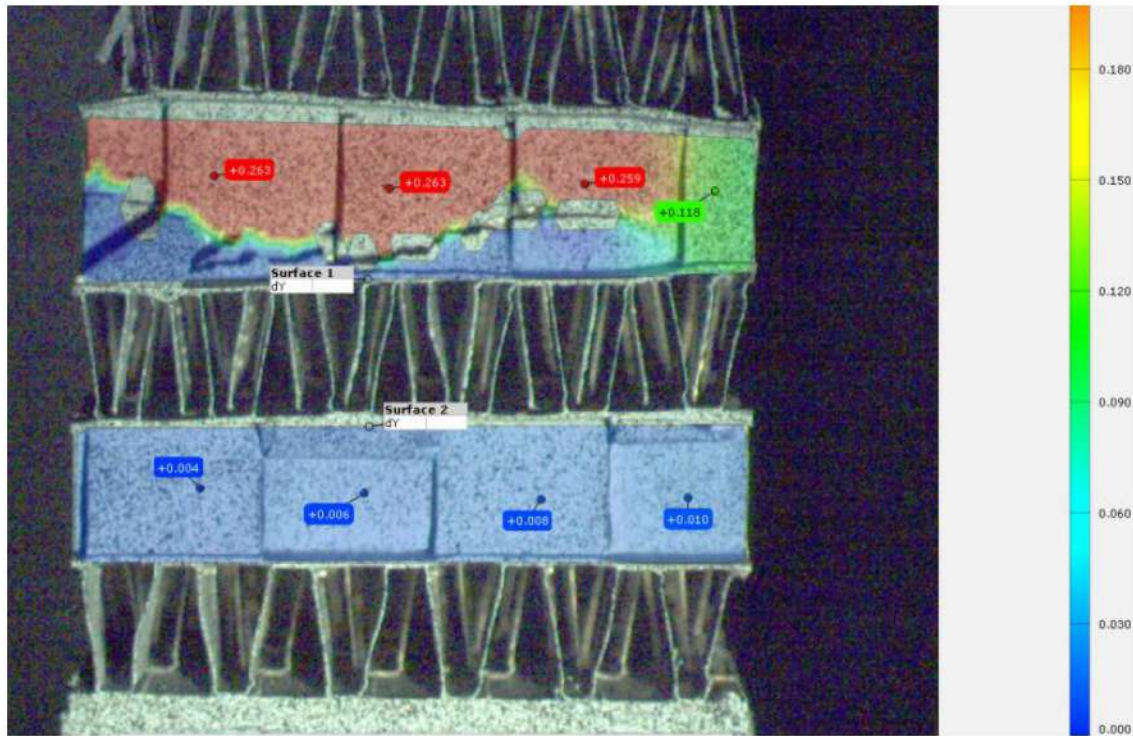


**Figure 1. 39:** DIC analysis of the final condition of the structure following damage tolerance testing [119].

Fathi et al. [120] conducted a study to investigate the shear deformations of three common structural core materials using Digital Image Correlation (DIC). The aim was to utilize full-field optical analysis to examine the shear response of extruded PET foam, cross-linked PVC foam, and Balsa wood. For this purpose, sandwich specimens were fabricated with glass fiber/epoxy laminate sheets on both sides of the core materials. The DIC system consisted of two high-speed cameras for capturing images, a controller to manage the cameras, and a computer for data acquisition and results evaluation. The specimens were tested in four-point bending in accordance with ASTM C 393, with loading and support span lengths of 150 mm and 500 mm, respectively. The study found that foam cores exhibited more uniform deformations in the elastic region compared to Balsa wood. PVC foam showed significant local deformation under the load introduction bars, which led to sub-interface shear failure. In contrast, PET foam displayed no signs of stress concentration, resulting in homogeneous shear deformations in the mid-core regions. The DIC measurements effectively captured strain evolution and redistribution, offering valuable insights into the failure mechanisms and performance of sandwich structures.



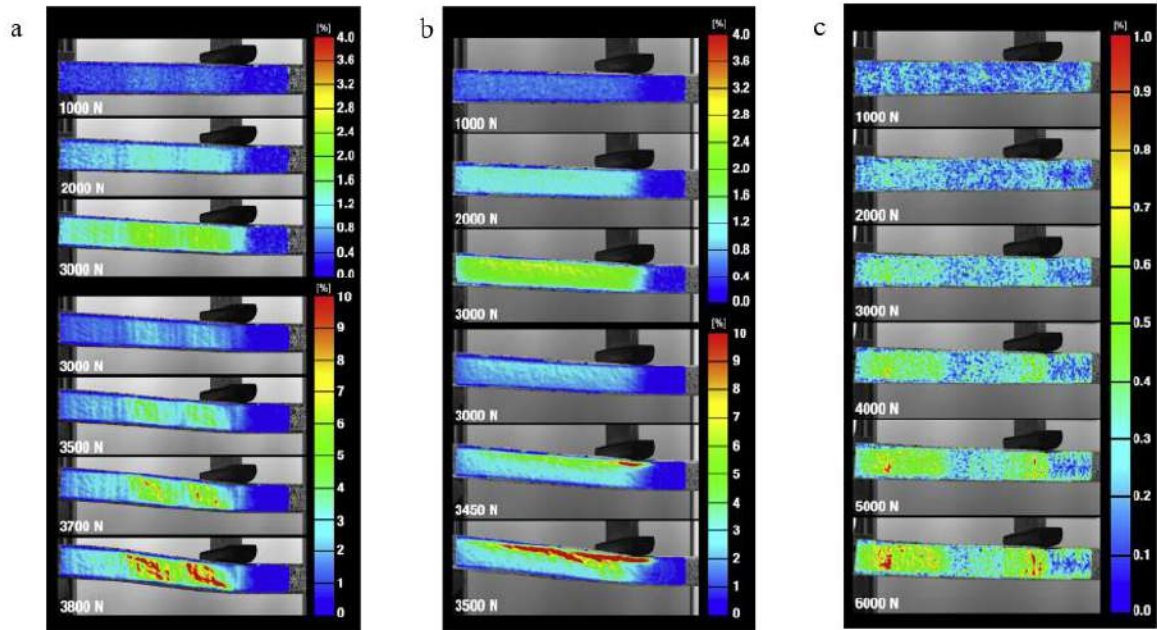


**Figure 1. 40:** Distribution of Shear Strains on the Surface of (a) PET Foam Core (Airex T92.100), (b) PVC Foam Core (Airex C70.55), and (c) Balsa Core (Baltek SB.50) Sandwich Beams at Different Mid-Load Levels [120].

## 1.7 conclusion

This chapter provided a comprehensive overview of composite materials, focusing on Glass Fiber Reinforced Polymers (GFRP) composites and their use in sandwich structures. It covered the identification and classification of composite materials, with an emphasis on GFRP, including various manufacturing techniques such as injection molding, compression molding, and hand lay-up processes. The applications and performance of GFRP in sandwich structures were discussed, along with the role of foams like Polyurethane (PU) and Polystyrene (PS) and different hybrid foams in enhancing their properties. Lastly, the use of digital image correlation for studying sandwich structure behavior was introduced. This theoretical background sets the stage for the experimental work that follows in the next part.

*Part I*  
*Materials and*  
*methods*

***CHAPTER 02***  
**MATERIALS AND**  
**EXPERIMENTAL**  
**METHODS**

# CHAPTER 02. MATERIALS AND EXPERIMENTAL METHODS

---

## 2.1 Introduction

This chapter presents a comprehensive and detailed description of the materials, methods, and experimental procedures employed throughout this research. It begins by outlining the selection and preparation of materials, including the UP resin, GFRP plates, PU and PS foams. The fabrication processes for the GFRP plates and sandwich structures, as well as the introduction of innovated hybrid core. The chapter also details the specific techniques and standards employed in the mechanical testing, including compression, shear, and flexural tests, to evaluate the mechanical characteristics of the materials and sandwich structures. SEM analysis is explained as a tool for examining microstructural features, including skin-core adhesion and failure modes. By providing a clear and thorough explanation of the experimental methodology, this chapter lays a strong foundation for interpreting the results and ensures the reliability and validity of the findings presented in subsequent chapters.

## 2.2 Materials used

This study investigates three distinct configurations of sandwich structures, all utilizing GFRP plates as skins. The first configuration consists of a sandwich structure with a PU foam core (SPU), designed to evaluate the performance of flexible, lightweight core material. The second configuration (SPS), incorporates a PS foam core, chosen for its higher stiffness and thermal insulation properties compared to PU. The third configuration, SRP, introduces a reinforced core with integrated pins, aimed at enhancing the structural integrity and interfacial bonding between the skins and the core. These configurations were developed to compare their mechanical under various conditions and explore their potential for advanced engineering applications.

### 2.2.1 Skin

#### 2.2.1.1 UP resin

The resin used is unsaturated Polipol 353 polyester (UP) resin with a density of  $1.121 \text{ g/cm}^3$ . To prepare the matrix, the resin was poured into a cup and weighed after the cup was tared.



Subsequently, 0.25% of each Mek-P hardener and Cobalt accelerator were added. The mixture was agitated slowly to avoid the formation of air bubbles.

### 2.2.1.2 Glass fiber

E-glass Chopped Strand Mat (CSM) was used as skin reinforcement. Two areal weights, 300 g/m<sup>2</sup> and 600 g/m<sup>2</sup>, were incorporated in this study. **Fig 2.1** illustrates the glass fiber.



**Figure 2. 1:** E-glass CSM fibers a) 300g/m<sup>2</sup>, b) 600g/m<sup>2</sup>

### 2.2.1.3 GFRP plates fabrication

The GFRP plates were fabricated using the hand lay-up method on a 50x50 cm<sup>2</sup> smooth glass plate to achieve a uniform surface finish. This process involved layering chopped strand mat E-glass fibers as the reinforcement material, with UP resin as the matrix. Before manufacturing, the glass fiber sheets were weighed, and the resin was measured at twice their weight. To begin, the glass plate was cleaned thoroughly to ensure no contaminants affected adhesion then a mold release was applied on the plate to easily remove the GFRP plates after hardening. Next, a thin layer of UP resin was then applied to the plate, followed by placement of the first layer of 300 gr/m<sup>2</sup> glass fiber mat. Subsequently, a layer of UP resin and three layers of 600 gr/m<sup>2</sup> glass fiber were added manually, ensuring even distribution and removal of air bubbles using a roller to minimize void content. chopped strand mat glass fiber; four layers of mat, the outer layer of 300 gr/m<sup>2</sup> glass fiber and three layers of 600 gr/m<sup>2</sup> glass fiber. After achieving the desired thickness, the laminate was left to cure at room temperature for a specified period. Once cured, the GFRP plate was carefully removed from the glass plate, trimmed to the required dimensions, and post-cured if necessary to enhance mechanical properties. A CNC machine was used to cut the specimens from the plate of 45x45 cm<sup>2</sup> into the desired shapes, 5 cm was removed from all the edges of the plates to avoid discrepancy in thickness. **Fig 2.2** presents the process and the molded GFRP plate. **Fig 2.3** demonstrates the SEM analysis of the manufactured GFRP plate.

The SEM analysis demonstrates strong interfacial adhesion between the glass fibers and polyester matrix. Micrographs confirm that the hand lay-up technique resulted in uniform resin distribution, enhancing the structural integrity of the skin.

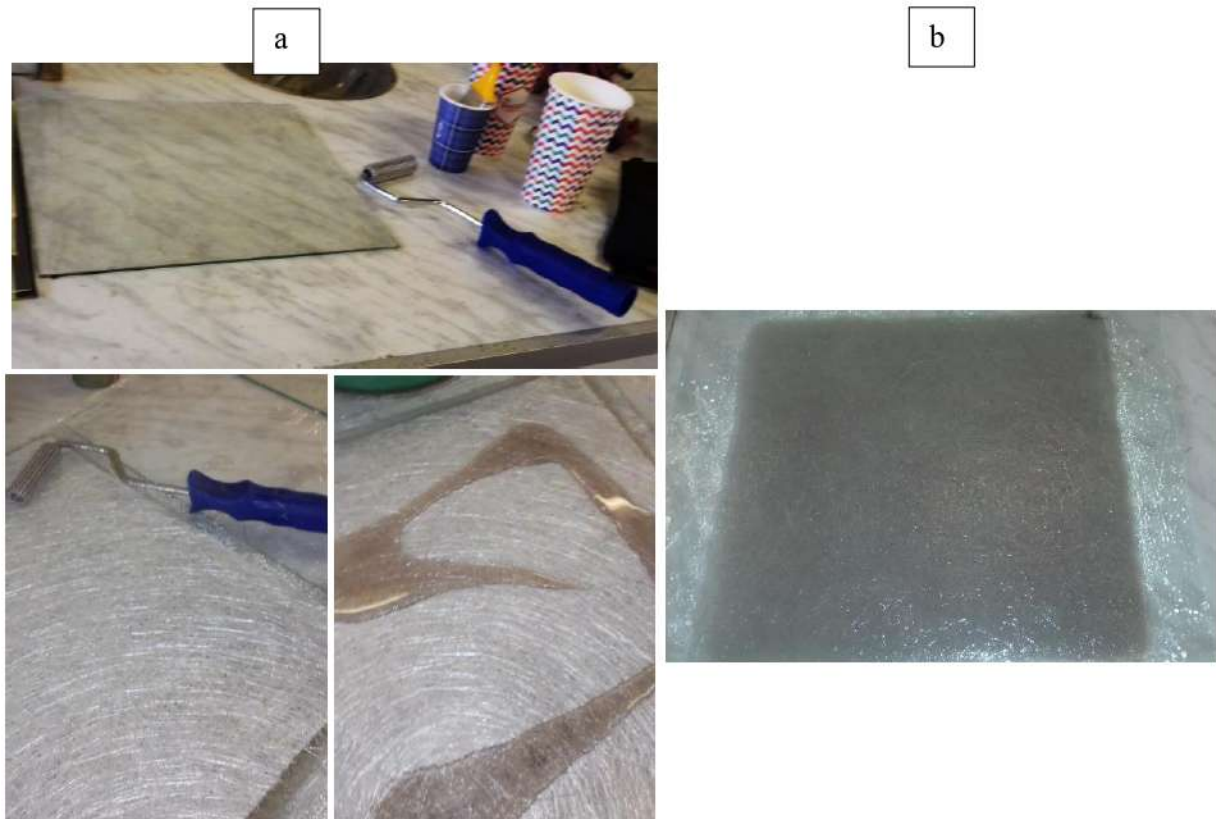


**Figure 2. 2:** a) Process of making GFRP plate, b) Molded GFRP plate.

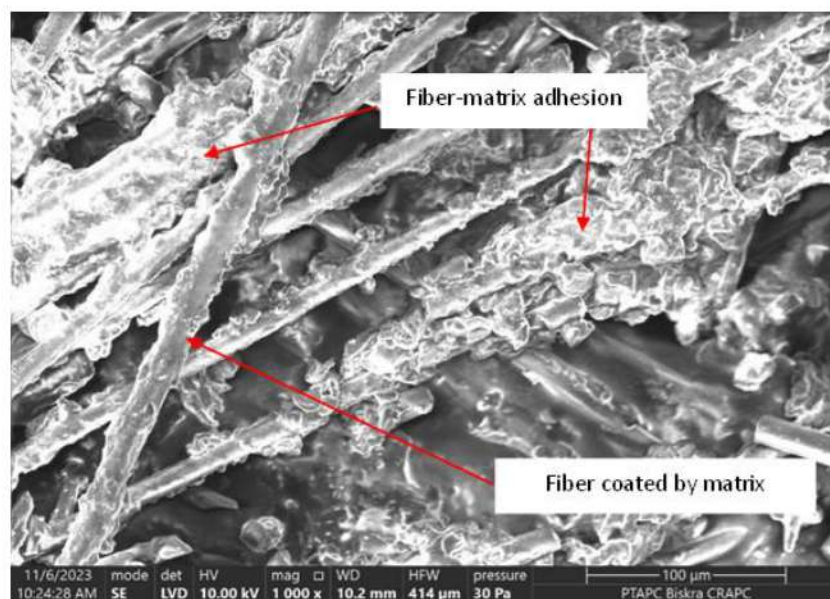


**Figure 2. 3:** SEM images of manufactured GFRP plate.



#### 2.2.1.4 Fiber content of GFRP plates.

Fiber content was determined by following the standard ISO 1172 [121]. To perform calcination, the following steps must be followed:

- Cutting three samples of 20x20mm of GFRP plates.
- Place the sample in a crucible to weigh it using the balance with a precision of  $10^{-3}$  g.
- Place the sample in an oven at  $650^{\circ}\text{C}$  for six hours.
- Take the fibers after calcination and place them in a desiccator for cooling and to absorb moisture for one hour.
- Weigh the obtained fibers.
- Place the fibers in the oven at  $650^{\circ}\text{C}$  for one hour to ensure complete calcination of the resin.
- Weigh the fibers a second time.

**Table 2.1** resumes the fiber content obtained. It was calculated using eq (1). Where  $w_1$ ,  $w_2$  and  $w_3$  are the weights of crucible, crucible with the sample and crucible with sample after calcination, respectively. As it can be seen that the reel values of the fiber content are different from the ones used while manufacturing the plates. This difference can be explained by: that the specimens of the calcination are too small compared to the manufactured plates, the distribution of the resin in the plates is not uniform. **Fig 2.4** presents the samples before and after calcination.

$$wf = \frac{w_3 - w_1}{w_2 - w_1} \quad (1)$$

**Table 2.1** Fiber fraction for GFRP skins.

	Sp 01	Sp 02	Sp 03	Average
<b>Fiber fraction</b>	36%	36.97%	36.69%	36.55%

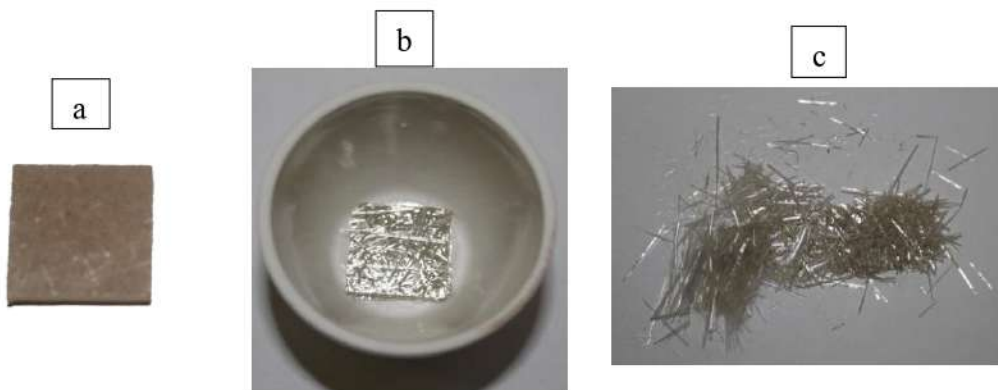


**Figure 2. 4:** a) sample of 2x2 mm for calcination, b) sample after calcination, c) fibers after calcination.

## 2.2.2 Core

### 2.2.2.1 PU and PS foams

The PU foam used was manufactured in the laboratory. Using Polyol-Component and Iso-Component with a ratio of 1:1.16. According to the technical data sheet provided by the company the density of the mixture with this ratio is  $50\text{kg/m}^3$ . After stirring the mixture very quickly, it was poured in a mold coated by mold release. The mold was designed to ensure the thickness of  $20\pm 2\text{ mm}$  (*Fig 2.5a*). The foam was left to rise and hardened for 72h in a room temperature  $20^\circ\text{C}$ . After the hardening the blocks of foam were cut into the desired dimensions (*Fig 2.5b*). Expanded PS foam was used as a core with a thickness of 20 mm (*Fig 2.6*)

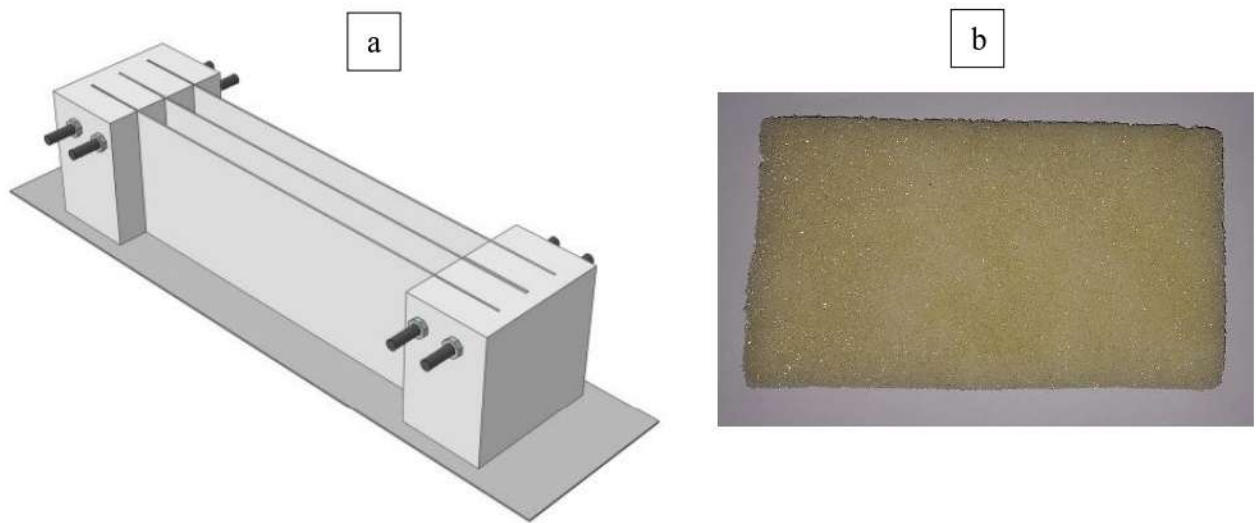


**Figure 2. 5:** a) Mold used for PU foam, b) Sample of PU foam.



**Figure 2. 6:** PS foam.



### 2.2.2.2 Reinforced pins

A silicone mold of 100x100 mm<sup>2</sup> with circular holes of 2 mm diameter and 20 mm length was used to fabricate the GFRP pins. The fabrication process involved two steps: first, glass fiber yarn was cut and inserted into the silicone mold, then the epoxy resin was injected using a syringe. The pins were left to cure at room temperature (25°C) for 72 hours. After curing, the pins were carefully removed from the mold and sanded with fine-grit sandpaper to eliminate any excess resin and fibers. **Fig 2.7** shows the mold and the pins after cure.

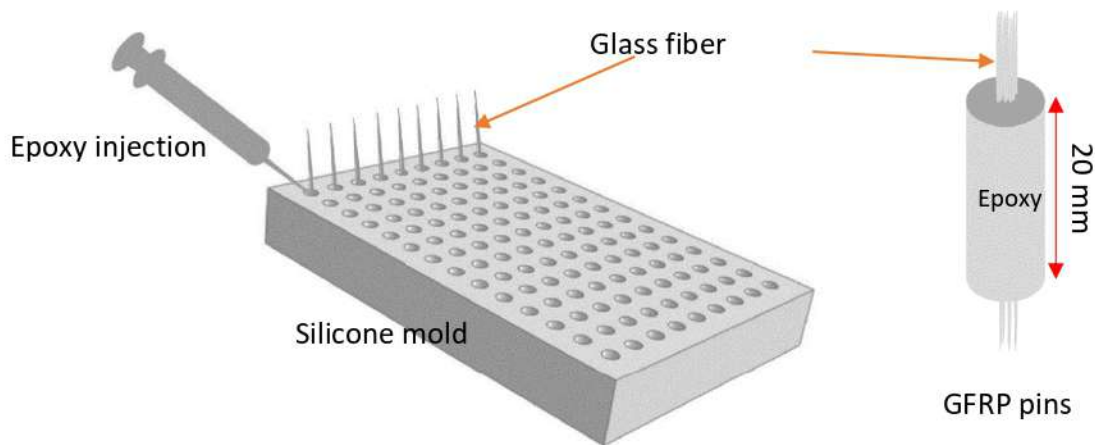


**Figure 2. 7:** Process of fabricating the GFRP pins.

### 2.2.2.3 Fiber content of reinforced pins

Following the same procedure for GFRP skin, the fiber content of reinforced pins was conducted. **Table 1.2** resumes the results of the method and **Fig 2.8** shows the sample after calcination.

**Table 2. 2** Fiber content for reinforced pins.

	Sp 01	Sp 02	Sp 03	Average
<b>Fiber fraction</b>	10.1%	11.9%	10.2%	10.73%



*Figure 2. 8: Sample of reinforced pin after calcination.*

## 2.3 Manufacturing of sandwich structure

### 2.3.1 Sandwich structure with PU and PS core (SPU and SPS)

The sandwich structure was composed of two GFRP skins. First configuration, PU foam was used as core material while the second one was PS foam. The GFRP skin, PU and PS foams were cut to the desired dimensions and arranged in a layered configuration to enhance the overall structural integrity. The sandwich structure was assembled by applying a layer of epoxy resin between the core and the GFRP skins, followed by curing at room temperature for 72 h under cold pressure. *Fig 2.9* shows the constituents of the sandwich structure. To perform DIC technique, spackle pattern was created; the samples were painted with white paint then sprinkled with black paint.



*Figure 2. 9: GFRP skin, PU and PS foams.*

### 2.3.2 Sandwich structure with hybrid core (SRP)

After the fabrication of the reinforced pins as explained in the section 2.2.2.2, the pins were placed in PS foam as demonstrated in *Fig 2.10*. Holes were drilled into the core material at predetermined locations to accommodate the reinforcement pins. The pins were inserted into the holes and secured with epoxy resin to ensure proper bonding and alignment. To ensure an adhesion between the pins and PS foam, the pins were coated with epoxy resin. The prepared core with reinforcement pins was placed between the two GFRP face sheets. A layer of epoxy resin was applied between the core and the face sheets to ensure strong bonding. The assembly was subjected to uniform pressure to ensure proper consolidation and minimize voids. The adhesive was left to cure at room temperature (25°C) for 72h.

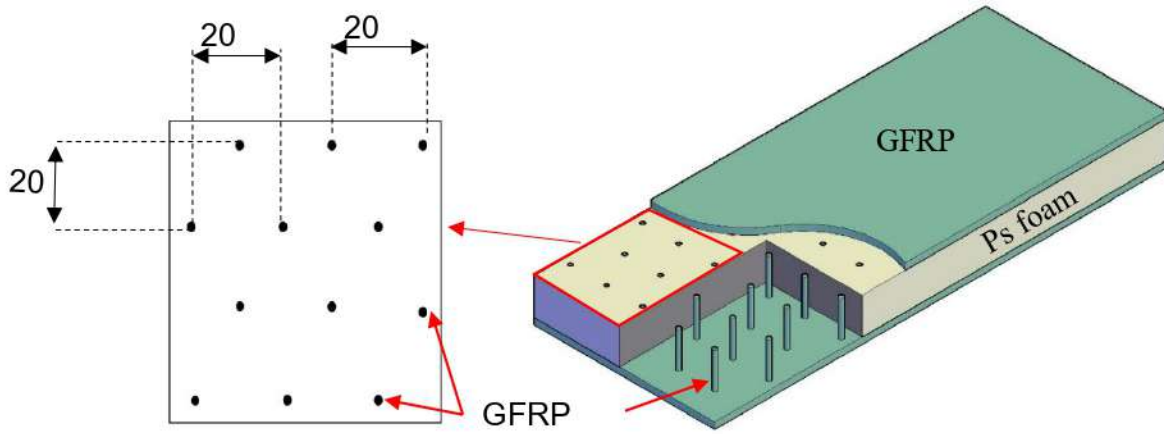


*Figure 2. 10: Position of reinforced Pins in SRP.*

## 2.4 Digital image correlation

The analysis of DIC and the subsequent determination of strain involved the use of an open-source tool for Digital Image Correlation (2D) Ncorr [122], which is a post-processing tool from MATLAB. To measure the displacement and strain, DIC-Ncorr code uses subsets of pixels; subset radius which refers to the size of a circular or square subset or region of interest (ROI) that is used to track and analyze the displacement or deformation of an object or material in an image sequence; subset spacing refers to the distance between the centers of adjacent subsets. The primary objective is to choose the smallest subset possible that avoids generating noisy displacement data [123]. In this study, a circular subset radius of 43 pixels and a subset spacing of 3 pixels were selected to achieve optimal accuracy and computational efficiency during DIC analysis. High-resolution images, with dimensions of 5202x3465 pixels, were captured using a CANON 1300D camera throughout the testing process. To ensure synchronization between the test machine data and the DIC results, the recorded timestamps from the test machine were aligned with the timestamps of the images captured by the DIC system. Images were acquired at a consistent frequency of one frame per second, starting from the beginning of the tests. To enhance the quality of the captured images, a high-intensity LED light source was strategically positioned in front of the testing machine. This setup ensured uniform illumination of the specimens, minimized shadowing, and improved image clarity. The experimental configuration, depicted in *Fig 2.11*, was carefully designed to support accurate DIC analysis for both GFRP skins and sandwich specimens. This arrangement provided consistent lighting, precise alignment, and reliable data acquisition across all tests performed.



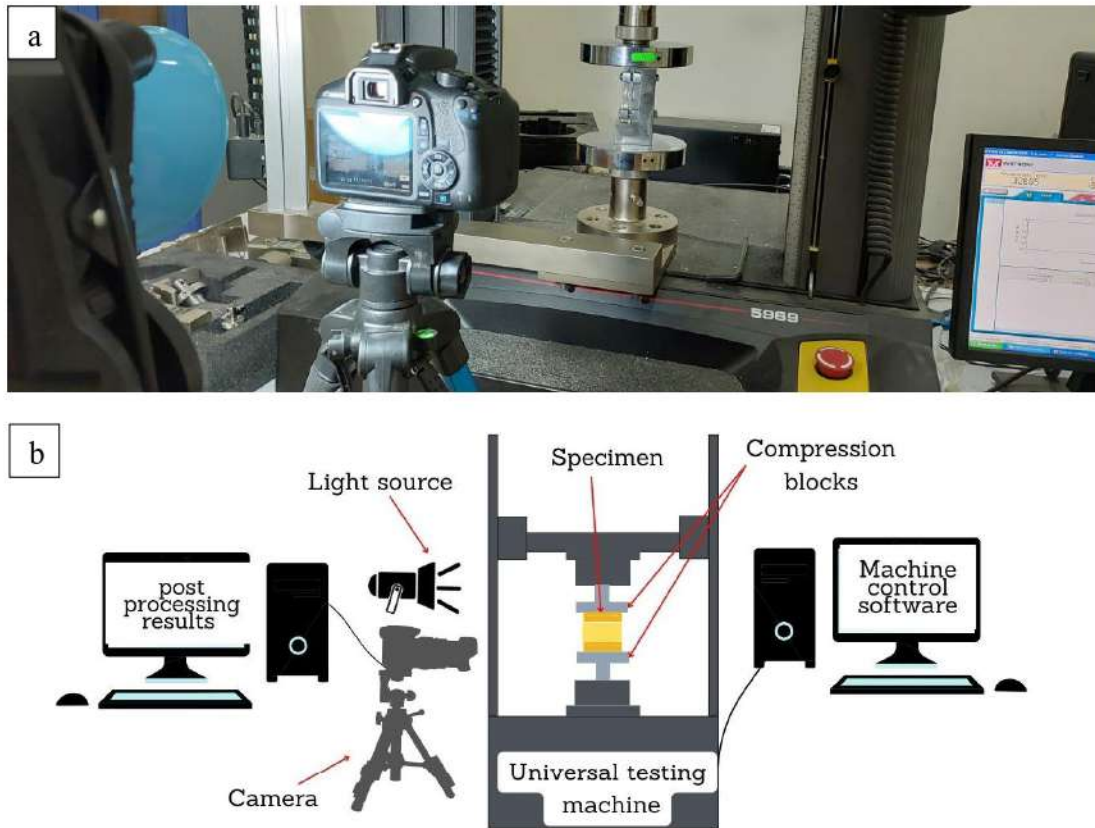


*Figure 2. 11: Experimental setup for DIC analysis adopted, a) GFRP skin compression test, b) Flatwise compression for sandwich.*

## 2.5 Mechanical testing

### 2.5.1 UP resin properties

To obtain the mechanical properties of the resin, tensile test was conducted according to ASTM D638-14 [124]. That is why a mold of silicone was prefabricated with dimensions suggested by the standard. The resin was poured into the mold and left to cure for 72h in room temperature (25°). Once hardened, the specimens were colored with white paint and then speckled with black paint to form a random spackle pattern for DIC analysis. **Fig 2.12** illustrates the silicone mold used, the specimen after curing and its dimensions. The thickness of the samples was  $5.5 \pm 0.14$  mm.



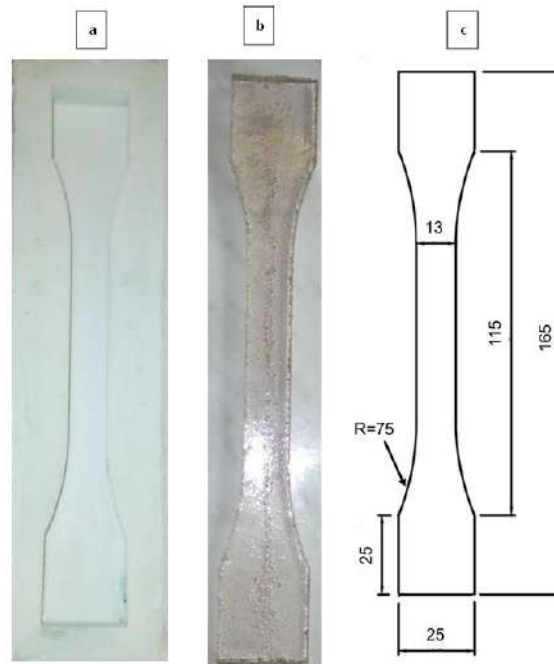


**Figure 2.12:** a) Mold of silicone, b) Specimen, c) Specimen dimensions (in mm).

## 2.5.2 GFRP mechanical testing

### 2.5.2.1 Tensile test

In order to investigate the mechanical performance of GFRP skin, experimental studies were carried out using the Instron 5659 Universal testing machine. The mechanical properties of GFRP skin were investigated through tensile test in accordance with ASTM D638-14 [124]. Each specimen was clamped at both ends and subjected to uniaxial tensile loading at 0.5mm/min crosshead speed. During the test, load and displacement data were continuously recorded to calculate the tensile properties. **Fig 2.13** displays the specimens studied and their dimensions. To create a random speckle pattern for DIC analysis the specimens were coated with white paint and subsequently sprinkled with black paint.

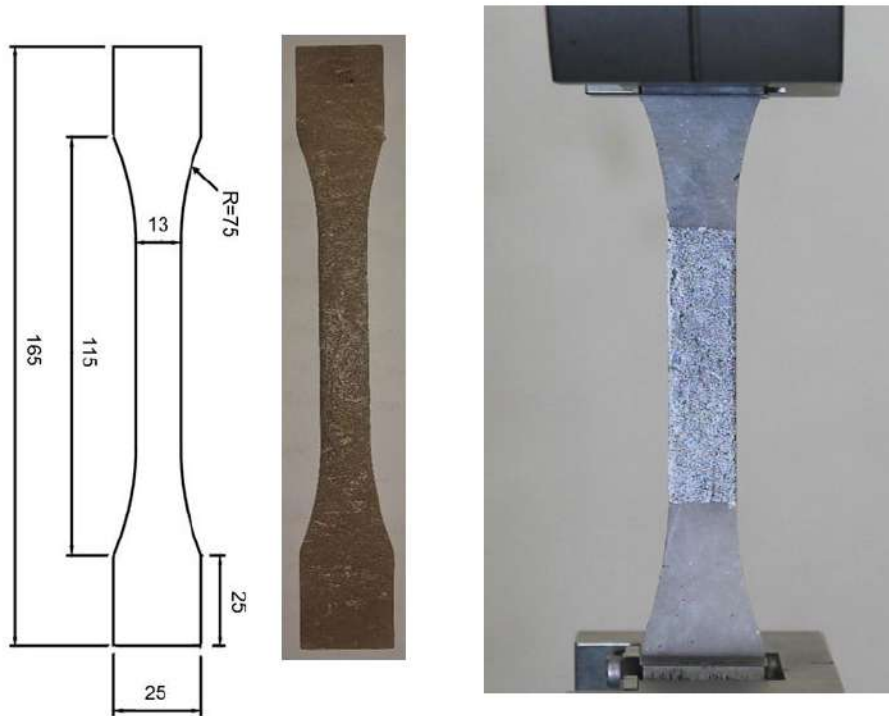


**Figure 2. 13:** Geometry of GFRP skin samples used for tensile test, dimensions are in mm.

#### 2.5.2.2 Compression test

According to the Modified ASTM D695 Compression Test Fixture (Boeing BSS 7260) [125] and ASTM D695-15 [126], the skin compression test was conducted to evaluate the compressive properties of the composite material. These test methods require the application of a uniaxial compressive load while ensuring that buckling is prevented [127], which is critical for obtaining accurate material properties. The compression fixture, shown in **Fig 2.14**, consists of a clamping mechanism with a bolted assembly, designed to provide uniform load distribution and prevent premature failure due to misalignment or bending. Due to the specimen's interface being enclosed within the fixture, the speckle pattern required for DIC analysis was applied to the side surface of the specimen, ensuring effective tracking of strain distribution during the test.

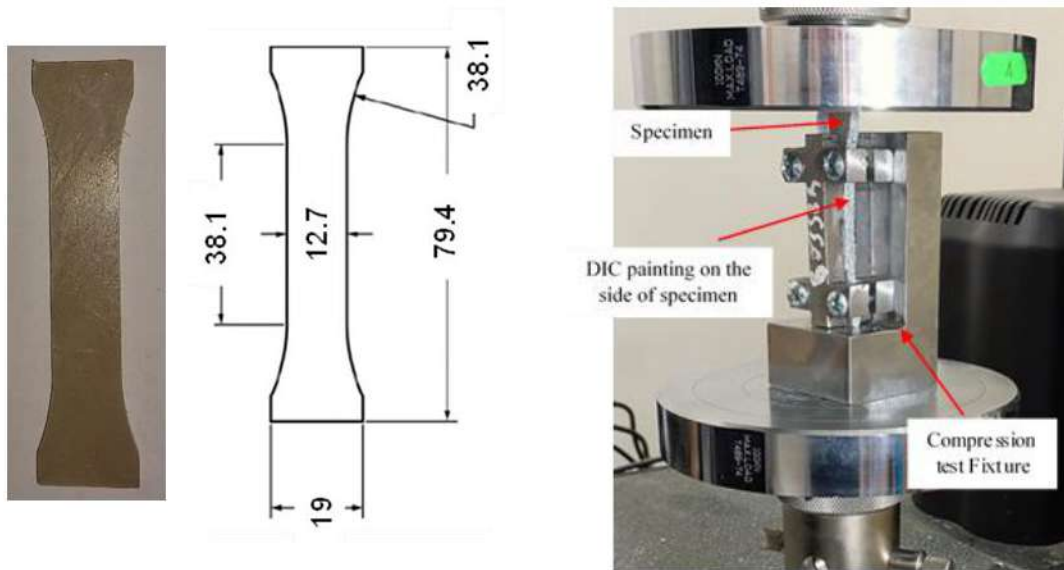


**Figure 2. 14:** a) Geometry of GFRP skin samples used for compressive test, dimensions are in mm. b) Modified compression test fixture.

### 2.5.2.3 Flexural test

#### 2.5.2.3.1 Three- and four-point bending

Three- and four-point bending tests were conducted on GFRP plates in accordance with BS EN ISO 14125:1998 [128] to assess flexural properties such as flexural strength, modulus, and failure modes. The test specimens were prepared with dimensions of 80 mm length, 15 mm width and  $4.2 \pm 0.18$  mm thickness. For the three-point bending test, the specimen was supported at two outer points. The support span length,  $L'$ , was set to 64 mm, with the loading support positioned at the center. In the four-point bending test, the load was applied at two points. The outer support span,  $L''$ , was set to 66 mm, while the inner span of the loading supports,  $l''$ , measured 22 mm. Both setups were conducted under a speed rate of crosshead of 0.5mm/min. Load-displacement data were obtained for the calculation of flexural properties. The spackle pattern was applied in the side of specimen to perform DIC analysis. **Fig 2.15** demonstrates the tests setup.

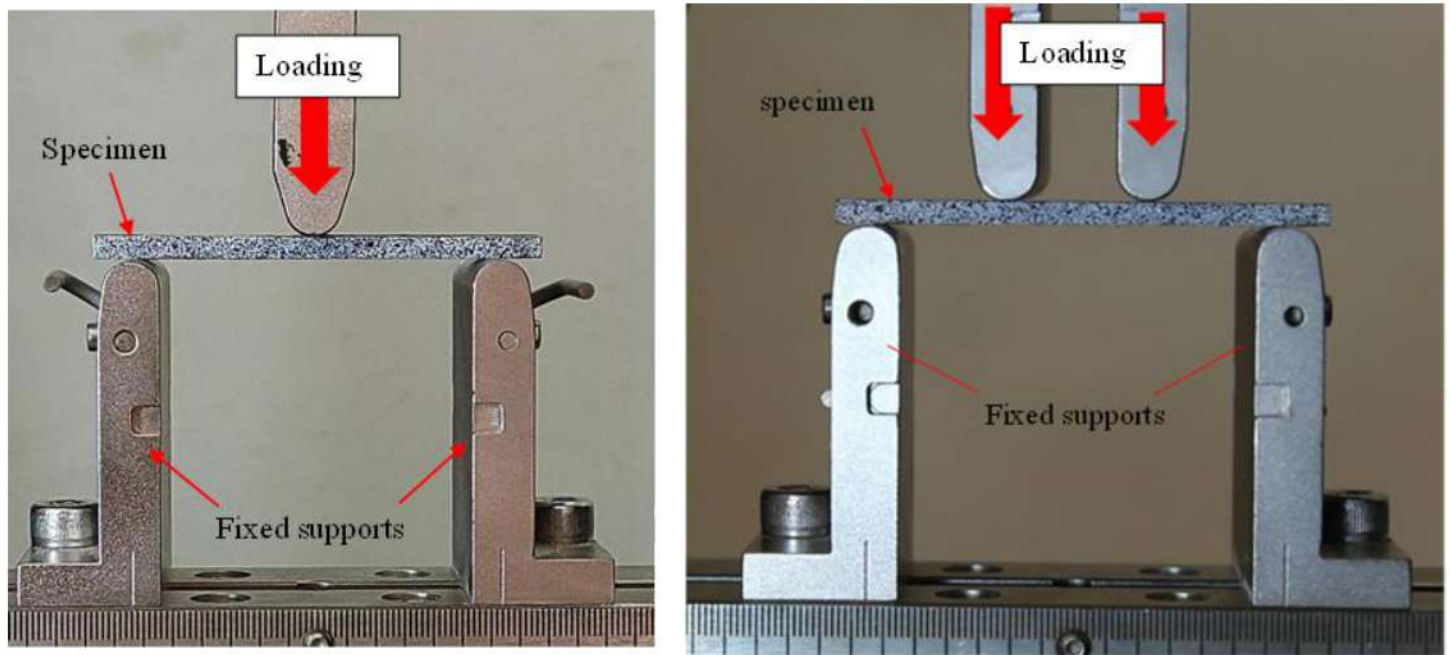


Figure 2.15: a) Three-points test. b) Four-points test.

### 2.5.3 Mechanical testing of sandwich structures

#### 2.5.3.1 Edgewise compression test

To study the mechanical behavior of sandwich structure, the edgewise compression test was performed according to ASTM D364 [129]. The compression load was applied on the specimens using an edgewise fixture and cylindrical loading blocks, **Fig 2.16** shows the test setup. The rate of displacement of crosshead for both tests was 0.5 mm/min, the bottom plate was fixed and the load was applied using the top plate. Two different geometries of samples were studied under edgewise compression load;  $w=L$  (S-60) and  $w<L$  (S-200). **Table 2.3** summarized the geometrical properties of sandwich structure studied. During the test, load and displacement data were continuously recorded, providing insights into the compressive strength, failure modes, and stability of the sandwich structure under edgewise compression. To perform DIC technique, spackle pattern was created; the samples were painted with white paint then sprinkled with black paint.



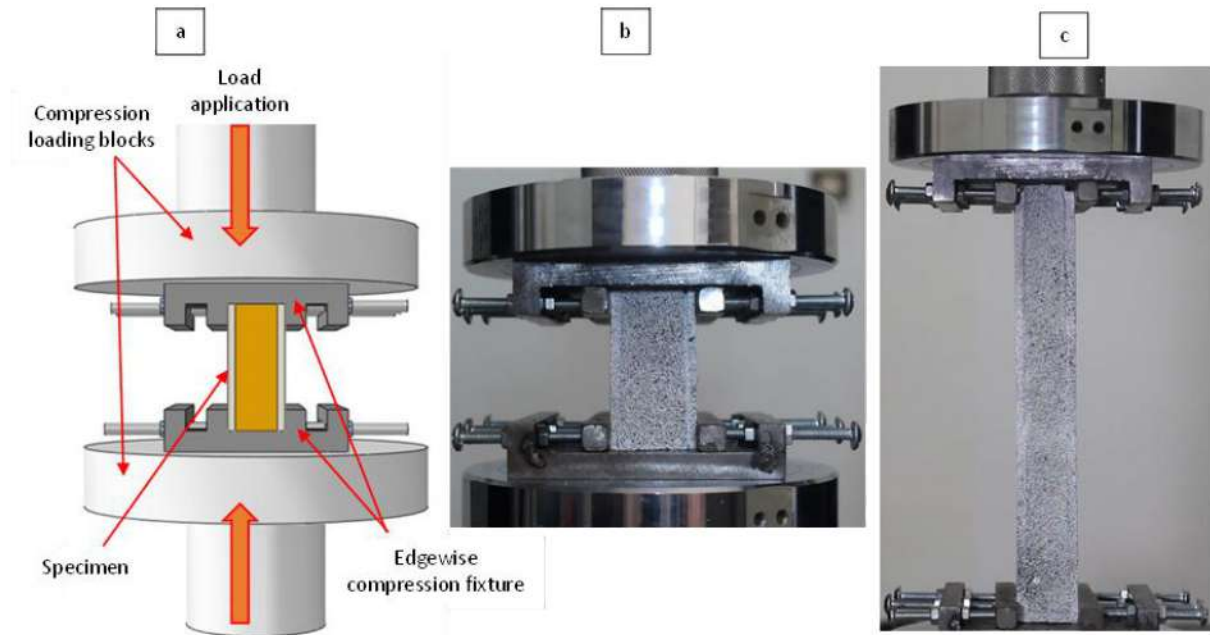


**Figure 2. 16:** a) Edgewise compression setup, b) S-60, c) S-200.

### 2.5.3.2 Flatwise compression test

A flatwise compression test was performed on sandwich structure specimens to determine their compressive strength and behavior under loading, in accordance with ASTM C365 [130]. This test method evaluates the compressive properties of sandwich core materials when loaded perpendicular to the skin of the sandwich structure. Specimens were prepared with dimensions specified by the standard (see Table 2.3). The load was applied on the specimens using cylindrical loading blocks with a rate of speed of 0.5 mm/min. Both the load and displacement were continuously recorded during the test. The compressive strength, failure modes, and other mechanical properties of the sandwich structure were assessed based on the recorded data. A spackle pattern was created to perform DIC technique.

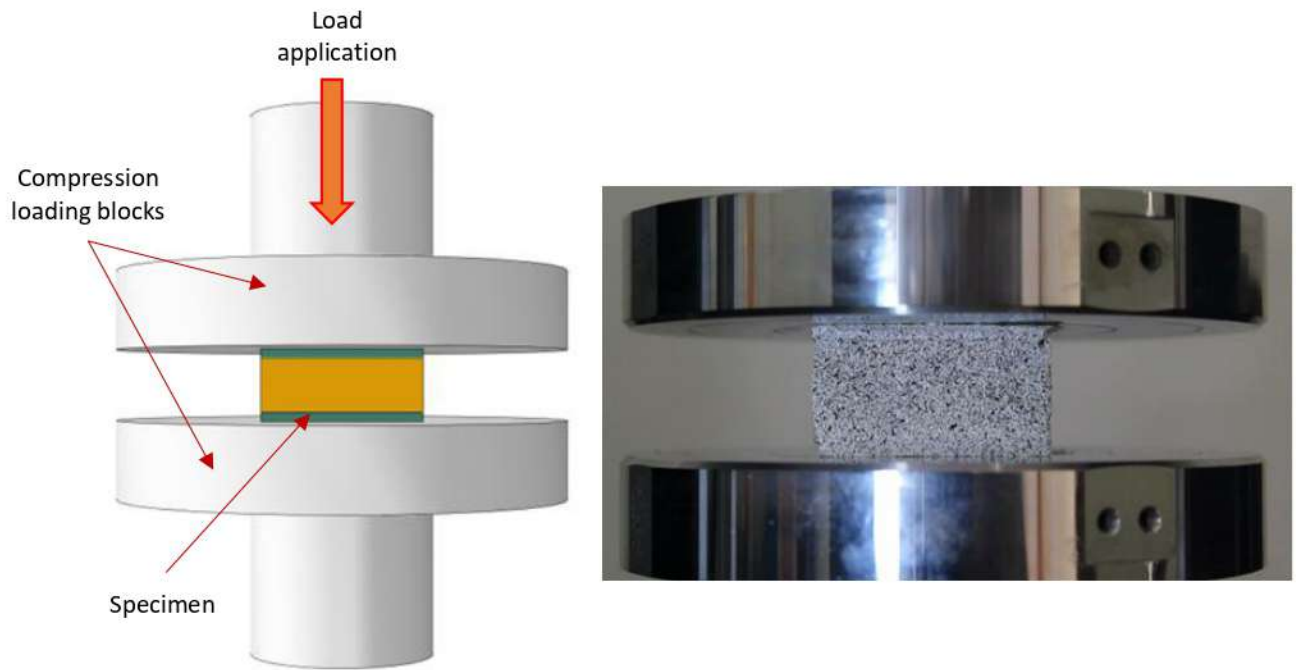


**Figure 2. 17:** Sandwich compressive setup for flatwise compression.

### 2.5.3.3 Shear test

A shear test was conducted on sandwich structure specimens to evaluate their shear modulus and strength, in accordance with the standards ASTM C273-00 [131]. This standard method is designed for assessing the shear properties of sandwich structure. The specimens, which were prepared according to dimensional requirements stipulated in the standard (see Table 2.3), were glued with the loading plates using the same adhesive used in assembling the sandwich which is epoxy resin. The load was applied in a uniaxial tensile direction, parallel to the plane of the sandwich panel faces, with a rate of 0.5 mm/min. Displacement and load data were recorded throughout the test to determine shear stress-strain characteristics. Calculations were then performed to extract the shear modulus and ultimate shear strength. **Fig 2.18** describes the shear test setup.

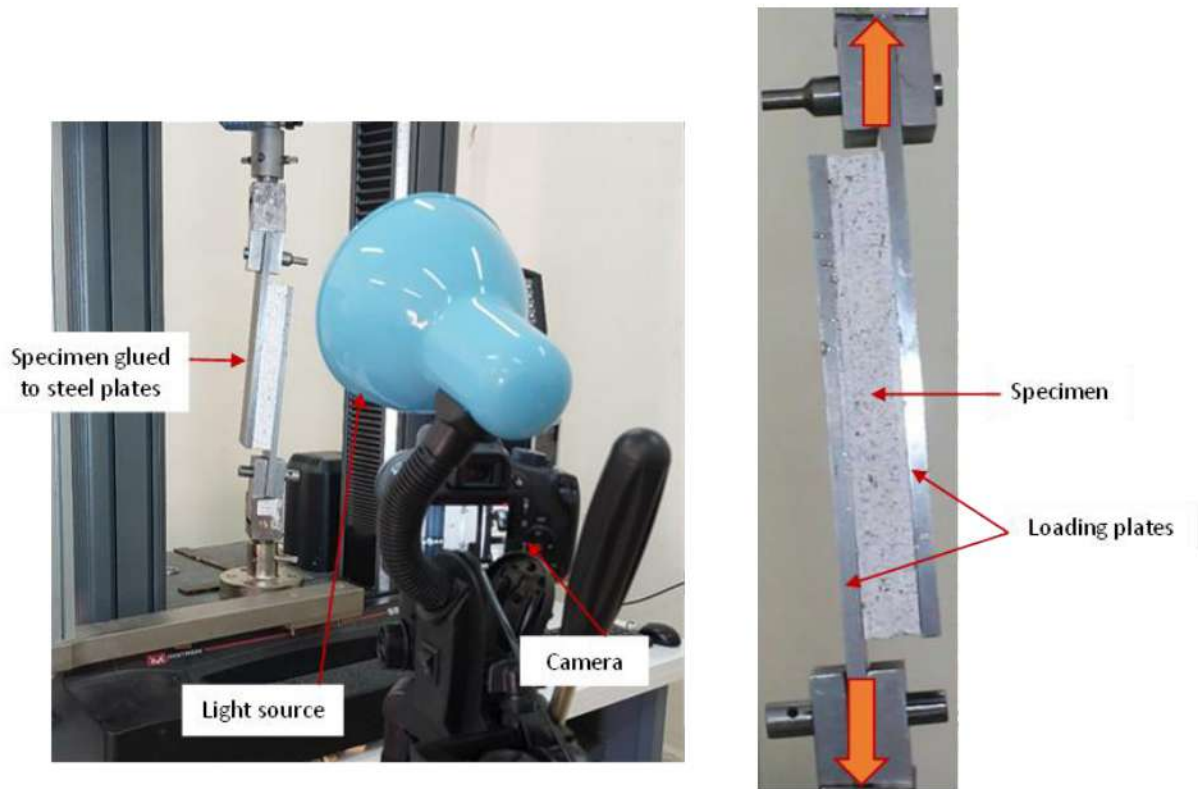


*Figure 2. 18: Shear test setup.*

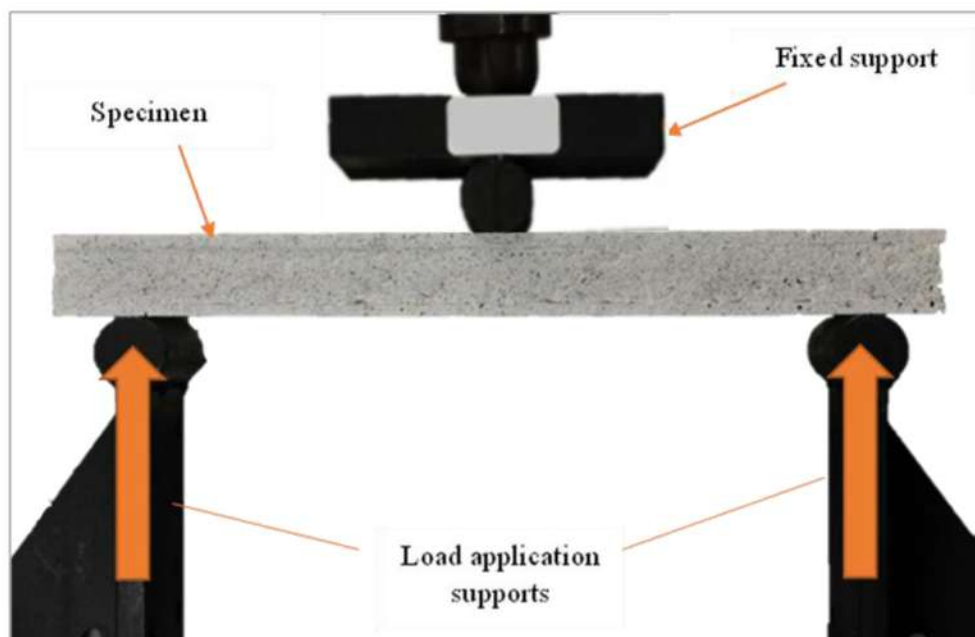
#### 2.5.3.4 Flexural test

To evaluate the flexural stiffness and fatigue behavior of sandwich structure, a static and cyclic loadings were applied on the specimens. The test was performed in three-point bending as shown in *Fig 2.19*. The samples were positioned on two supports with a length  $L$  of 250 mm. The dimensions of the samples are described in *Table 2.3*. The load was applied by the lower supports using TRI-SCAN 100 universal machine. The speed rate of the crosshead was 0.5 mm/min. Load and displacement were recorded throughout to generate load-deflection curves for calculating flexural properties. The static flexure test was designed to assess the ultimate bending load, strength and stiffness of the sandwich structure. For the cyclic flexure test, the specimens were subjected to repeated loading and unloading cycles to simulate fatigue conditions. Approximately 13%, 22%, 37%, and 95% of the ultimate load, as determined from the static test, were applied as four distinct load cycles, which can also be represented relative to the average first peak load. Table 2.3 resumes the dimensions of the sandwich structure.



**Table 2. 3** Dimensions of sandwich structure samples.

Dimensions		w: width (mm)	L: length (mm)	$t_t$ : Total thickness (mm)	$t_c$ : Core thickness (mm)	$t_s$ : Skin thickness (mm)
Edgewise compression test	<b>S-60</b>	60	60	29±1.12	21.8±1.08	3.8±0.15
	<b>S-200</b>	60	200	27.83±3	20.51±3	3.62±0.15
Flatwise compression test		50	50	28.62±2.3	21.3±2.1	3.67±0.35
Shear test		100	200	28.29±1.0	20±0.5	4.3±0.77
Flexural test		100	300	28.61±0.27	20±0.5	3.88±0.86

**Figure 2. 19:** Flexure test fixture

## 2.6 Scanning electron microscopy

The purpose of this study was to understand the failure mode and assess the efficiency of the fiber-matrix and skin-core bonding in samples. To achieve this, a microscopic examination was conducted using the Scanning Electron Microscopy technique at the Scientific and Technical Research Center in Physical-Chemical Analysis located in Biskra, Algeria. Samples were cut from GFRP plates and sandwich structures.

## 2.7 Conclusion

This chapter detailed the materials and methods used for the fabrication and characterization of GFRP plates and sandwich structures with various core materials. The fabrication process, including the production of GFRP skins was systematically outlined. Additionally, the



manufacturing of sandwich structures with different core configurations was described in detail. Experimental characterization of the sandwich structures and their components, including tests conducted according to ASTM standards, was also presented.

# **Results and discussion**

***CHAPTER 03***  
**CHARACTERIZATION  
OF THE CONSTITUENTS  
OF SANDWICH  
STRUCTURES**

## CHAPTER 03. CHARACTERIZATION OF THE CONSTITUENTS OF SANDWICH STRUCTURES

---

### 3.1 Introduction

This chapter presents a detailed analysis of the results obtained from the experimental characterization of the individual components of the sandwich structures, including the core materials and face sheets. The matrix material used for the skins, along with GFRP skins, were thoroughly evaluated for their tensile, compressive, and flexural performance, highlighting their strength, stiffness, and failure mechanisms. Similarly, the core materials PU and PS foams were analyzed for their mechanical properties, including compressive strength, compressive modulus, and their ability to sustain mechanical loads under various conditions. These evaluations were conducted using standardized test methods to ensure reliability and consistency. The results presented in this chapter provide essential insights into the individual contributions of the skin and core materials to the overall mechanical performance of the sandwich structures. This characterization forms the basis for understanding how these components interact and perform when integrated into a complete sandwich structure.

### 3.2 UP resin

*Fig 3.1* demonstrates the stress-strain curves of the experimental test obtained from machine's control software. One can see that the curves exhibit a similar performance; a linear part corresponding to an elastic behavior, followed by a nonlinear part that started with a bend which could be related to the first crack than an increase until final failure. *Fig 3.2* shows full DIC engineering; measured displacement on the lateral area of the tested sample and their corresponding computed strains. The images were taken just before the specimen totally breaks. The maps of vertical displacement shows that the high value in blue is in the top where the load is applied, it is remarked that it is so accurate to the one acquired by the experimental machine (2.2 mm). The strain field maps indicate the region of the failure in the specimen. The high strain concentration in the longitudinal strain  $\epsilon_y$  designates where the fracture is occurring. To assess the Poisson's ratio, the longitudinal and transverse strains of the UP resin were measured using virtual extensometers. The Ncorr-post MATLAB program, a specialized post-processing tool, was employed to process, visualize, and export the data generated by the Ncorr software [132,133]. To calculate the strain three virtual extensometers were marked by tracing two points (1a-1b, 2a-2b, 3a-3b). *Fig 3.3* illustrates the position for each one for both transverse and



longitudinal strain. For an isotropic material, the Poisson's ratio is the gradient of the elastic linear region of transverse strain- longitudinal strain curve that corresponds to the elastic linear part of stress-strain curve [134]. It is determined as the negative ratio of transverse strain  $\varepsilon_t$  ( $\varepsilon_x$ ) to longitudinal strain  $\varepsilon_l$  ( $\varepsilon_y$ ):

$$\nu = -\varepsilon_t / \varepsilon_l \quad (3.1)$$

**Fig 3.4** demonstrates transverse strain-longitudinal strain to determine the Poisson's ratio  $\nu_{12}$  of UP resin. As illustrated in the stress-strain curves (**Fig 3.1**), the elastic phase could be defined until the longitudinal strain reaches approximately 0.0016 (OA). The results achieved after exporting the extensometers data expose that the Poisson's ratio of UP resin can be estimated by 0.46 which is near to values of UP used by Biswas et al. (0.44) [135].

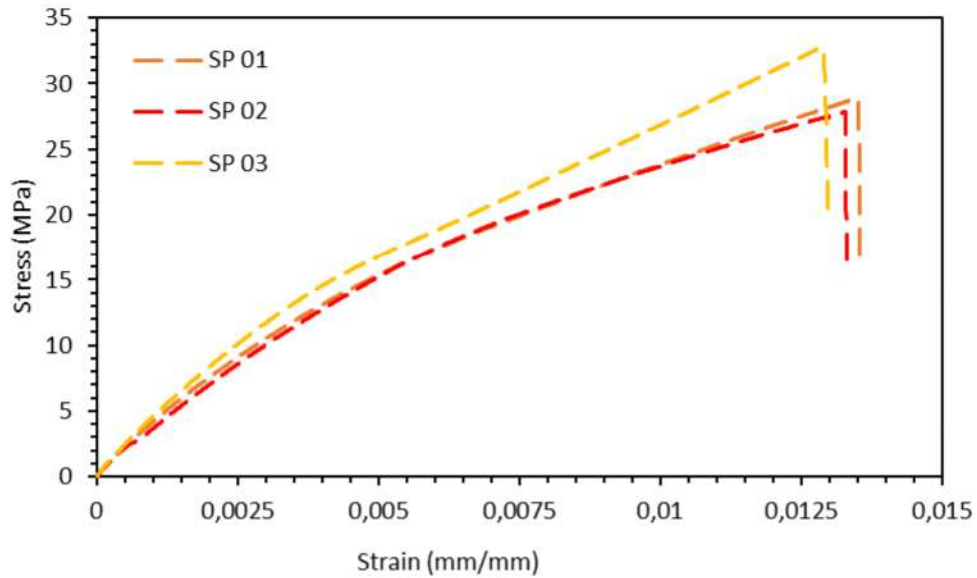


**Figure 3. 1:** Stress strain curves of tensile test of UP resin [136]

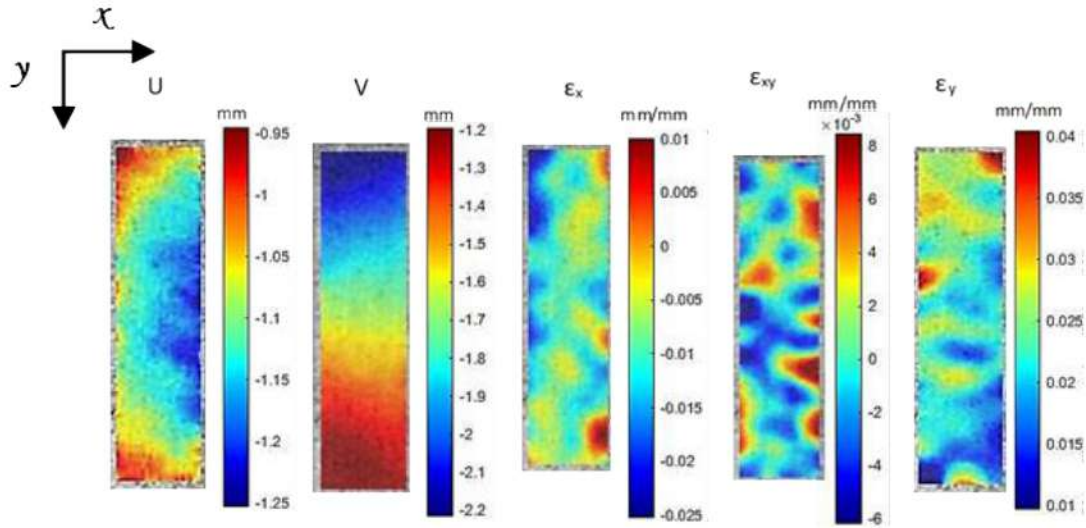


*Figure 3. 2: DIC engineering displacement and strain fields for tensile test of the specimens. [136]*

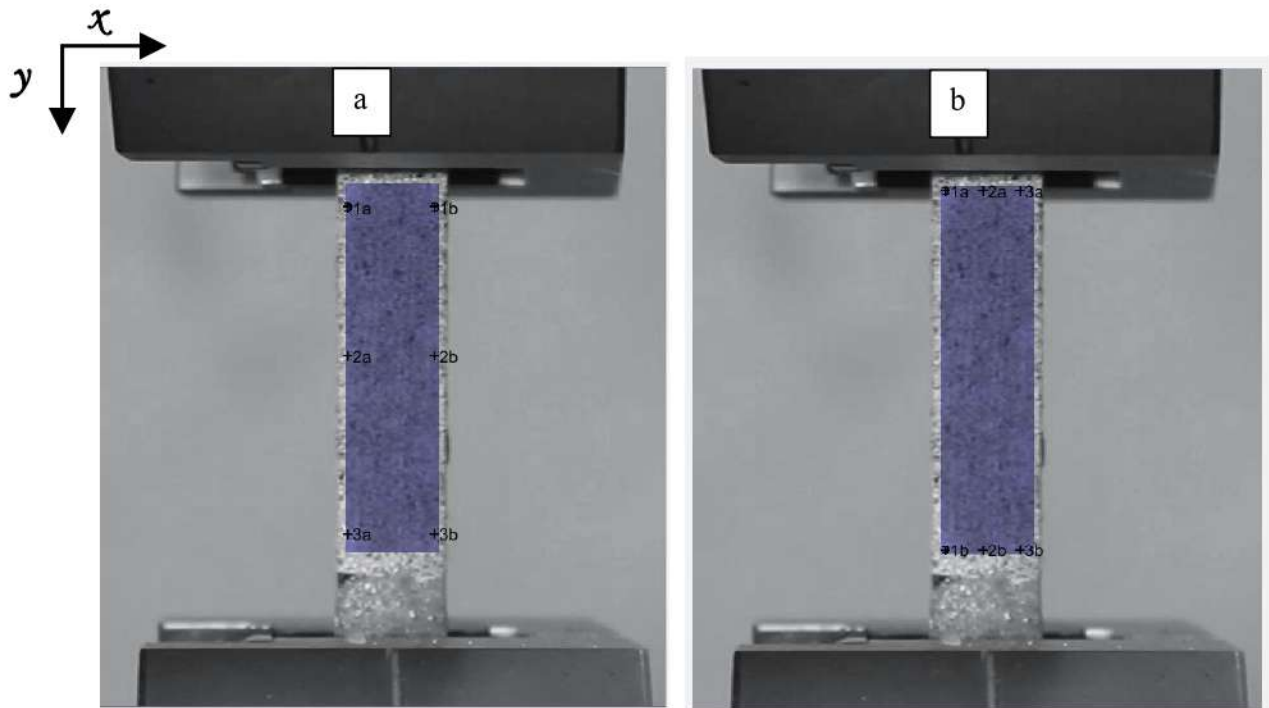


*Figure 3. 3: virtual extensometers to obtain: a) Transverse strain  $\epsilon_t$ , b) Longitudinal strain  $\epsilon_l$ . [136]*

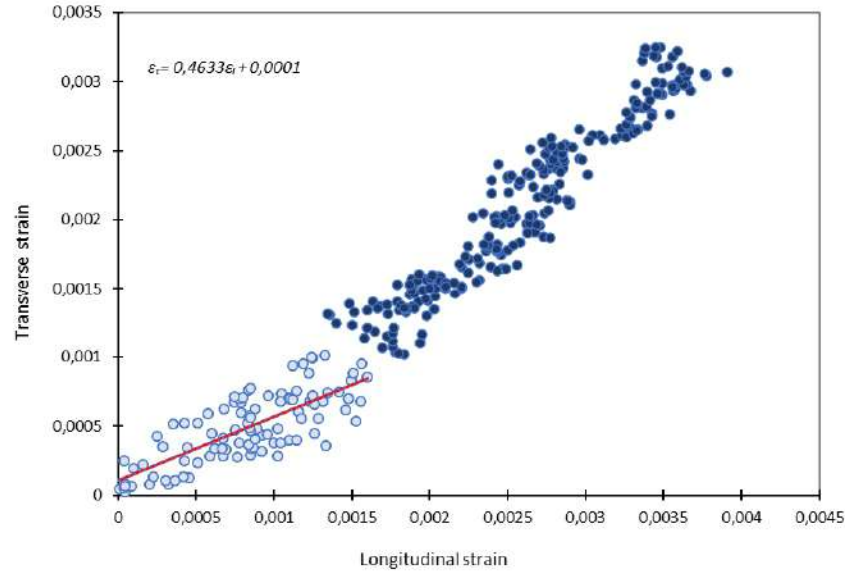


**Figure 3. 4:** Transverse strain-longitudinal strain curves for evaluating Poisson  $\nu_{12}$ [136].

### 3.3 GFRP skin characterization

#### 3.3.1 Tensile test

**Fig 3.5a** shows the stress-strain curves of the tensile test for GFRP skin. It demonstrates that the curves behave identically and approximately overlay one another, which confirms the repeatability and reliability of the GFRP skin behavior under tension load. It is observed that this behavior is divided into three parts as demonstrated; firstly, the behavior is mainly linear to a point where the elastic stress is about 12.57 % of the ultimate tensile stress then the curves lose their linearity and the damage starts, it is defined by the elastic modulus. At the end of the elastic part, the curves exhibit a bend that could be related to prior fiber damage caused by fragile bonding between fiber and matrix. The last one is when tensile stress increases nonlinearly with longitudinal strain until final damage occurs. As illustrated in **Fig 3.5b** the failure positions of the specimens after testing, were almost close to the center. **Fig 3.6** demonstrates SEM image of fractured zone from the specimen under tensile test. One can see an irregular distribution of glass fibers, a debonding of fiber-matrix, fiber breaking and pull out. The maps in **Fig 3.7** represent the in-plane strain fields of the GFRP skin under tensile loading of Sp 03. The DIC images were taken just before final failure. The chromatic map displays the maximal value of strain  $\epsilon_y$  in red 0.03, which confirming the experimental results with high accuracy. The concentration of longitudinal strain illustrates the position of the fracture in the specimen. The results obtained from the tensile test are summarized in **Table 3.1**. All samples



have approximately the same strength, and the average value is 151.12 MPa with corresponding strain of 2.7%.

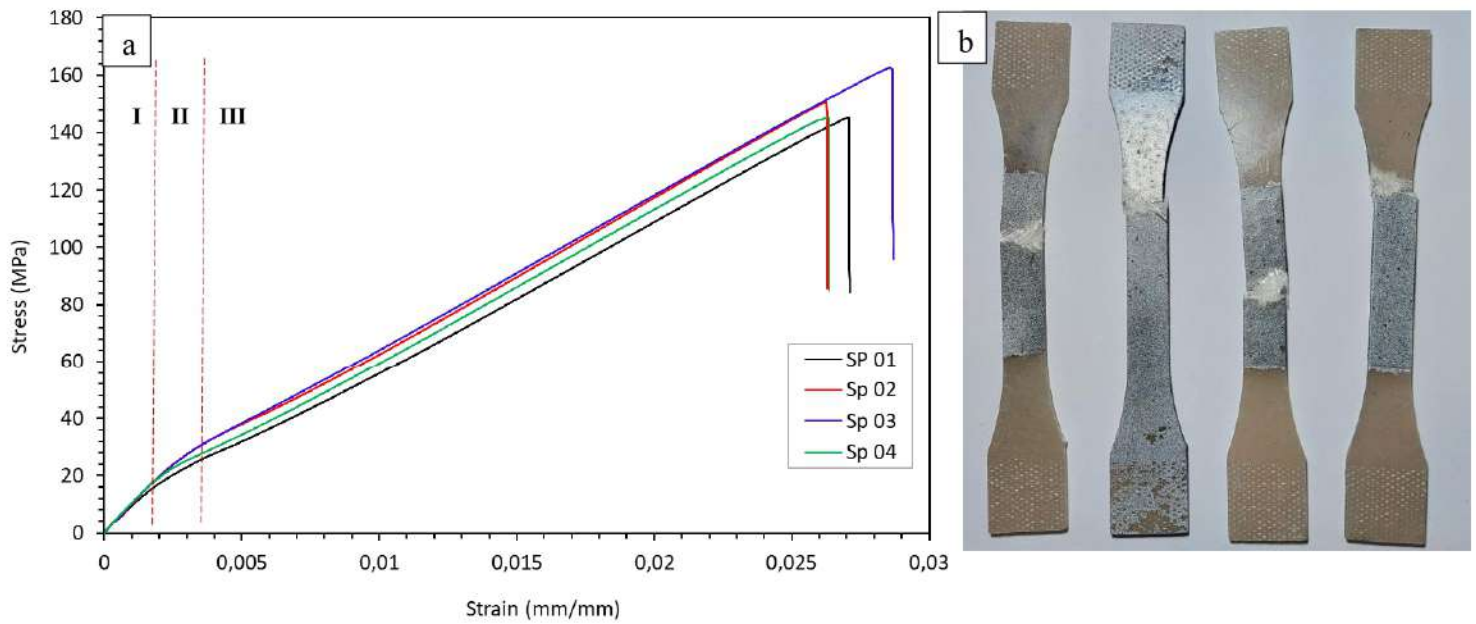


**Figure 3. 5:** a) Stress-strain curves for tensile test of GFRP skin. b) Specimens after tensile test [137]

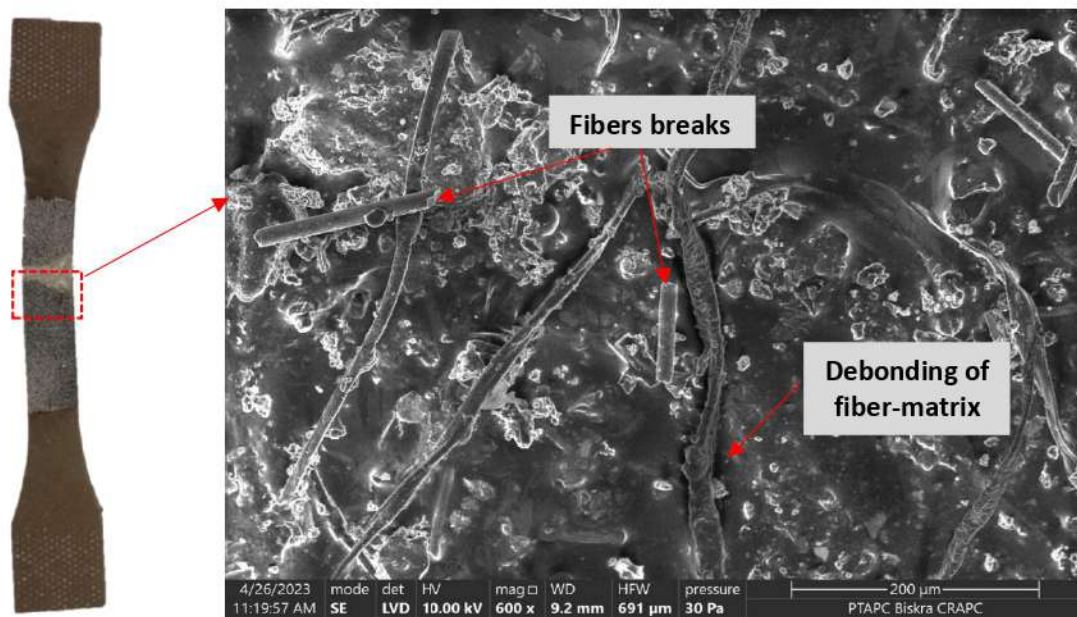


**Figure 3. 6:** SEM images of fracture surface of GFRP skin under tensile failure [137].



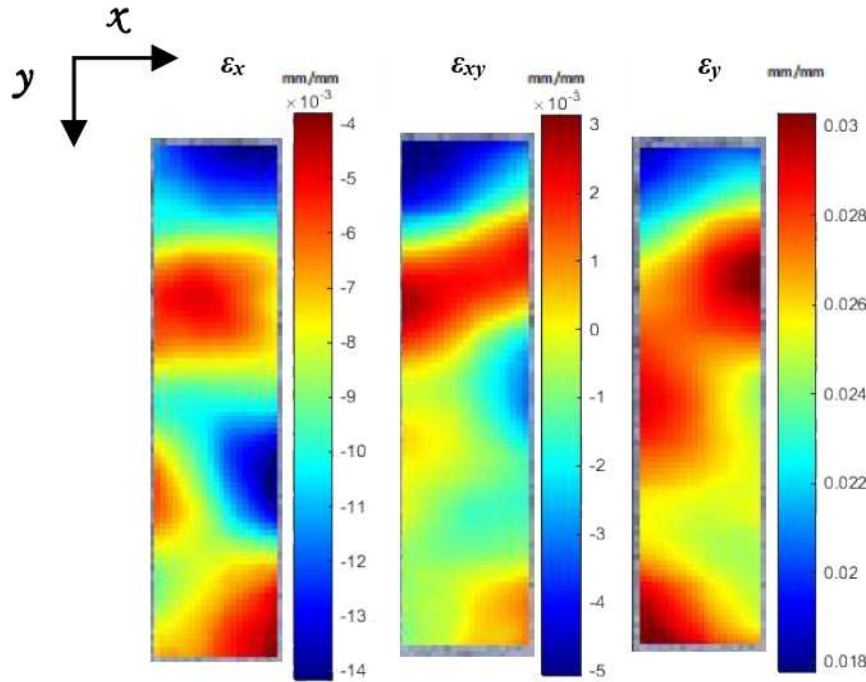


**Figure 3. 7:** DIC engineering strain fields for tensile test of GFRP skin [137].

**Table 3. 1** Mechanical parameters obtained through tensile test of GFRP skin.

	$P_{\max}$ (N)	Displacement (mm)	Ultimate tensile stress (MPa)	Tensile strain (mm/mm)	$E_{\text{st}}$ (MPa)
Sp 01	7331.99	4.47	145.36	0.027	9656.84
Sp 02	7645.72	4.34	150.80	0.026	9899.19
Sp 03	8172.43	4.73	162.86	0.029	9806.83
Sp 04	7430.43	4.35	145.44	0.026	9406.89
Average	7645.14	4.47	151.12	0.027	9692.44
SD	8.23	0.18	8.23	0.001	214.97

### 3.3.2 Compression test

**Fig 3.8a** presents the stress-strain curves of the compressive test for GFRP skin. Just like the tensile test, it is illustrated that the curves exhibit an identical behavior. Three distinct phases are noted. Initially, the behavior remains predominantly linear, reaching a point where the curves deviate from linearity and damage commences; this phase is primarily characterized by the elastic modulus. The elastic stress is estimated by 2.17% of the ultimate compressive stress. At the end of the elastic phase, the curves exhibit a noticeable bend, which may be attributed to previous fiber damage resulting from weak bonding between the fibers and the matrix. The final

phase involves a nonlinear increase in compressive stress with longitudinal strain until eventual failure or damage is observed. As it is shown in **Fig 3.8b** and **Fig 3.9** the failure modes that occur in the specimens is localized at the center. It was evident that the observed failure involved a combination of longitudinal splitting, interlaminar cracking, fiber breakage, and the formation of kink bands, specifically manifested as fiber micro-buckling. Kim et al. [138] had detected comparable failure mode of GFRP composites subjected to compression. **Fig 3.10** illustrates the region of interest studied in DIC and full fields strain maps of **Sp 03**. The DIC images were taken just before final failure. The chromatic maps display the highest absolute values of strain  $\epsilon_y$  0.031 at the top where the load is applied. On the other hand, it can be seen that the values obtained through DIC are close to the those obtained experimentally (see **Table 3.2**). The maximum values of  $\epsilon_x$  appeared in the middle of the specimen is 0.02, demonstrating the region of the local buckling happened to the sample. The results obtained from the compressive tests are listed in **Table 3.2**. The samples have an average strength of 226.70 MPa and 3.4 % strain.

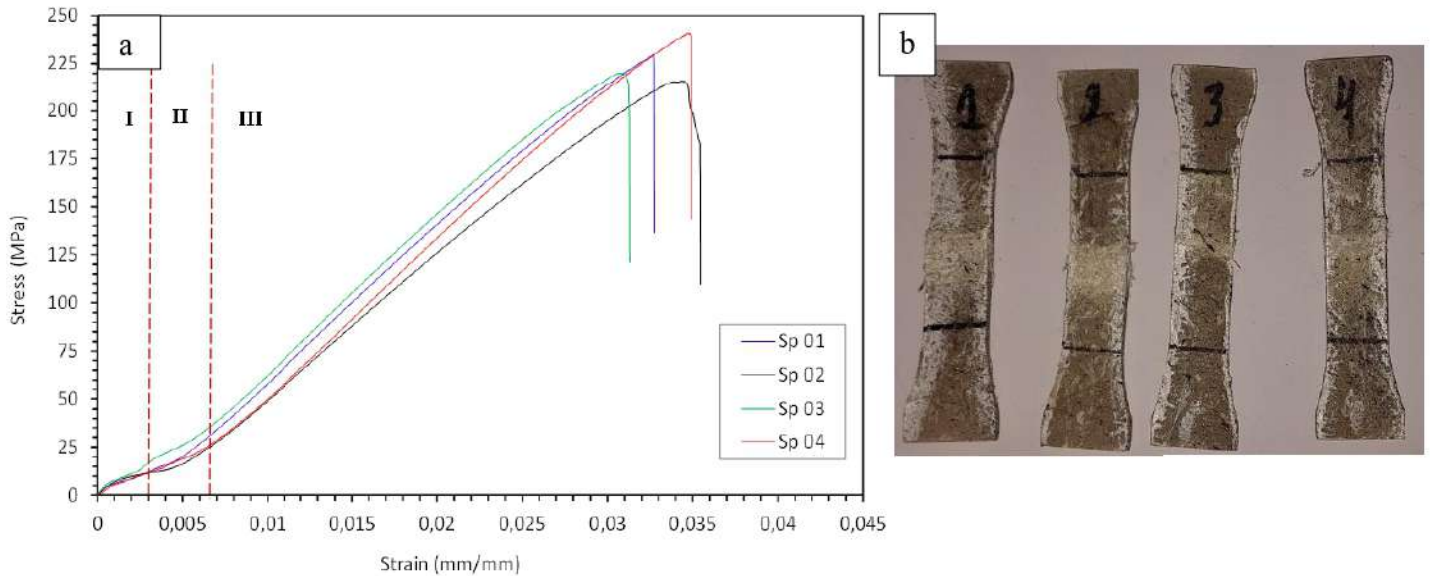


**Figure 3. 8: a) Stress-strain curves for compression test of GFRP skin. b) Specimens after compression test.**

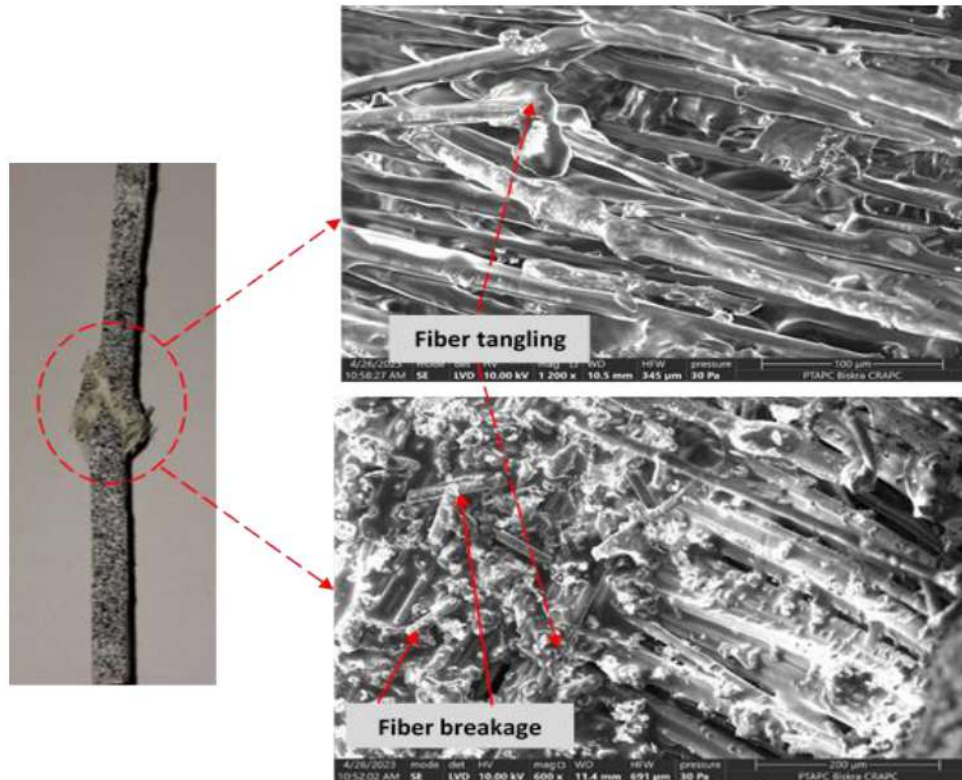


*Figure 3. 9: SEM images of fracture surface of GFRP skin under compressive failure.*

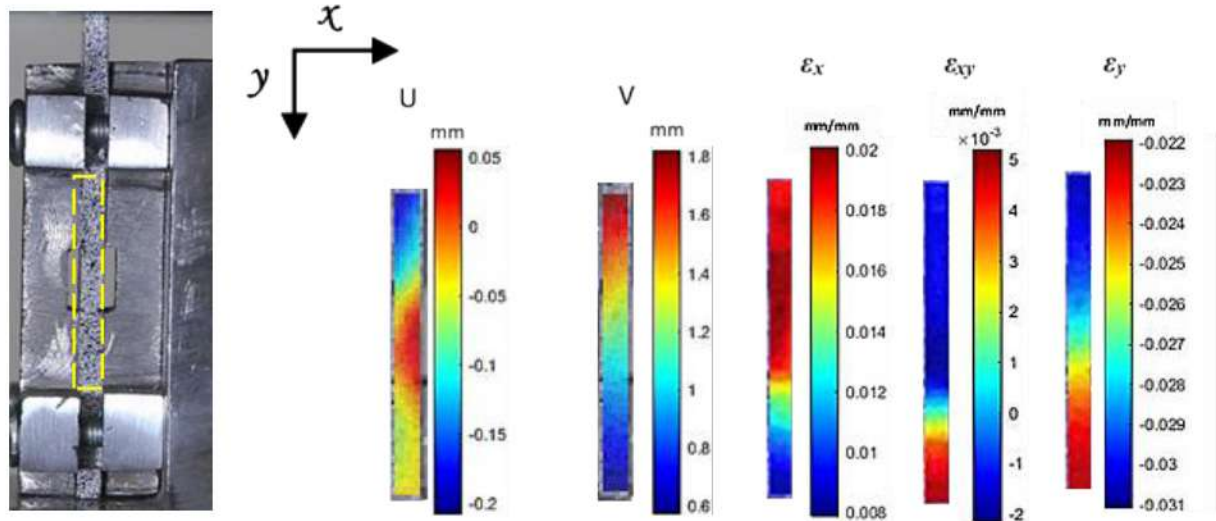


*Figure 3. 10: Region of interest studied in DIC and DIC engineering fields for compression test of GFRP skin.*



**Table 3. 2** Mechanical parameters obtained through compressive test of GFRP skin.

	$P_{\max}$ (N)	Displacement (mm)	Ultimate compressive stress (MPa)	Compressive strain (mm/mm)	$E_{sc}$ (MPa)
Sp 01	12575.44	2.60	229.74	0.032	9524.71
Sp 02	11680.25	2.82	215.89	0.035	8643.35
Sp 03	11562.19	2.49	220.44	0.031	9285.39
Sp 04	13055.18	2.77	240.74	0.035	9701.55
Average	12218.27	2.67	226.70	0.034	9288.75
SD	718.31	0.15	10.99	0.0019	462.83

### 3.3.3 Flexural test

#### 3.3.3.1 Three-point bending

The experimental results of three-point flexural loading are depicted in **Fig 3.11**. The specimen after failure shown in **Fig 3.11a** exposed the layers delamination and fiber breakage. The flexural loading-displacement curves in **Fig 3.11b** show the behavior of three GFRP specimens. Initially, all curves exhibit a linear relationship between load and displacement, indicating elastic behavior. The slope of this linear region represents the stiffness of the sample. As the load increases, a deviation from linearity is observed, which can be caused by an internal damage such as matrix cracking, fiber debonding, or fiber fracture. Eventually, the curves reach a peak load followed by a sharp drop, indicating final failure. The DIC analysis presented in **Fig 3.12** provides a detailed understanding of the deformation and strain behavior of the GFRP skin under three-point bending. The strains concentration in loading point reveals the localized stress and damage initiation. In this region the distribution distinct tensile and compressive zones resulting from bending. The bottom surface experiences tensile strain as it stretches, whereas the top surface undergoes compressive strain due to contraction. The vertical displacement values measured using DIC were consistent with the displacement values recorded by the testing machine. This consistency demonstrates a high level of accuracy and agreement between the mechanical testing system and the DIC method. The flexural stress and strain at outer surface of the specimen are calculated using eq 3.2 and 3.3 respectively. The main results from the test are presented in **Table 3.3**. The computed average ultimate flexural strength and the maximum strain are assessed as 219.55 MPa and 4.2% respectively.



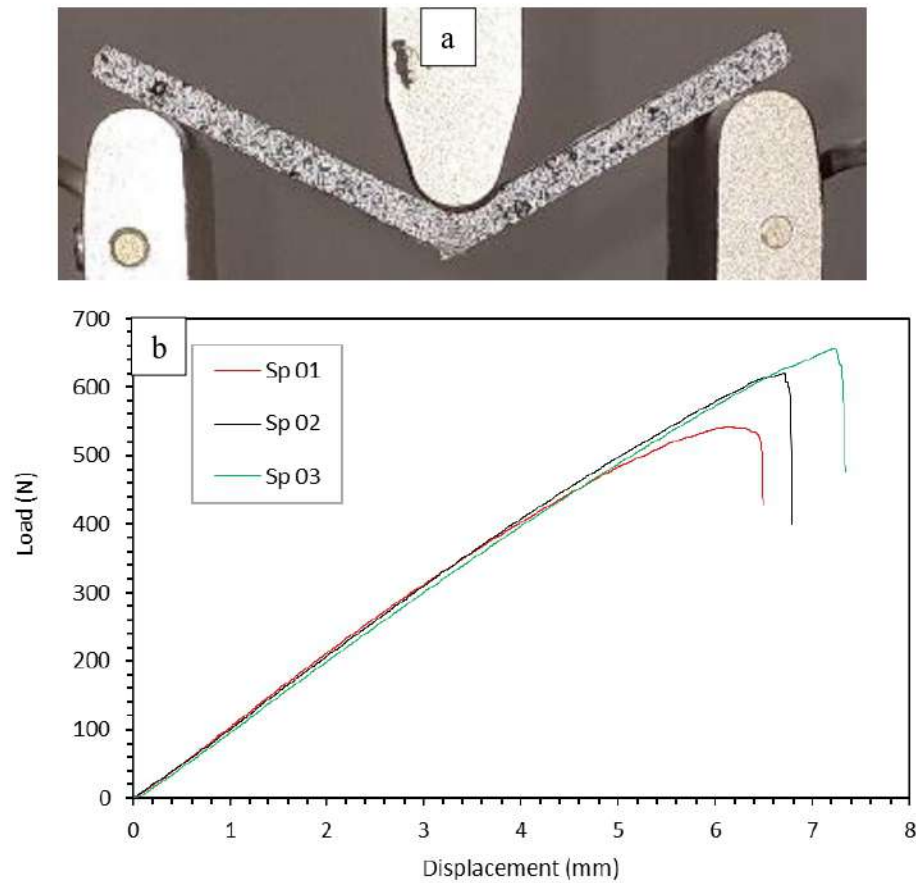


**Figure 3. 11:** Three-point test a) Specimen after test. b) Load-displacement curves.

**Table 3. 3** Results obtained through three-point bending

	Pmax(N)	Deflection (mm)	Flexural stress $\sigma_{sf3}$ (MPa)	Strain max (mm)	Flexural modulus $E_{sf3}$ (MPa)
Sp 01	540.94	6.49	205.95	0.039	6623.2
Sp 02	619.93	6.78	236.02	0.041	6409.4
Sp 03	655.44	7.35	216.68	0.047	5062.3
Average	605.43	6.87	219.55	0.042	6031.63
SD	58.61	0.44	15.24	4.42E-03	846.25

The flexural stress  $\sigma_f$  at the outer surface at mid-span

$$\sigma_{sf3} = \frac{3PL}{2bh^2} \quad (3.2)$$

Where P, L, b and h, are; load, span length, width of the specimen and thickness of the specimen, respectively.

Strain in the outer surface of the specimen as follows

$$\varepsilon_{sf3} = \frac{6\delta h}{L^2} \quad (3.3)$$

Where  $\delta$  is mid-span displacement.

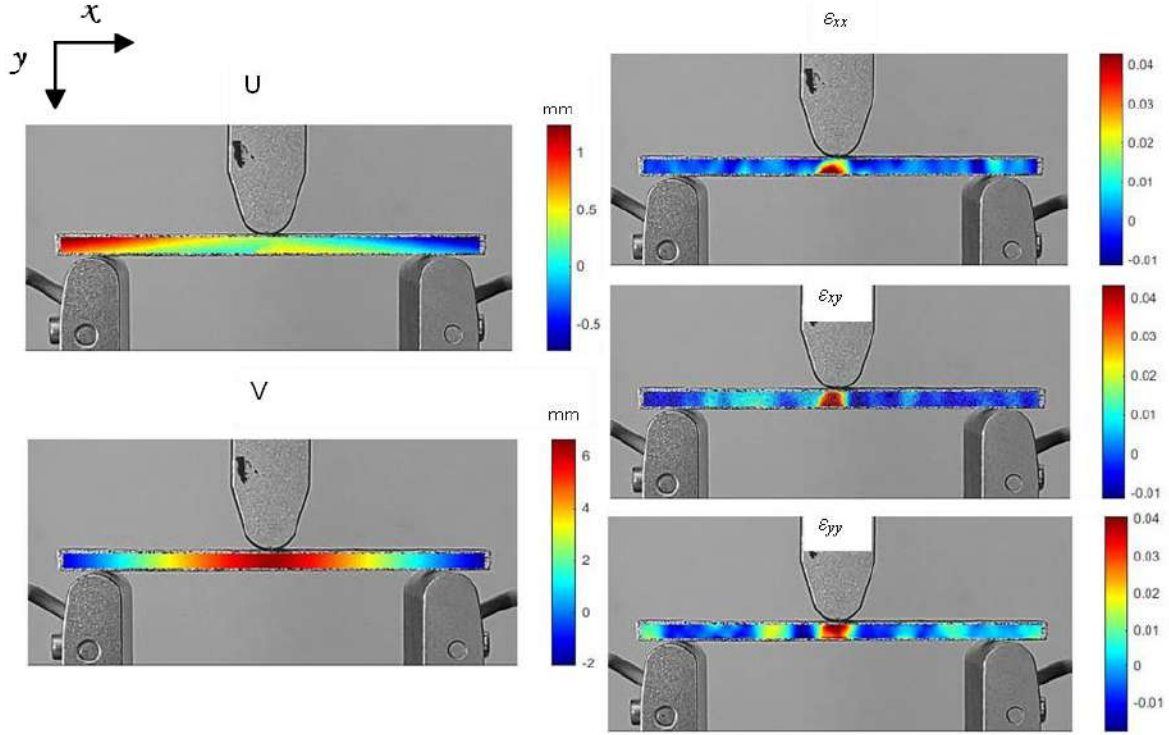


**Figure 3. 12:** DIC engineering for Three-point bending of GFRP skin.

### 3.3.3.2 Four-point bending

**Fig 3.13a** and **3.13b** shows specimens and the load-displacement curves of experimental results from four-point bending test, respectively. The observed failure appears to be a combination of interlaminar shear failure, tensile fiber failure, and matrix cracking. The separation between layers suggests delamination, which typically occurs in the load span region due to high shear stress. The load-displacement curves perform identically demonstrating a consistent mechanical response among the tested specimens. The initial linear region represents the elastic response. As the load increases, the curve reaches the peak load, which signifies the ultimate flexural strength of the material. The peak load indicates the ultimate flexural strength. The post-peak region shows a drop, suggesting brittle failure. **Fig 3.14** illustrates the SEM analysis of GFRP specimen after the test. The analysis confirms that the specimens failed through a combination of debonding of fiber-matrix and fiber pull-out. The DIC engineering fields are presented in **Fig 3.15**. The vertical displacement (V) values obtained through DIC were in

agreement with those recorded by the testing machine. The strain concentration detected at bottom surface in  $\epsilon_y$  field indicates tensile failure, whereas compressive failure is localized at the top surface within the load span region. The main results from the test are presented in Table 3.4. The flexural stress and strain at outer surface are calculated using eq 3.4 and 3.5, respectively. The test results indicate that the GFRP specimen exhibited an average ultimate stress of 263.38 MPa and a maximum strain of 3.5%. **Fig 3.16** displays a comparison of four-point and three-point flexural strength and flexural modulus. As it appears, the flexural strength and flexural modulus of four-point bending test are higher than the ones of three-point bending.

The flexural stress  $\sigma_f$  at the outer surface in the load span region

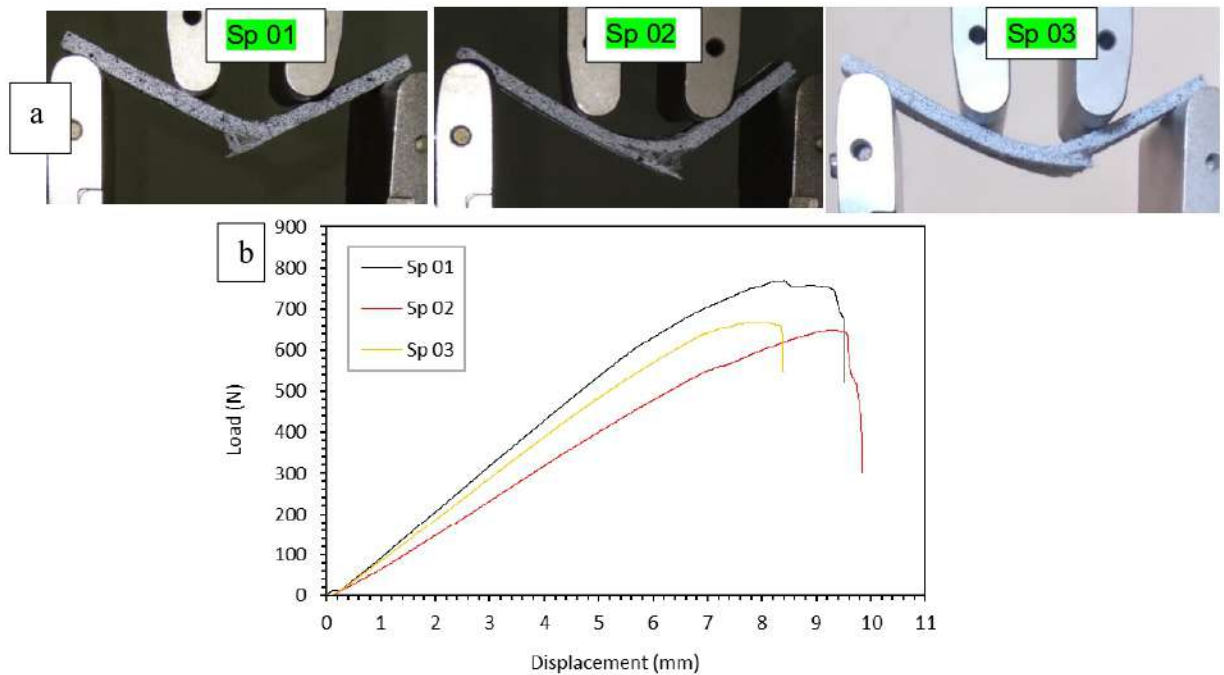
$$\sigma_{sf4} = \frac{PL}{bh^2} \quad (3.4)$$

Where P, L, b and h, are; load, span length, width of the specimen and thickness of the specimen, respectively.

Strain in the outer surface of the specimen as follows

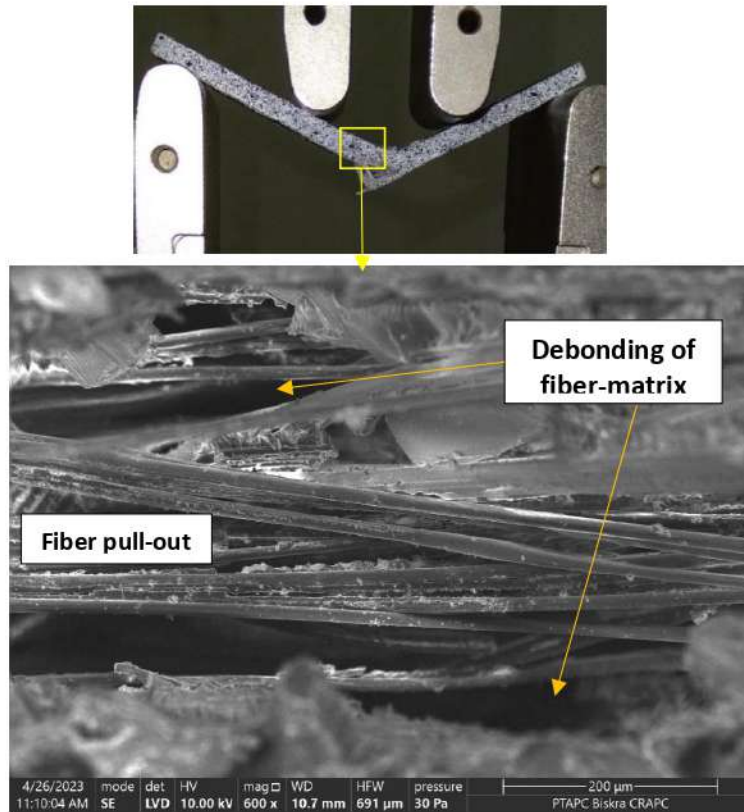
$$\epsilon_{sf4} = \frac{4.7\delta h}{L^2} \quad (3.5)$$

Where  $\delta$  is mid-span displacement.

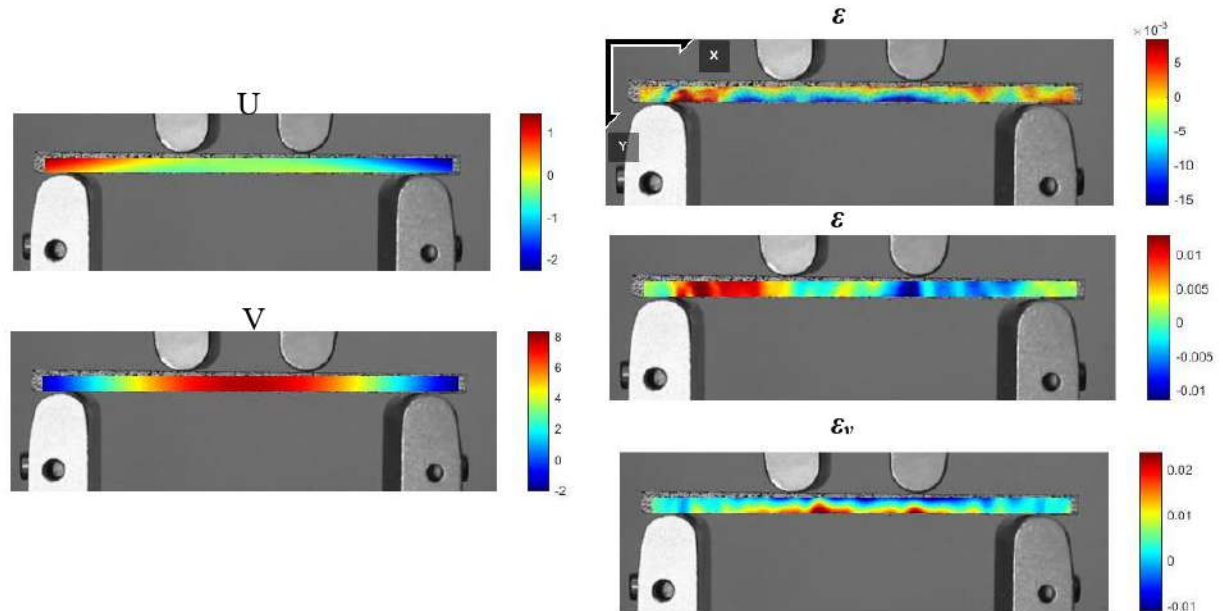


**Figure 3. 13:** a) Specimens after four-points flexural test, b) Load-displacement curves.





*Figure 3. 14: SEM analysis of GFRP specimen after four-point bending.*

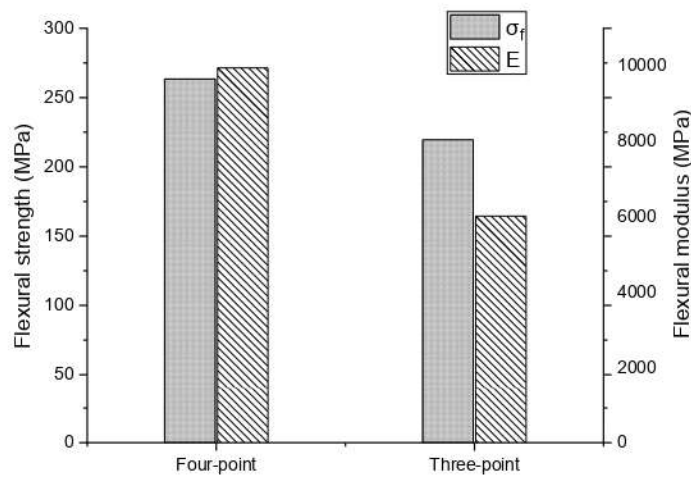


*Figure 3. 15: DIC engineering for Four-point bending of GFRP skin.*



**Table 3. 4** Results obtained through four-point bending

	Pmax(N)	Deflection (mm)	Flexural stress $\sigma_{sf4}$ (MPa)	Strain max (mm)	Flexural modulus $E_{sf4}$ (MPa)
Sp 01	769.51	9.52	274.82	0.036	10379
Sp 02	648.86	9.84	252.89	0.036	8803.8
Sp 03	669.37	8.39	262.49	0.032	10669
Average	695.91	9.25	263.38	0.035	9950.6
SD	64.55	0.76	10.99	2.30E-03	1003.69

**Figure 3. 16:** Comparison of four-point and three-point flexural strength and flexural modulus.

### 3.4 Flatwise compression test of PU and PS foams

The load-displacement curve obtained from the compressive testing of PU foam is presented in **Fig 3.17a**. The curve typically exhibits three distinct regions: the linear elastic region, the plateau region, and the densification region. In the linear elastic region, the load increases proportionally with displacement as the foam deforms elastically. Beyond this point, as displacement continues, the curve enters the plateau region, where the load remains low while displacement continues to increase. Finally, in the densification region, the cell walls are fully compacted, and the load rises sharply with further displacement as the material resists additional compression. **Fig 3.17b** presents the load-displacement curve for PS foam. The curve similarly begins with an initial linear elastic region, followed by a plateau region. However, the plateau region in PS foam is shorter and less prominent compared to that of PU foam. This difference arises from the brittle nature of PS foam, which causes the cell walls to collapse more abruptly under load. Additionally, the densification region in PS foam is observed at lower

displacements compared to PU foam, reflecting its reduced capacity to sustain deformation before full compaction occurs.

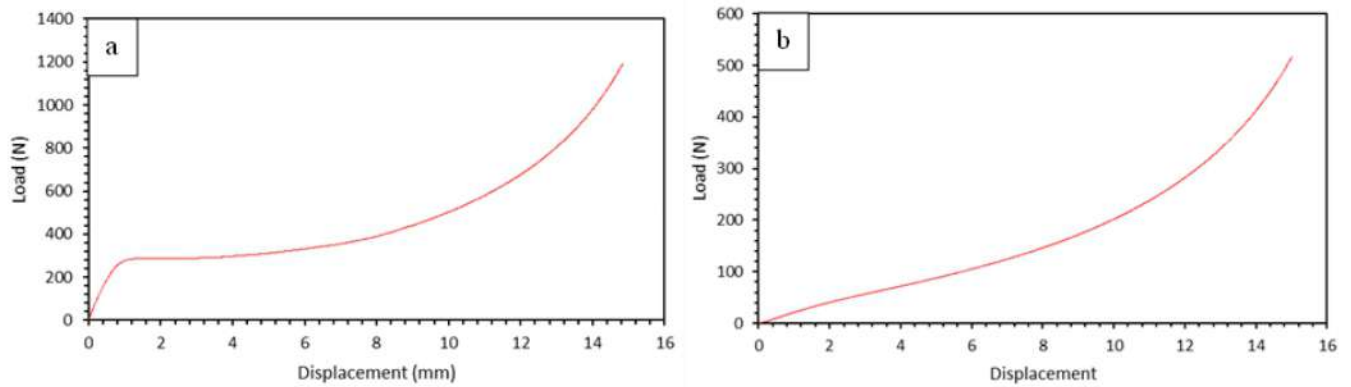


**Figure 3. 17:** Load-displacement curve of flatwise compression test; a) PU foam, b) PS foam

**Table 3. 5** Mechanical properties of PU and PS foams

Properties	PU foam	PS foam
Compressive stress (MPa)	0.48	0.21
Compressive strain (mm/mm)	0.74	0.75
Elastic stress (MPa)	0.10	0.017
Corresponding strain (mm/mm)	0.40	0.11
Compressive Modulus (MPa)	4.19	0.19
Shear modulus (MPa)	1.49	0.09

### 3.5 Conclusion

This chapter discussed the essential characterization and properties obtained throughout mechanical and SEM analysis of the components of the sandwich structures. GFRP skin was subjected to tensile, compression, three-point and four-point bending to acquire their mechanical characteristics. The morphology of the specimens after tests were presented. The mechanical characteristics of PU and PS were studied through flatwise compression. The findings from these characterizations form the foundation for understanding the role of each component in the overall behavior and performance of the sandwich structures under various loading.

***CHAPTER 04***  
***MECHANICAL***  
***BEHAVIOR OF***  
***SPU AND SPS***

## CHAPTER 04. MECHANICAL BEHAVIOR OF SPU AND SPS

---

### 4.1 Introduction

This chapter presents a comprehensive analysis of the results obtained from the mechanical characterization of sandwich structures with PU (SPU) and PS foam (SPS) cores. These results are based on a series of tests conducted under various loading conditions, including edgewise compression, flatwise compression, shear, as well as static and cyclic flexural loading. Each test was designed to evaluate specific mechanical properties such as strength, stiffness, and failure modes under different stress conditions.

### 4.2 Edgewise compression test of SPU and SPS

*Fig 4.1* shows the failure modes of SPU and SPS samples under edgewise compression loading for **S-60**. The specimens experienced the same behavior until final failure; localized buckling in the mid-section of the specimens followed by skin cracking on both sides and progressed throughout the width of the specimen and a small skin-core debonding on one side. SP 02 of SPS experienced skin shear where the localized buckling has occurred. It is observable that Sp 03 and Sp 04 of SPU and SPS samples respectively behaved differently from the other specimens, this difference can be caused by a lack of adhesion between skin and core. An abrupt failure caused by skin buckling succeeded by skin-core debonding on both sides for those specimens with a shear sliding damage of the skin on the left side. *Fig 4.2* depicts the load-displacement curves obtained from the test for S-60. The curves of Sp 03 for both foam cores demonstrate a decent linearity to ultimate load then the load decreased gradually to total failure. While the curves of the other three specimens exhibited similar pattern and performed an initial phase of linear increase of the applied load followed by a non-linear phase until it reaches the ultimate load, then the load decreased gradually to final failure. Summarized results are listed in Table 4.1, for S-60 the average values of the test were calculated without including Sp 03. According to ASTM C-364M the ultimate flatwise compression strength was calculated using the *eq. (4.1)*

$$\sigma_{EC} = \frac{P_{max}}{2.w.t_s} \quad (4.1)$$

where  $\sigma_{EC}$  the ultimate edgewise compressive strength (MPa).  $P_{max}$  is the ultimate force prior to failure (N),  $w$  width of specimen (mm) and  $t_s$  thickness of a single face sheet (mm).



The average ultimate load for the three SPU specimens is approximately 37860.76 N, which is nearly twice that of SP 03. In comparison, the average ultimate load for SPS is 34631.94 N. DIC engineering displacement and strain fields for edgewise compression test for both SPU and SPS are shown in **Fig 4.3** the images were taken before the correlation is lost. The collapse modes observed during the test are further elucidated by analyzing horizontal displacement (U). The maximum horizontal displacement (U) is concentrated in the region where the specimen first buckled and sustained damage, whereas the maximum vertical displacement (V) occurs at the top of the specimen, aligning with the point of load application. **Fig 4.4** illustrates the collapse modes of S-200 for SPU and SPS, a significant difference in failures mechanisms is noticed. For S-200 different behavior was detected, the specimens collapsed in the global buckling mode or as it known Euler buckling. A densification of the foam is noticed during the test for both S-60 and S-200. **Fig 4.5** represents the load-displacement curves obtained from the test for S-200. The curves exhibit a small linear pattern succeeded by a non-linear one until the ultimate load reached its maximum. Followed by softening phase of post-buckling. The divergence of failure modes of **S-60** and **S-200** samples under edgewise compression load signify that the lengths of samples have a crucial impact. When the length is higher than the width the Euler buckling become the dominant failure mode and the load capacity of the samples decreases. The ultimate load had reduced from 37860.76 N to 6487.96 N for SPU and from 34631.94 to 4972.003 for SPS with the increasing of the length of specimens. DIC engineering displacement and strain fields for edgewise compression test for **S-200** are shown in **Fig 4.6**. The displacement field along the horizontal direction (U) provides clearer insights into the collapse modes of the specimens. The maximum horizontal displacement (U) is observed in the region where the initial buckling and damage occurred. In contrast, the maximum vertical displacement (V) is located at the top surface where the load was applied. As results; different failure mechanisms were distinguished for sandwich structures under edgewise compression load. With length equal to the width the samples experienced skin-core debonding, shear sliding damage of the skin, and localized buckling in the mid-section of the specimens followed by skin cracking on both sides and progressed throughout the width of the samples. While when length is much greater than the width the global buckling mode is the dominant collapse mode.

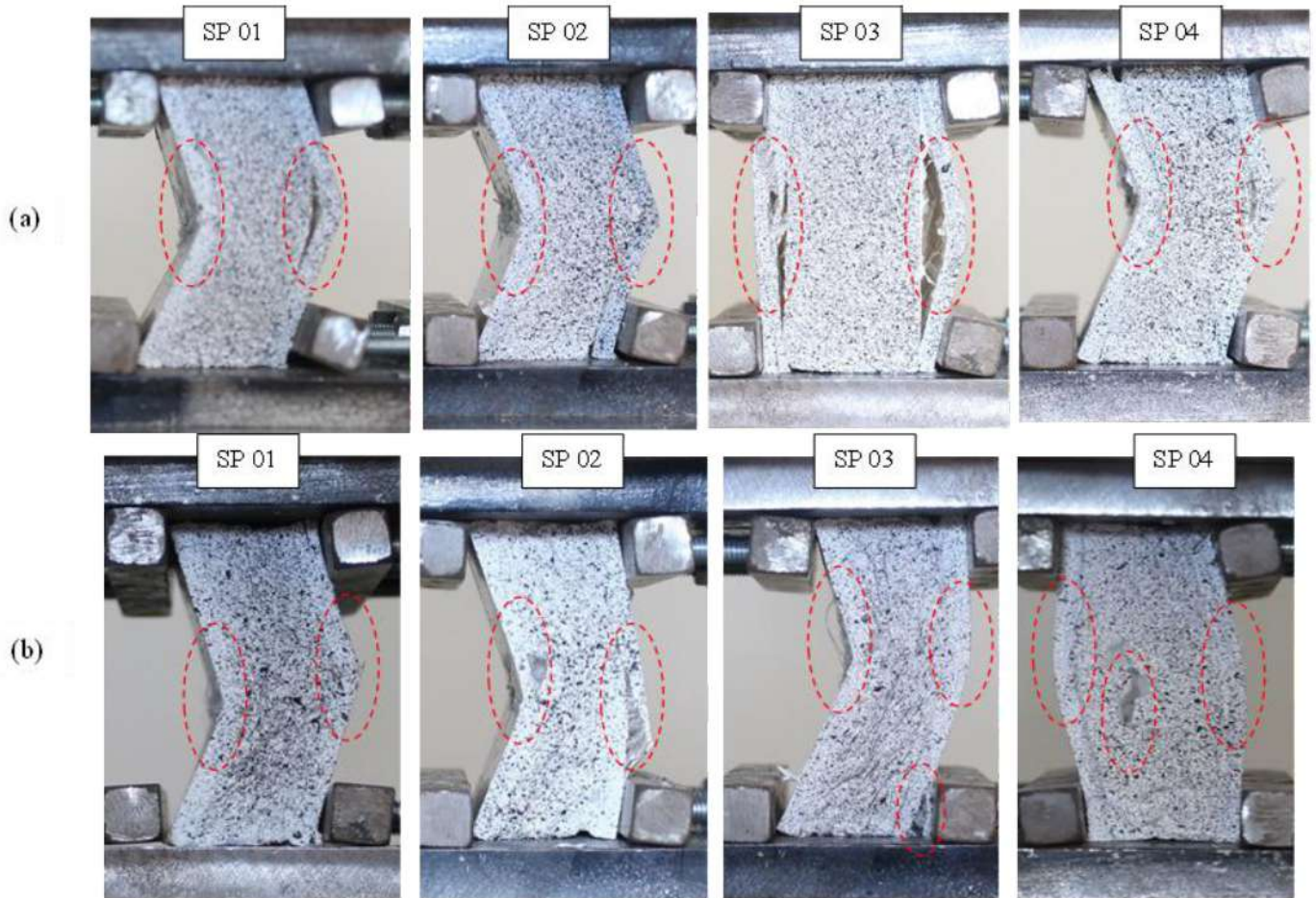


**Figure 4. 1:** Specimens after edgewise compression test for S-60: a) SPU, b) SPS.

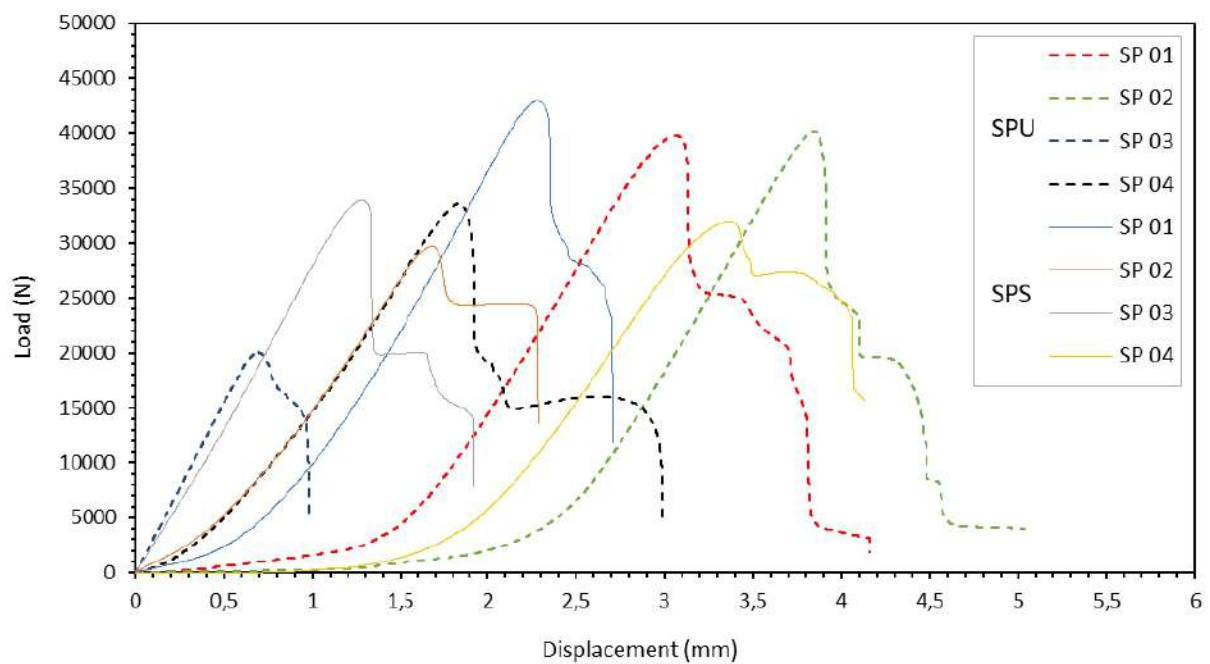


**Figure 4. 2:** Edgewise compression load-displacement curves for SPU and SPS; S-60.

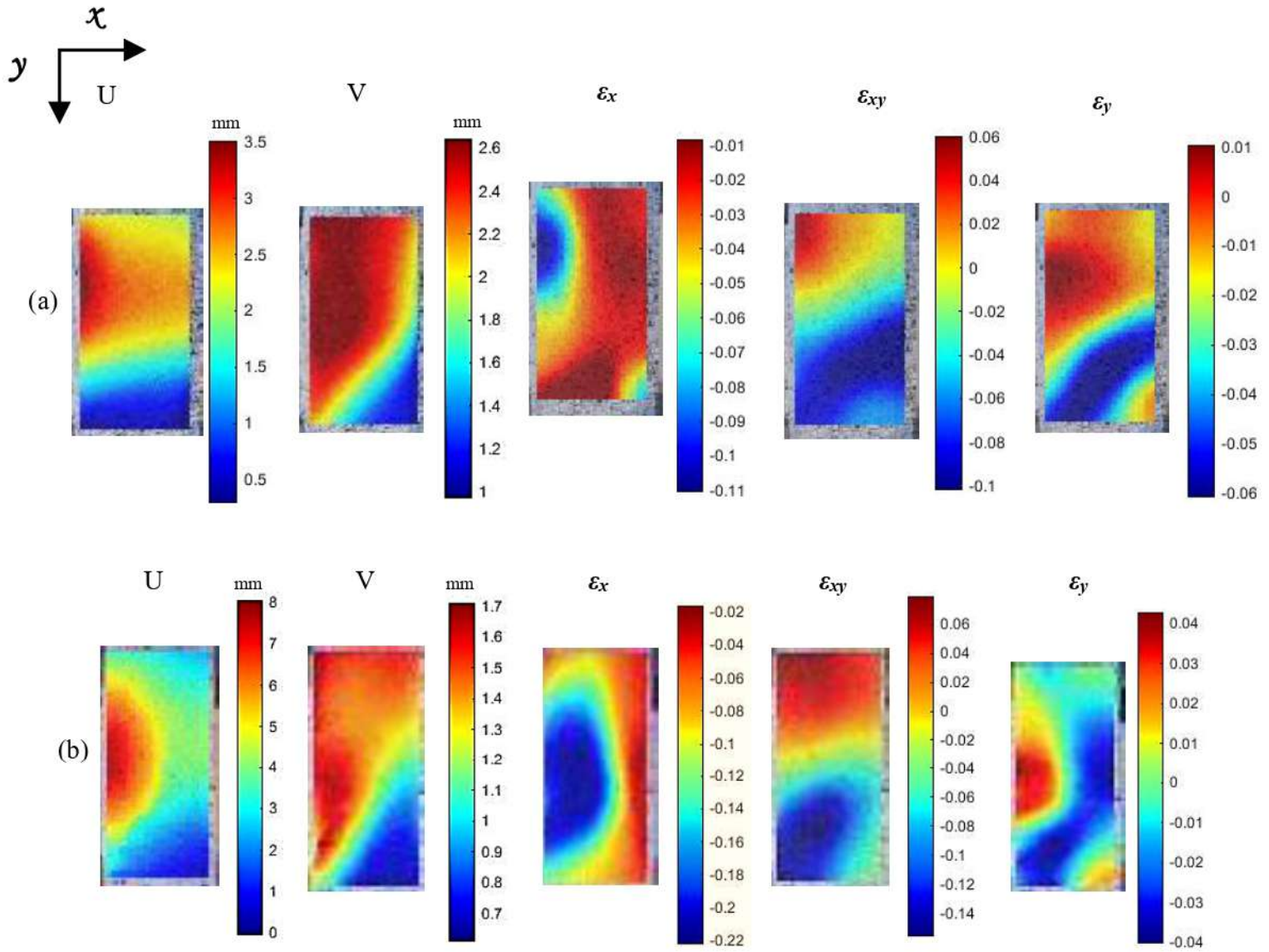


**Figure 4. 3:** DIC engineering displacement and strain fields after edgewise compression test for **S-60**:  
a) SPU, b) SPS.



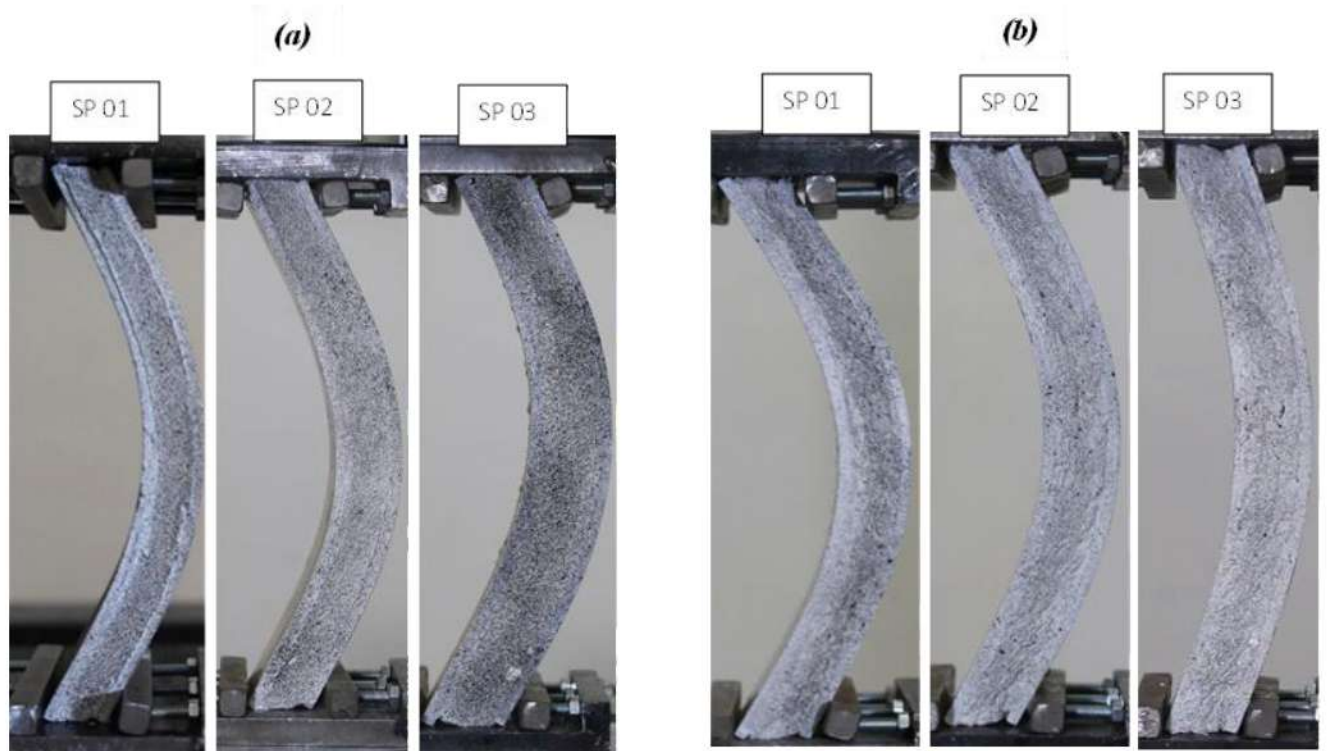


**Figure 4. 4:** Specimens after edgewise compression test for S-200; a) SPU, b) SPS.

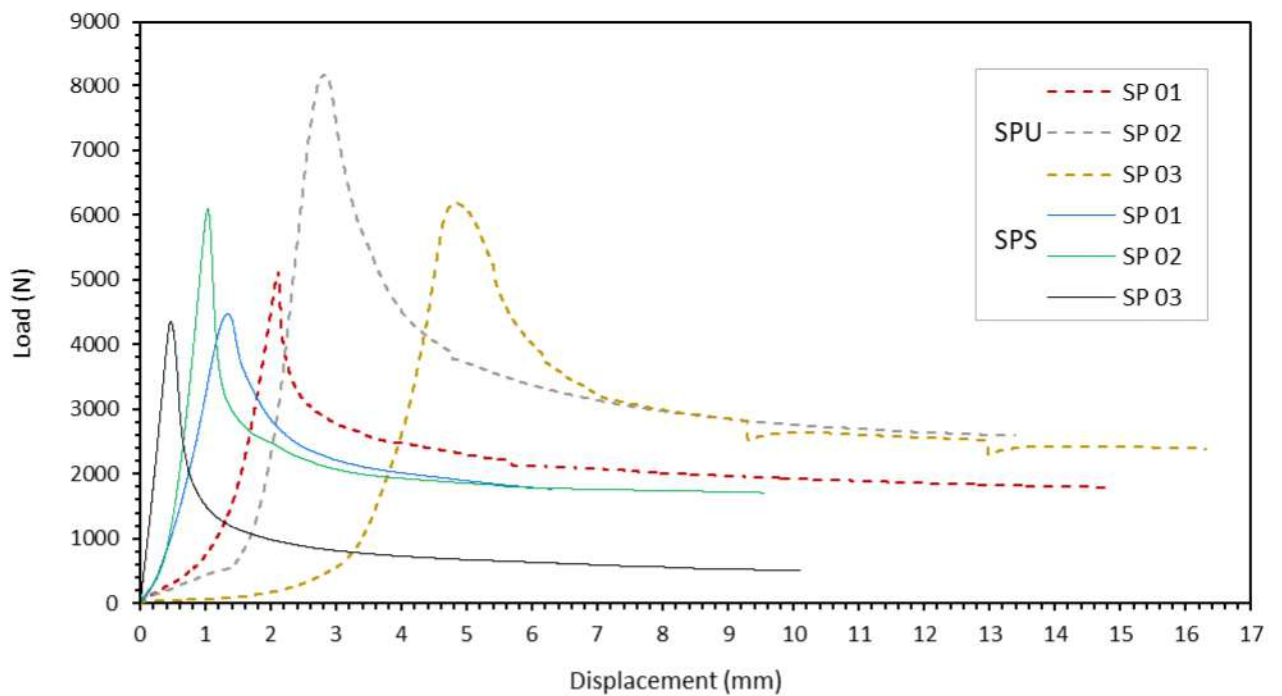


**Figure 4. 5:** Edgewise compression load-displacement curves for SPU and SPS; S-200.



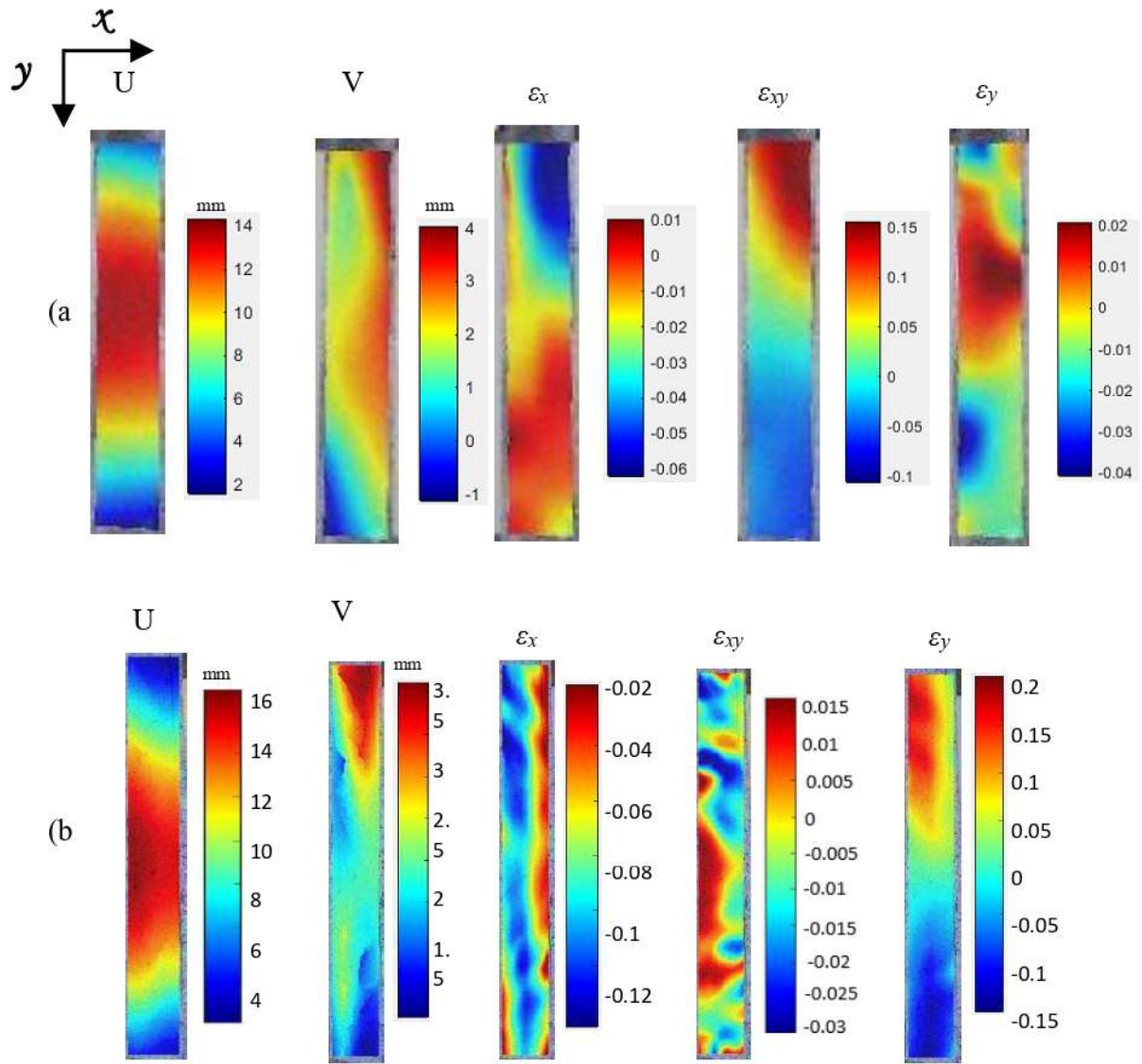


**Figure 4. 6:** DIC engineering displacement and strain fields after edgewise compression test for S-200: a) SPU, b) SPS.

**Table 4. 1** The results obtained through edgewise compression tests for SPU and SPS

			$P_{max}$ (kN)	Displacement (mm)	Ultimate compressive strength (MPa)	Compressive strain (mm/mm)
SPU	S-60	Sp 01	39767.24	4.16	87.21	0.069
		Sp 02	40163.82	5.04	95.63	0.084
		Sp 04	33651.23	2.99	73.79	0.049
		Average	37860.76	4.06	85.54	6,73E-02
		SD	3650.95	1.03	11.01	1,76E-02
		Sp 03	20082.73	0.98	44.87	0.016
	S-200	Sp 01	5140.66	14.78	11.34	0.074
		Sp 02	8176.96	13.38	17.93	0.067
		Sp 03	6182.26	16.30	14.11	0.082
		Average	6487.96	14.82	14.46	0.074
		SD	1558.79	1.46	3.31	7.00E-03
SPS	S-60	Sp 01	42919.86	2.71	94.12	0.05
		Sp 02	29709.02	2.29	65.15	0.04
		Sp 03	33923.27	1.92	74.39	0.03
		Sp 04	31975.61	4.13	70.12	0.07
		Average	34631.94	2.76	75.95	0.046
		SD	5787.429	0.97	12.69	0.02
	S-200	Sp 01	4471.49	6.29	9.09	0.031
		Sp 02	6086.37	15.22	13.35	0.048
		Sp 03	4358.15	10.09	9.36	0.05
		Average	4972.003	10.54	10.6	0.043
		SD	966.73	4.48	2.39	0.01

### 4.3 Flatwise compression test of SPU and SPS

Load-Displacement curves of the SPU and SPS samples subjected to flatwise compression are shown in **Fig 4.7**. As it is marked, the zoomed-in region of the curves of both structures exhibits a similar behavior to PU and PS foams under compression test (**Fig 3.17**), which can be explained by the fact that the core is the first part of sandwich damaging. It is noticed that the curves behave in a comparable performance for both SPU and SPS; a linear behavior representing the elastic deformation until yield point, where SPS yielding at a lower load compared to SPU due to differences in stiffness and strength of the foams. Subsequently, the curves enter a plateau phase where the load remains relatively constant while the displacement continues to increase, which represent that the condensation and collapse of the specimen. Afterward a densification phase was noted where a rapid increasing of load with small displacement. **Fig 4.8** depicts the final failure of the specimens. **Fig 4.9** and **4.10** illustrate the SEM micrograph of flatwise compression of SPU and SPS samples respectively. The samples

were cross-sectioned to obtain the SEM images (**Fig 4.9a and 4.10a**). It is noted that no debonding between skin and core induced by testing is recorded in **Fig.4.9b** and **Fig 4.10b**. This can be attributed to the efficient stress transfer facilitated by the strong interfacial adhesion between the GFRP skin and the foam core under flatwise compression. This loading mode promotes foam densification, which limits interfacial failure and enhances the structural response. The presence of epoxy resin at the interface further improves mechanical integrity due to its high compressive strength and stiffness, enabling effective load distribution between the skin and the core. Furthermore, significant compression of the foam led to extensive cell collapse, making most of the foam cells no longer distinguishable. It is worth noting that the localized gaps observed at the skin–core interface are not indicative of debonding initiated during testing, but rather result from the inherent surface porosity of the foam structure and minor surface imperfections of the skin. The zoomed-in part of the sample (**Fig 4.9c** and **4.10c**) exposes micro-crack in the skin parallel to the loading fixture. This micro-crack may have formed as a result of continuous micro-voids. DIC results of SPU and SPS are shown in **Fig 4.11**. The images were taken just before losing correlation and the map faded caused by foam compression. It is remarkable that the maximum displacement along the load direction (V) is corresponding to the top plate where the load is applied, colored in red and it gradually decreases to zero towards the bottom fixed plate. However, the displacement traverse to the loading (U) indicates an expanding of the foam on both sides in opposite directions and tends to zero in the rest of points. Furthermore, the concentration longitudinal strain  $\varepsilon_y$  in blue signify the densification of the PU and PS foams. The results obtained from the test are listed in **Table 4.2**. The average ultimate flatwise compression strength is 20.99 MPa for both SPU and SPS. The specimens exhibited deformation of 70% and 75% for SPU and SPS, respectively. According to ASTM C-365M the ultimate flatwise compression strength was calculate using *eq. (4.2)*

$$\sigma_{fc} = \frac{P_{max}}{A} \quad (4.2)$$

where  $\sigma_{fc}$  is the ultimate flatwise compressive strength (MPa).  $P_{max}$  is the ultimate force prior to failure (N) and A is the area of the of the surface of facing subjected to compressive load ( $\text{mm}^2$ ).

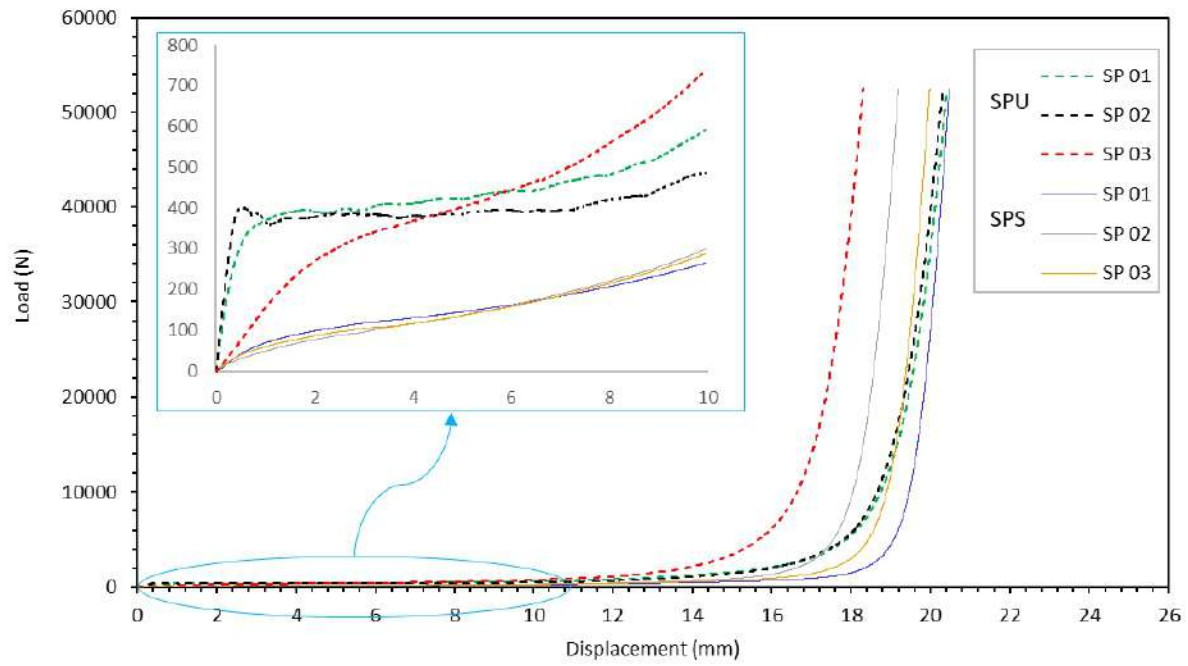


*Figure 4. 7: Flatwise compression Load-Displacement curves*

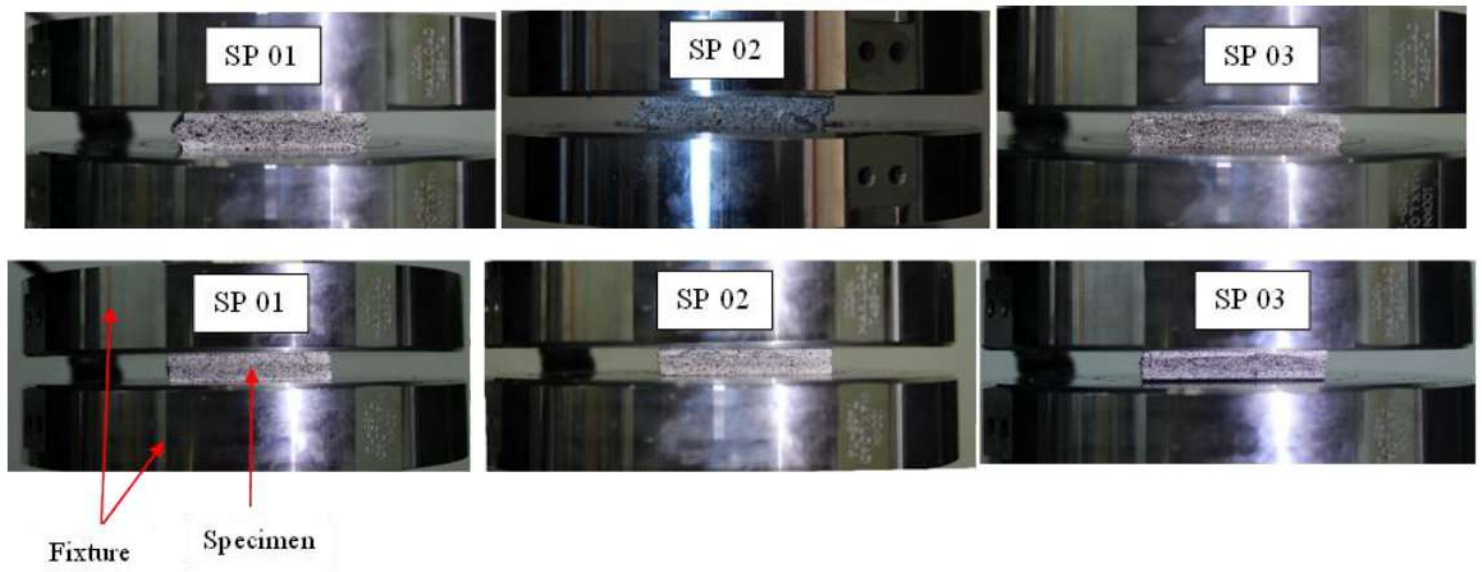


*Figure 4. 8: Specimens after Flatwise compression test.*



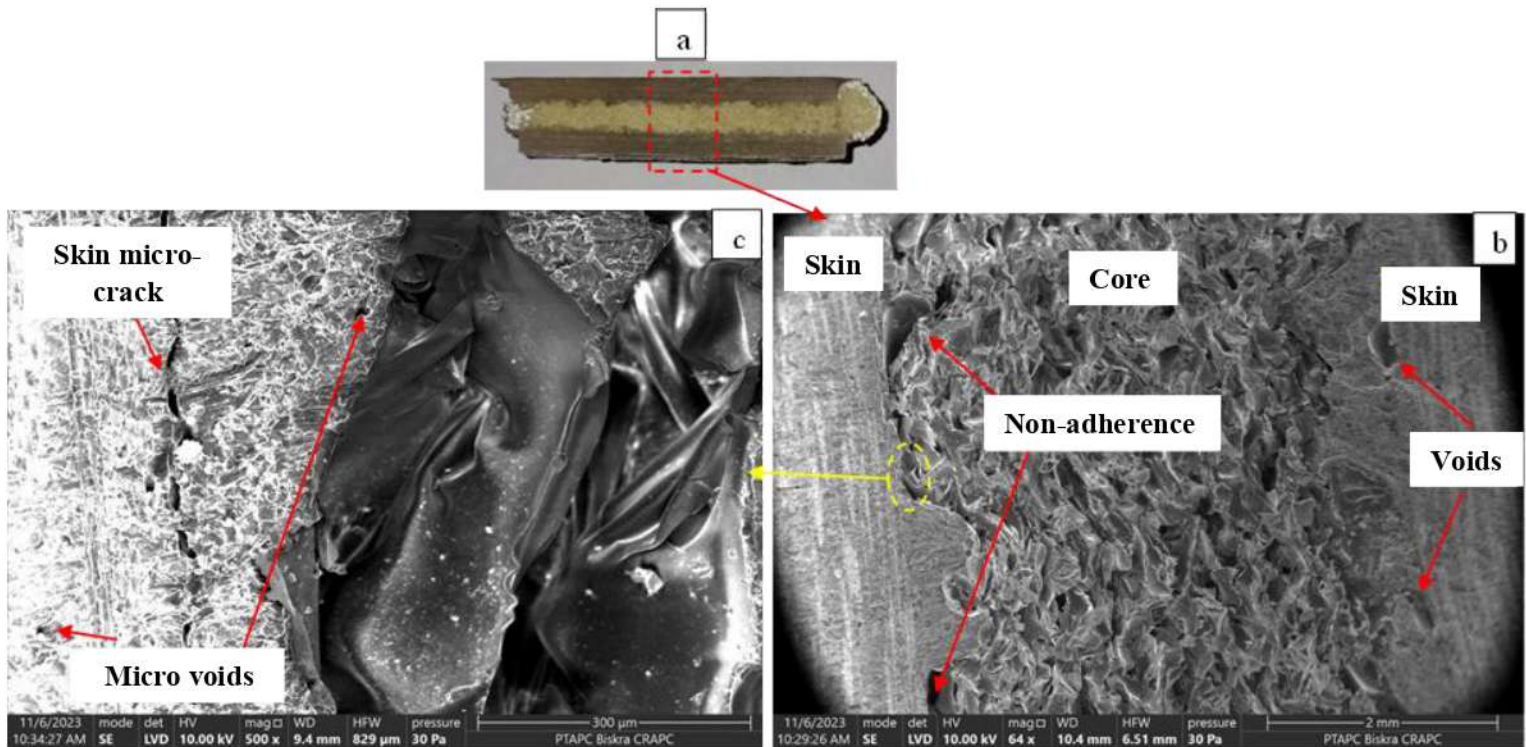


*Figure 4. 9: SEM analysis of SPU subjected to flatwise compression samples.*

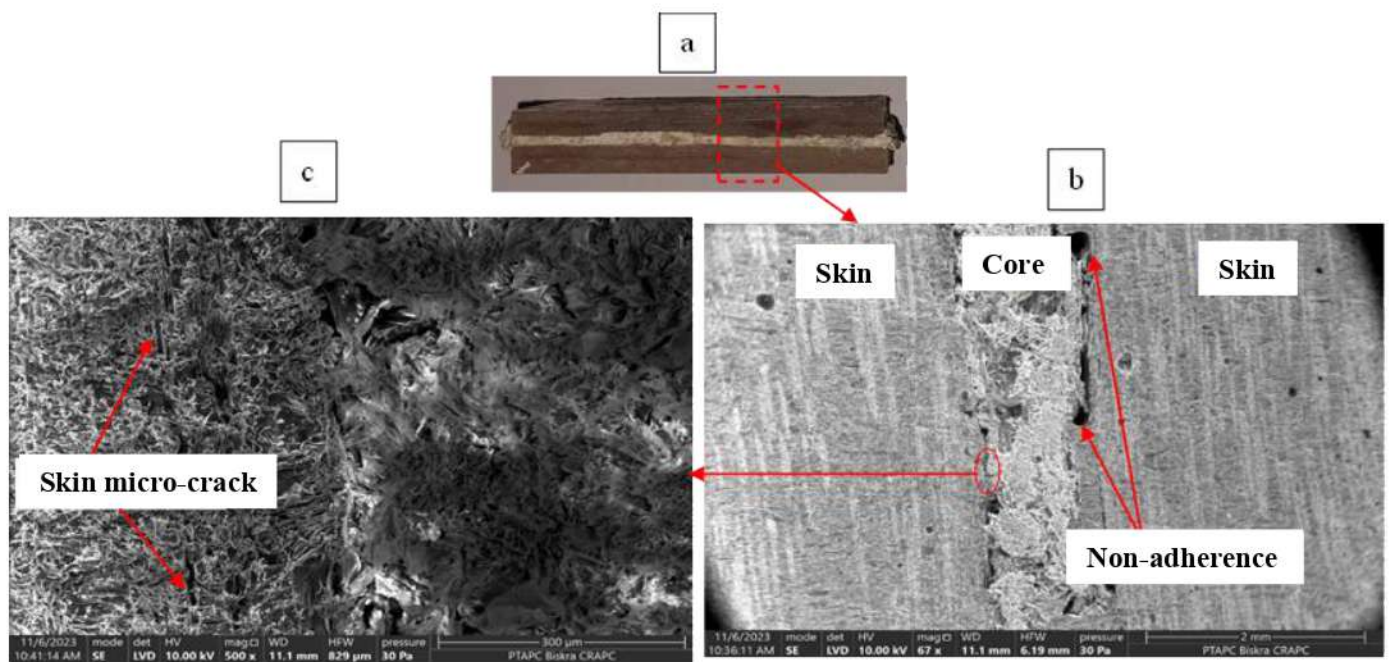


*Figure 4. 10: SEM analysis of SPS subjected to flatwise compression samples.*

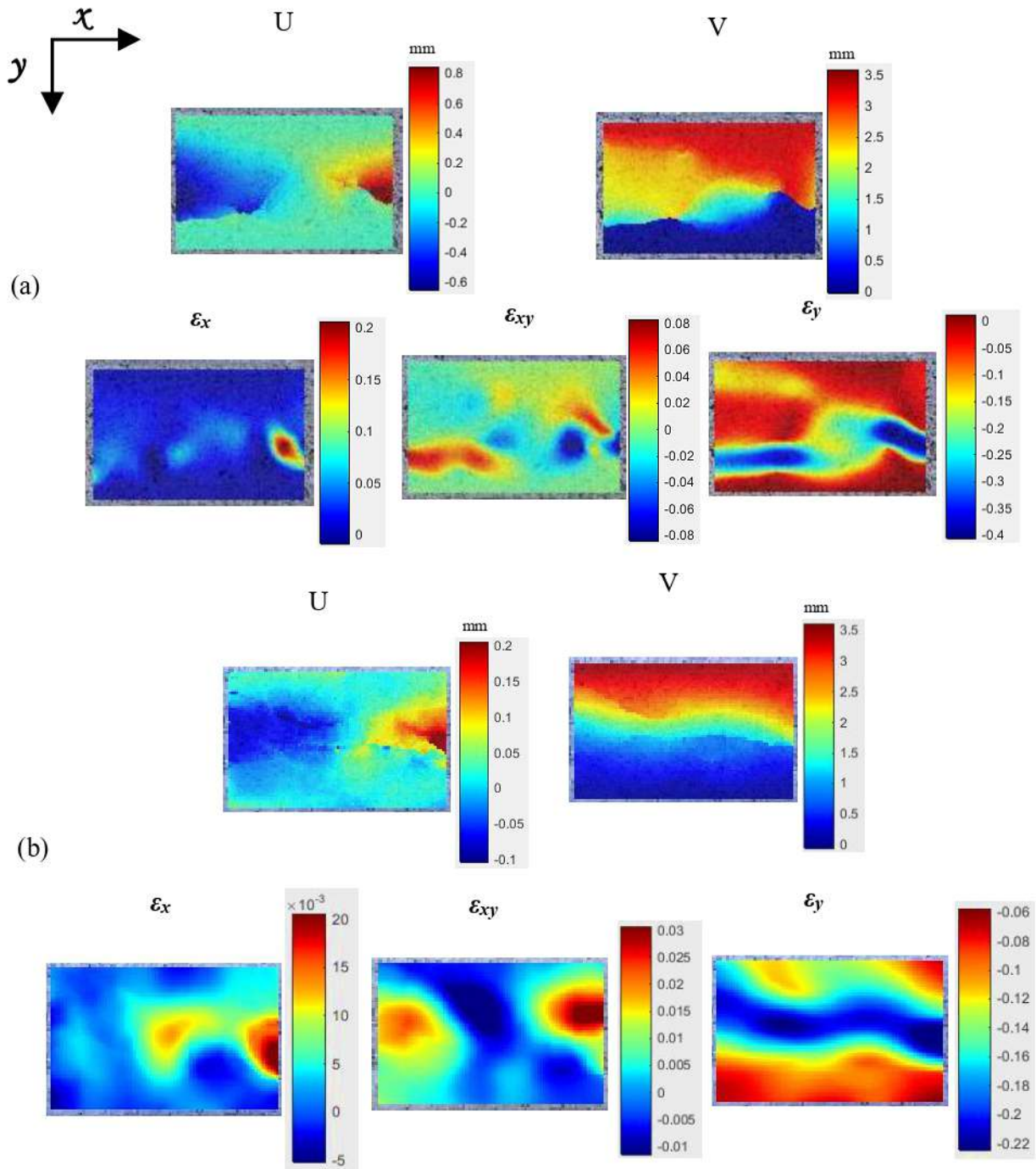


**Figure 4. 11:** DIC engineering displacement and strain fields for flatwise compression test of a) SPU, b) SPS

**Table 4. 2** Mechanical parameters obtained through flatwise compressive test of SPU and SPS

		$P_{max}$ (N)	Displacement (mm)	Ultimate flatwise compressive stress (MPa)	Compressive strain (mm/mm)
<b>SPU</b>	SP 01	52493.59	20.41	20.997	0.68
	SP 02	52483.36	18.31	20.993	0.70
	SP 03	52475.24	20.30	20.990	0.68
	Average	52484.06	19.67	20.99	0.69
	SD	9.195	1.18	3.50E-03	0.011
<b>SPS</b>	SP 01	52495.45	20.47	20.99	0.77
	SP 02	52493.05	19.19	20.99	0.72
	SP 03	52489.24	19.98	20.99	0.76
	Average	52492.58	19.88	20.99	0.75
	SD	3.13	0.64	1.33E-03	0.025

### 4.3 Shear test of SPS

Load-displacement curves are represented in **Fig 4.12** Initially, all specimens exhibit a linear region, representing elastic behavior, where the load increases proportionally with displacement. After reaching the peak, the load drops significantly and the specimens experience a softening phase, indicating damage initiation and progressive failure. **Table 4.3** resumes the results obtained throughout the test. The core shear stress ( $\tau_{max}$ ) and shear modulus ( $G$ ) are calculated in accordance with the ASTM C273-00 standard, as follows:

$$\tau_{max} = \frac{P_{max}}{L.w} \quad (4.3)$$

$$G = \frac{S.t}{L.w} \quad (4.4)$$

Where  $S$ ,  $t$ ,  $L$ ,  $w$  are the slope of initial portion of load-displacement curve, thickness, length of specimen and width of specimen respectively.

**Fig 4.13** depicts the failure mode of SPS subjected to shear test. The failure mechanism is predominantly characterized by core shear failure, with PS foam core exhibiting substantial deformation and fracture along planes parallel to the fixture of the test. The damage is primarily concentrated in the central region of the core, where shear stresses are highest. Additionally, the failure mechanism involves debonding between GFRP skin and the PS foam, particularly at the ends of the specimens. This debonding is likely due to stress concentrations at the



interface between the skin and the core, leading to interfacial failure. Notably, no debonding is observed between the specimens and the shear test fixture, indicating that the failure is intrinsic to the material and not influenced by the testing setup. DIC analysis, as shown in **Fig 4.14**, provides detailed insights into the displacement and strain fields of the SPS during the shear test. The DIC results reveal high strain concentrations along the shear strain  $\epsilon_{xy}$  and  $\epsilon_y$  components, which are critical indicators of shear failure initiation and propagation. These strain concentrations align with the observed failure patterns, confirming that the core shear failure is determined by localized shear deformation.

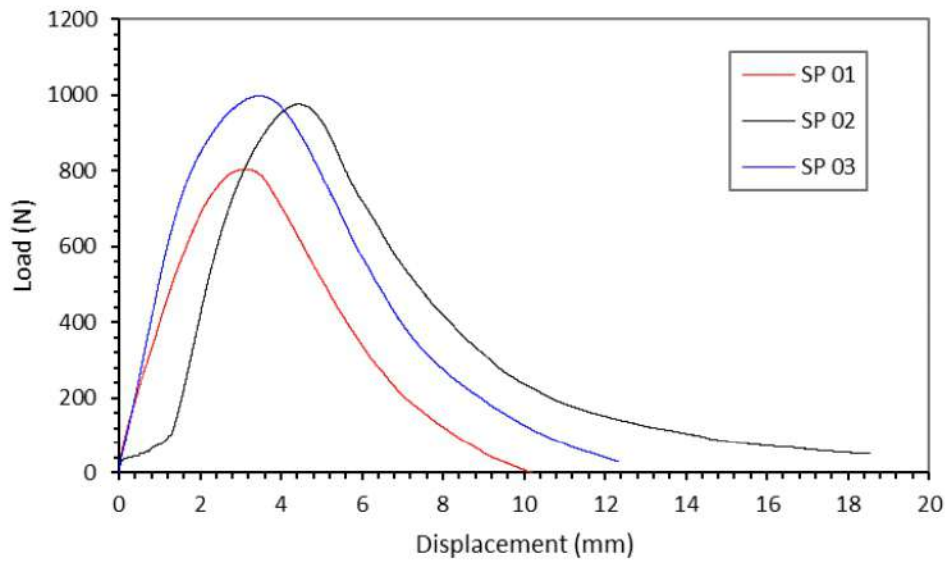


**Figure 4. 12:** Load-displacement curves for SPS specimens subjected to shear test.

**Table 4. 3** Mechanical parameters obtained through shear test of SPS.

	Pmax (N)	Correspondent displacement (mm)	Maximum Core Shear Stress (MPa)	Correspondent Strain (mm/mm)	G (MPa)
Sp 01	803.91	3.08	0.032	0.0123	0.776
Sp 02	975.75	4.44	0.039	0.0178	0.553
Sp 03	997.29	3.46	0.0392	0.0138	0.714
Average	925.65	3.66	0.037	0.0146	0.681084
SD	105.98	0.7	4.24E-03	0.002	1.15E-01





*Figure 4. 13: Samples after shear test of SPS*

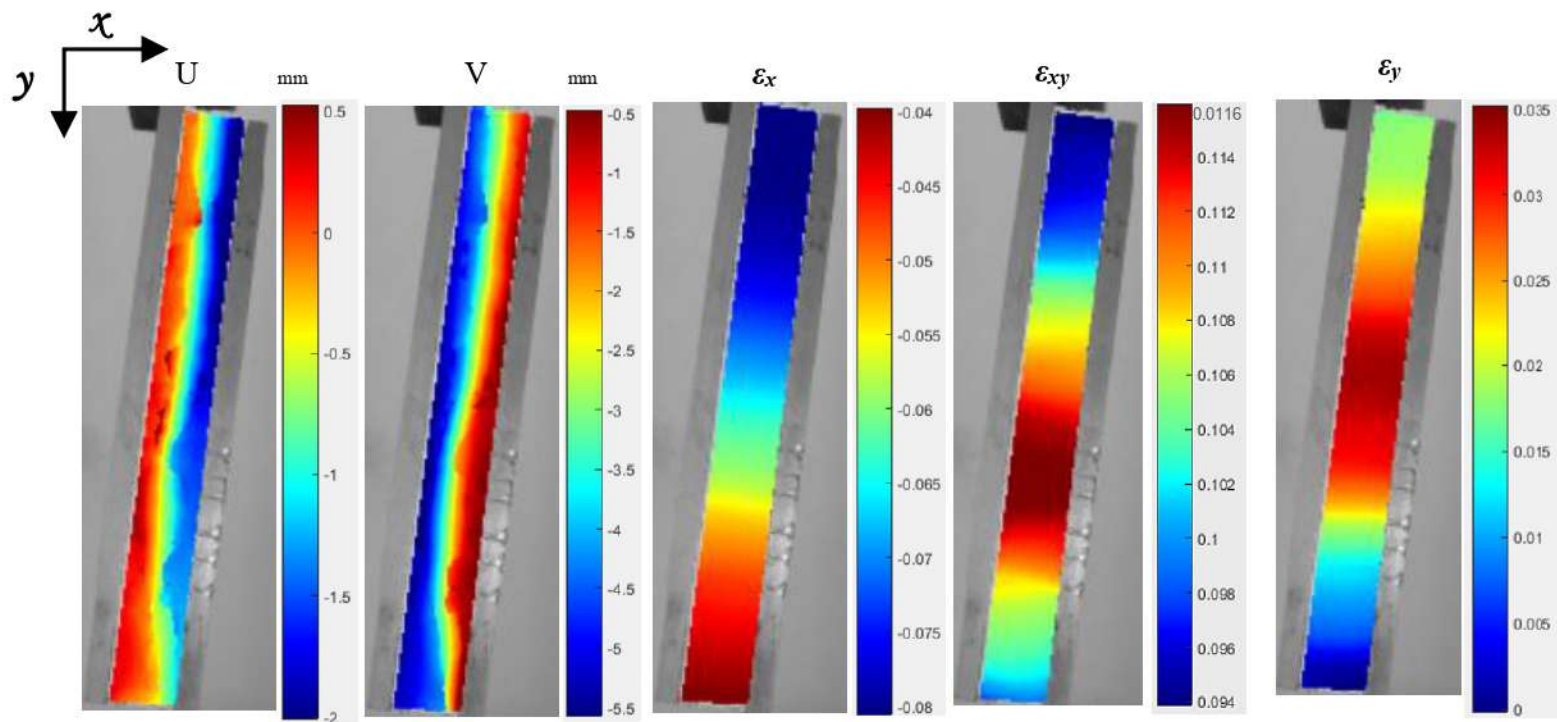


*Figure 4. 14: DIC engineering displacement and strain fields of SPS after shear test.*

#### 4.4 Flexural test of SPS

The flexural behavior of SPS specimens was analyzed under two different loading conditions; static loading (S-L) and cyclic loading (C-L 1 and C-L 2). The load-displacement curves for specimens obtained for both loading conditions are presented in **Fig 4.15**. The curve of static loading exhibits a linear increase, indicating that both the core and skins function cohesively without noticeable damage. However, by loading progressing, the response deviates from linearity, suggesting the onset of damage mechanisms as core shear deformation and initial debonding. It is important to note that the maximum load does not precisely represent the failure load; the test was manually finished after reaching a mid-span displacement of approximately 70 mm. The load-displacement response under cyclic loading displays a reasonable correlation with static loading response. With an increasing of number of cycles, the repeated load application leads to progressive stiffness degradation, resulting from microcracks propagation and specimen damage. Upon unloading, the specimens regained approximately 83% of their maximum recorded displacement during the test. The failure analysis of the tested specimens, as depicted in **Fig 4.16**, reveals a combination of core shear failure, skin-core debonding, and foam densification. The key mechanical results from both loading conditions are summarized in **Table 4.4**. **Fig 4.17** illustrates DIC engineering of vertical displacement for both static and cyclic loads. The images were taken just before losing correlation.

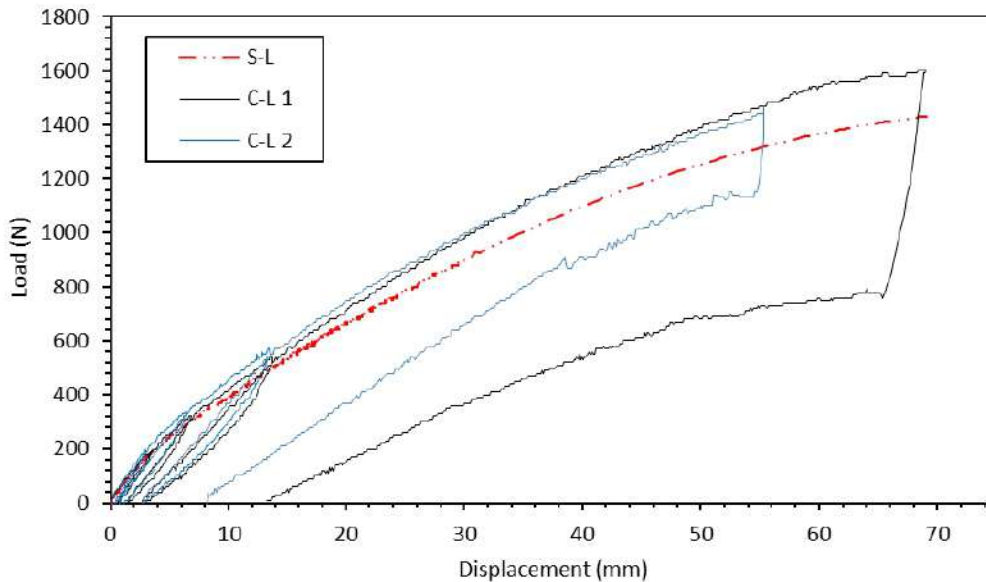


**Figure 4. 15:** Load-displacement curves for SPS specimens subjected to static and cyclic bending tests.





**Figure 4. 16:** SPS specimen after test; a) S-L, b) C-L

**Table 4. 4** Summary of main results from static and cyclic bending test for SPS specimens.

Pmax (N)				Correspondent displacement (mm)			E (MPa)		
S-L	1430.55			69.06			52.79		
C-L	C-L 1	C-L 2	Average	C-L 1	C-L 2	Average	C-L 1	C-L 2	Average
Cycle 01	200.00	200.00	200.00	3.60	3.02	3.31	144.79	163.58	154.185
Cycle 02	320.00	340.00	330.00	6.84	6.46	6.65	103.29	125.82	114.55
Cycle 03	540.00	570.00	555.00	13.81	13.51	13.66	91.93	97.87	94.9
Cycle 04	1600.00	1460.00	1530.00	69.06	55.36	62.21	76.78	96.71	86.75

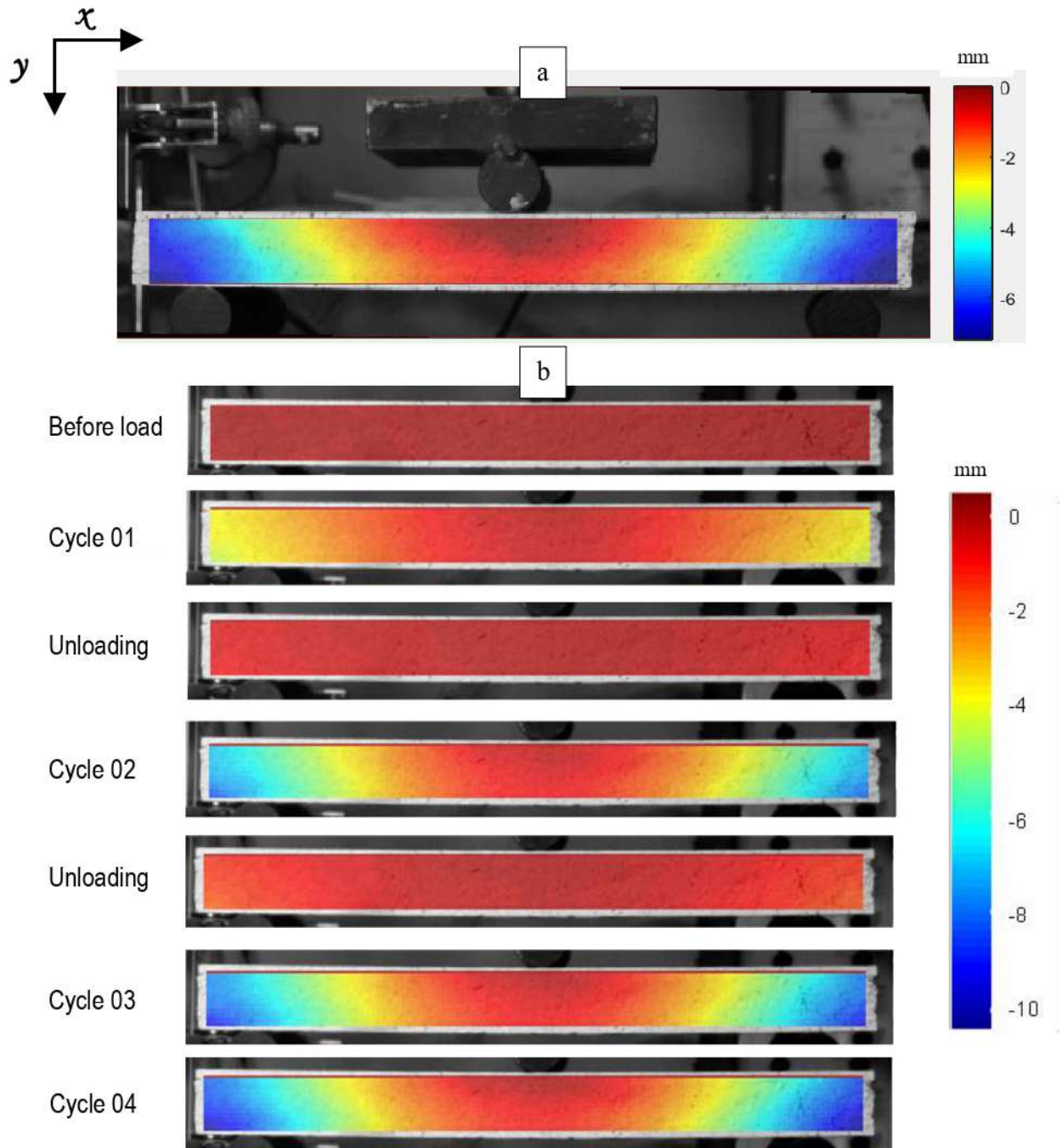


**Figure 4. 17:** DIC analysis of vertical displacement of specimen; a) S-L, b) C-L.



## 4.5 Conclusion

Series of test were conducted on sandwich structures with PU and PS foams. The mechanical properties were obtained through different tests. The tests revealed that both SPU and SPS almost responded similarly in edgewise and flatwise compression loadings. A combination of failure mode was detected. The results show that the length of samples has a significant effect on the collapse modes of sandwich structures under edgewise compression for both SPU and SPS. The shear test of SPS samples reveals core shear failure and skin-core at the ends of the specimens. The flexural behavior of SPS specimens was analyzed under two different loading conditions. The specimen experienced a combination of core shear failure, skin-core debonding, and foam densification for both conditions. For cyclic loading, the specimens regained approximately 83% of their maximum recorded displacement during the test, upon unloading.

***CHAPTER 05***  
**MECHANICAL  
BEHAVIOR OF SRP**

# CHAPTER 05. MECHANICAL BEHAVIOR OF SRP

---

## 5.1 Introduction

Due to the inherent limitations in shear strength and stiffness of foamed sandwich structures, the integration of reinforced pins within the core has been proposed as a means to enhance their structural performance. This chapter explores the impact of reinforced pins on the mechanical behavior of sandwich composites (SRP), with a particular focus on key mechanical properties under shear and flexural loading conditions.

## 5.2 Shear test of SRP

*Fig 5.1* presents the load-displacement curves for SPS and SRP specimens subjected to shear testing. The Fig highlights the impact of incorporating reinforced pins into the core of the sandwich structure. As shown, the SRP curves display a steeper slope in the linear elastic region of the curves, indicating significantly higher stiffness compared to the SPS specimens. This behavior reveals that the reinforced pins enhance the core's rigidity, resulting in both improved resistances to shear loads and a higher peak load compared to the SPS specimens. Once the load reaches its maximum, it is evident that the SRP specimens show a more gradual decline, indicating a progressive failure mechanism rather than an abrupt collapse. *Table 5.1* resumes the main results obtained from the test. The maximum core shear stress and shear modulus are calculated as mentioned in equations 4.3 and 4.4, respectively. The histograms in *Fig 5.2* provide a detailed comparison of the  $\tau_{\max}$  and  $G$  for SRP and SPS. As shown, both  $\tau_{\max}$  and  $G$  nearly doubled, representing a significant enhancement in their shear resistance and stiffness. Failure mode of SRP specimens subjected to shear test is shown in *Fig 5.3*. Similar to SPS specimens, core shear failure is the dominant mechanism. Core revealing significant deformation and fracture along planes parallel to the test fixture. The damage is mainly concentrated in the central region of the core. Furthermore, skin-core debonding observed in SRP specimens was slightly reduced compared to SPS. No debonding is detected between the specimens and the shear test fixture, demonstrating that the failure is inherent to the material and not influenced by the testing setup. *Fig 5.4* displays DIC maps illustrating the displacement and strain fields of the SRP specimen. The maps were captured just before losing correlation. It is observable that strain distribution reveals a distinct concentration in the central region of

the specimen where the initiation of failure. Furthermore, as expected, the highest vertical displacement is detected at the region of load application.

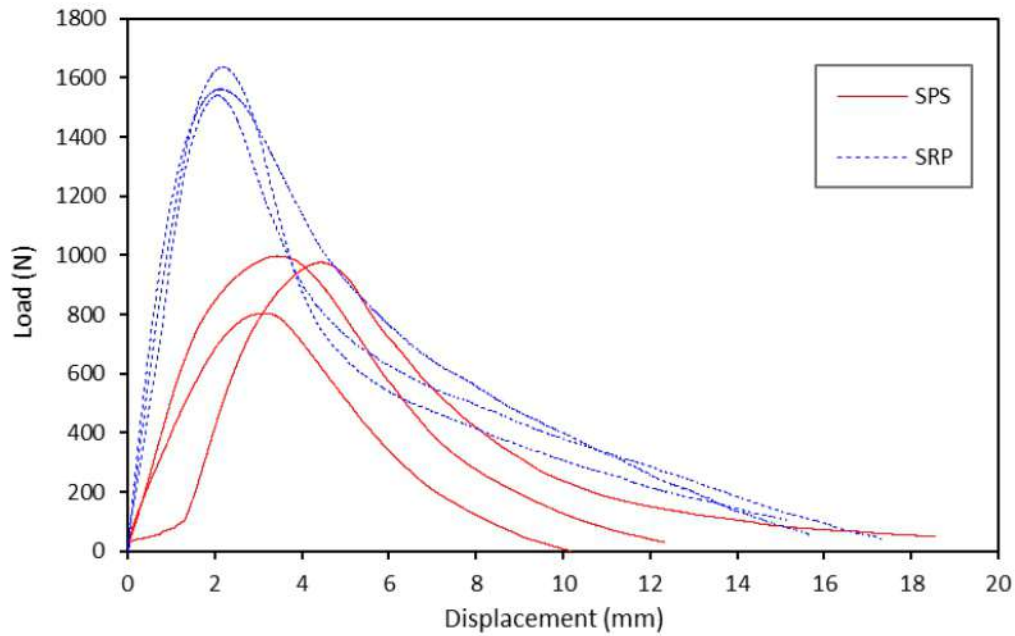


**Figure 5. 1:** Load-displacement curves for SPS and SRP subjected to shear test.

**Table 5. 1** Mechanical parameters obtained from shear test of SRP samples.

	Pmax	Correspondent displacement (mm)	Maximum Core Shear Stress (MPa)	Correspondent Strain (mm/mm)	G(Mpa)
Sp 01	1562.47	2.15	0.062	0.009	1.281
Sp 02	1541.26	2.05	0.061	0.008	1.432
Sp 03	1637.39	2.18	0.061	0.009	1.328
Average	1580.38	2.13	0.062	0.009	1.347
SD	50.51	0.07	9.31E-04	6 E-04	7.73E-02



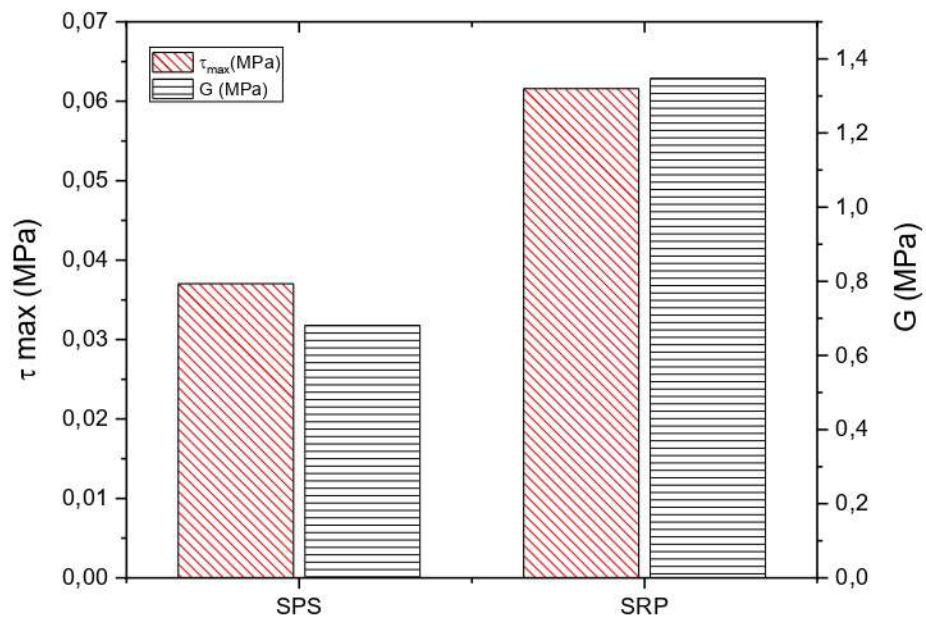


*Figure 5. 2: Comparison of  $\tau_{max}$  and G for SRP and SPS.*



*Figure 5. 3: SRP specimens after shear test.*

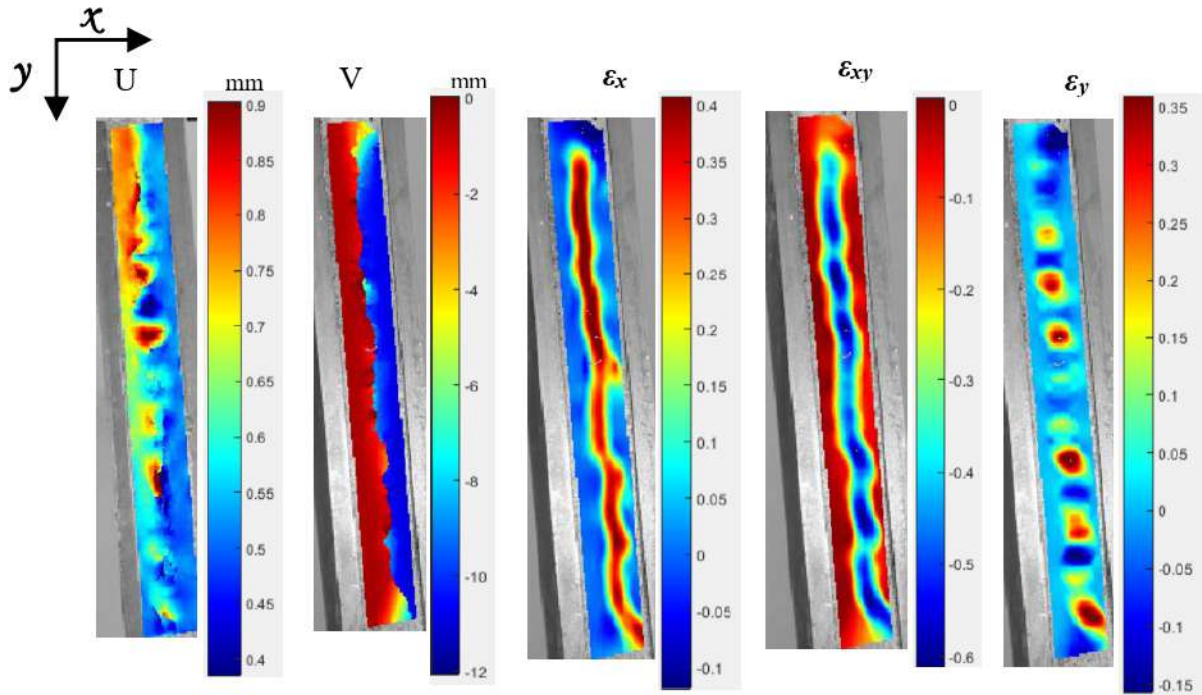


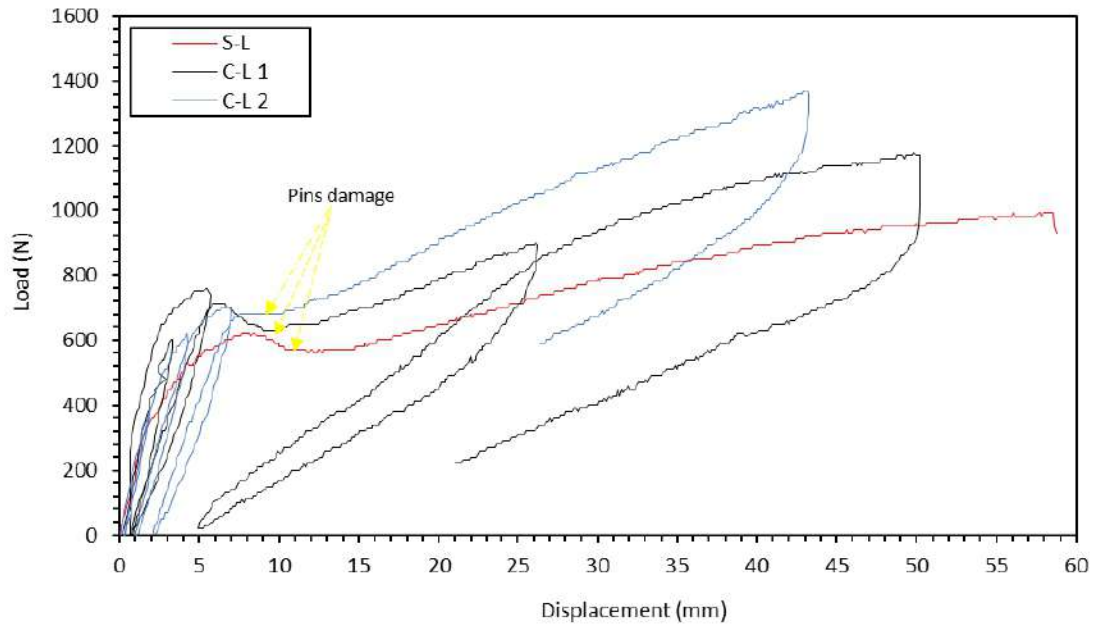
*Figure 5. 4: DIC engineering displacement and strain fields of SRP specimens under shear load.*

## 5.2 Flexural test of SRP

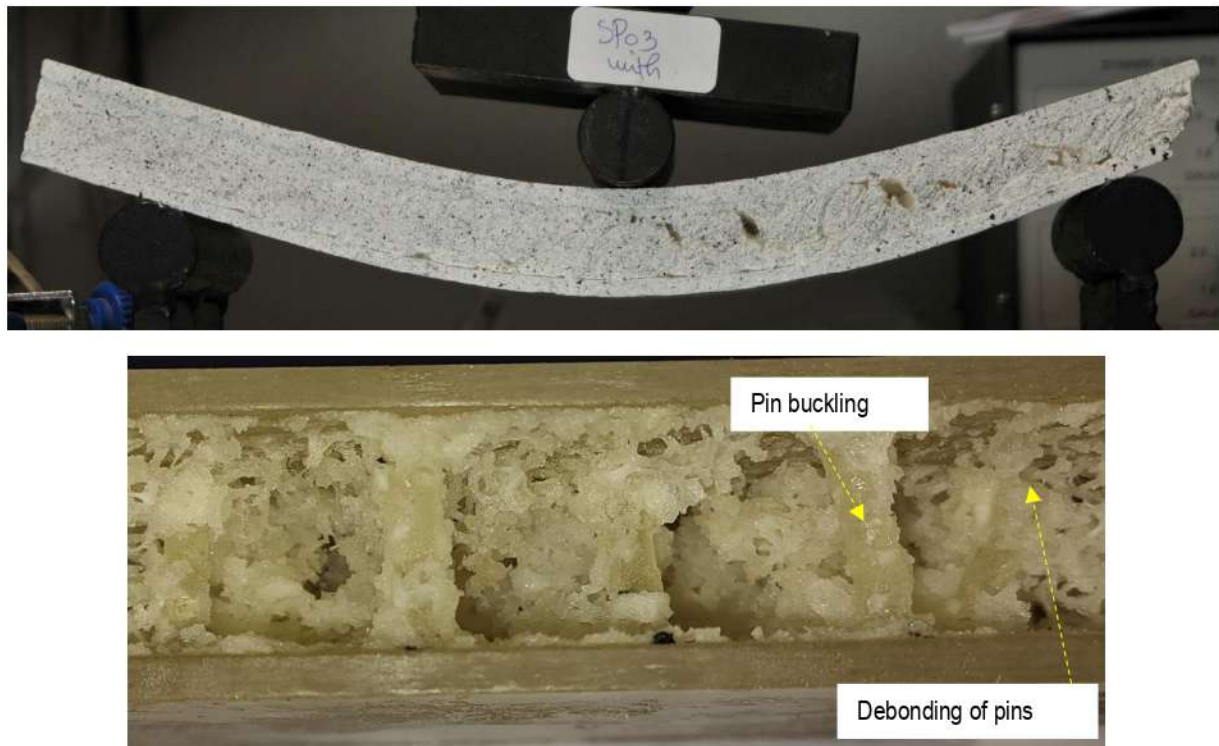
Similar to the flexural test for SPS specimens, the flexural behavior of SPS specimens was investigated under two different loading conditions; static loading (S-L) and cyclic loading (C-L 1 and C-L 2). The corresponding load-displacement curves for both loading conditions are illustrated in **Fig 5.5**. The specimen under static loading displays a linear performance, followed by load drop, which is attributed to pins damage. This damage may occur due to shear failure of the pins or debonding. After the initial failure, the load gradually increases again. The response of SRP subjected to cyclic loading follows a similar trend the static case. However, with each loading cycle, the specimens experience a progressive stiffness reduction. Also, a load drop is noticed in cycle 3 and 4 for C-L 1 and C-L 2, respectively. This load drop is related to pin failure. For C-L 1, a significant stiffness decrease is detected in final cycle subsequent the pins damage. After unloading the specimen, about 57% and 39% of maximum recorded displacement were recovered for C-L 1 and C-L 2, respectively. The fracture mechanism for the specimens is shown in **Fig 5.6**. Clear core shear is observed, additionally, foam densification is particularly remarked in areas where the pins de-bonded from the skin. To further analyze the failure mode, a solvent was applied on remove PS foam revealing the pins' condition. **Fig 5.6b** highlights pin debonding and pin buckling. The main results of the tests are resumed in

**Table 5.2.** As expected, a degradation in Young's modulus with cycle number progressing. To refine the assessment of the impact of incorporating reinforced pins in sandwich composites and comparison analysis of mechanical properties are presented in **Fig 5.7** and **Fig 5.8**. The remarkable difference in SPS and SRP response when subjected to static and cyclic loading demonstrated the substantial improvement in stiffness achieved through the integration of reinforced pins. This enhancement is particularly apparent in **Fig 5.8**, which confirms a considerable increase in flexural Young's modulus. The DIC analysis of vertical displacement of SRP specimen subjected to cyclic loading is shown in **Fig 5.9**. The maps were captured just before loss of correlation in each cycle. The highest vertical displacement values are concentrated in the support regions where the load is applied. The displacement results for loading and unloading phases of cycle 1 and 2 as well as the unloading phase of cycle 3, exhibit strong agreement with the measurements obtained from experimental testing machine, demonstrating the reliability of the DIC technique in capturing displacement fields under cyclic loading conditions. In **Fig 5.10**, the strain fields prior failure are presented. The strain distributions highlight regions of high deformation, with pronounced strain concentrations indicating the core failure. The Ncorr-post processing tool was employed to export the vertical strain of SPS and SRP specimens under cyclic loading. Three virtual extensometers were positioned by selecting two points in the support regions as provided in **Fig 5.11**: 1a-1b, 2a-2b, 3a-3b for ext 1, ext 2 and ext 3, respectively. The vertical strain evolution, extracted from the virtual extensometers, is illustrated in **Fig 5.12**. It is evident that SRP specimen exhibits a more stable and gradual increase in strain when considering the absolute strain values. In contrast, SPS specimen undergoes higher overall deformation.





**Figure 5. 5:** Load-displacement curves for SRP specimens subjected to static and cyclic bending tests.

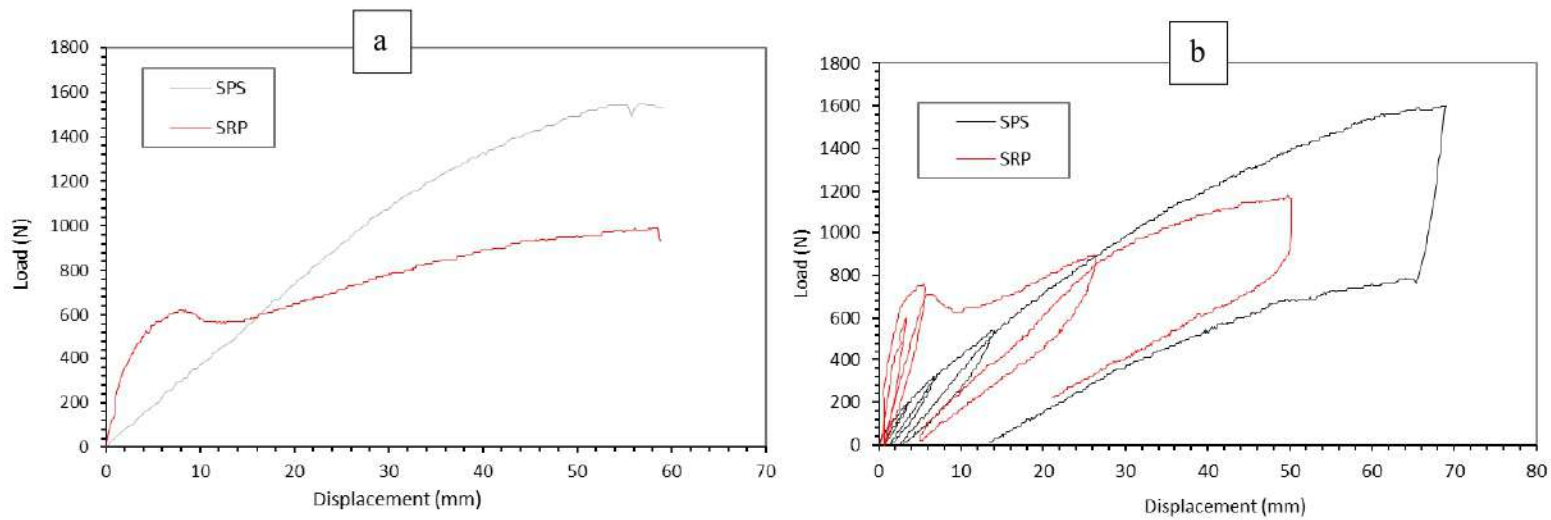
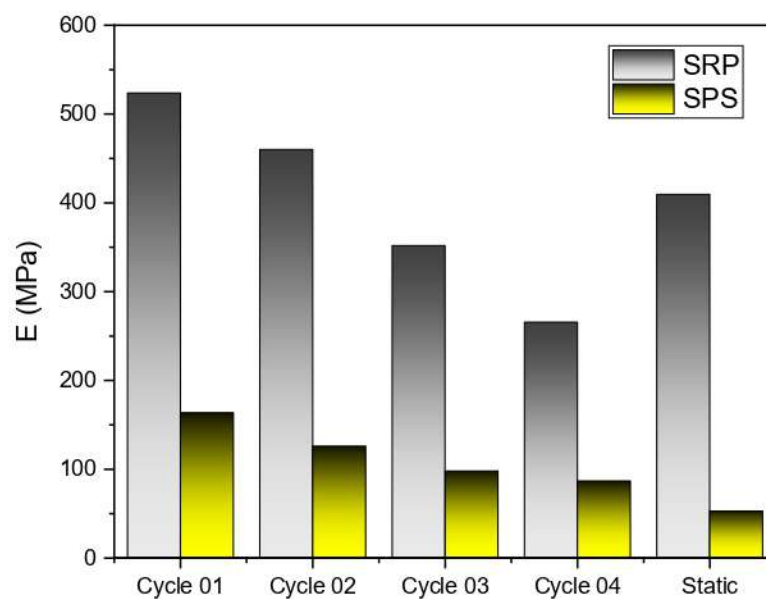


**Figure 5. 6:** a) SRP specimen after flexural test, b) Failure of reinforced pins.



**Table 5. 2** Summary of main results from static and cyclic bending test for SRP specimens.

Pmax (N)			Correspondent displacement (mm)		E (MPa)	
S-L	990		58.57		409.52	
C-L	C-L 1	C-L 2	C-L 1	C-L 2	C-L 1	C-L 2
Cycle 01	600.00	380.00	3.32	1.9	500.17	523.61
Cycle 02	760.00	620.00	5.53	4.25	382.96	459.96
Cycle 03	900.00	700.00	26.17	7.05	282.90	351.72
Cycle 04	1170.00	1370	49.11	43.16	72.76	265.52

**Figure 5. 7:** Load-displacement curves for SRP and SPS samples: a) Static loading, b) Cyclic loading.**Figure 5. 8:** Comparison of flexural Young's modulus of SRP and SPS.

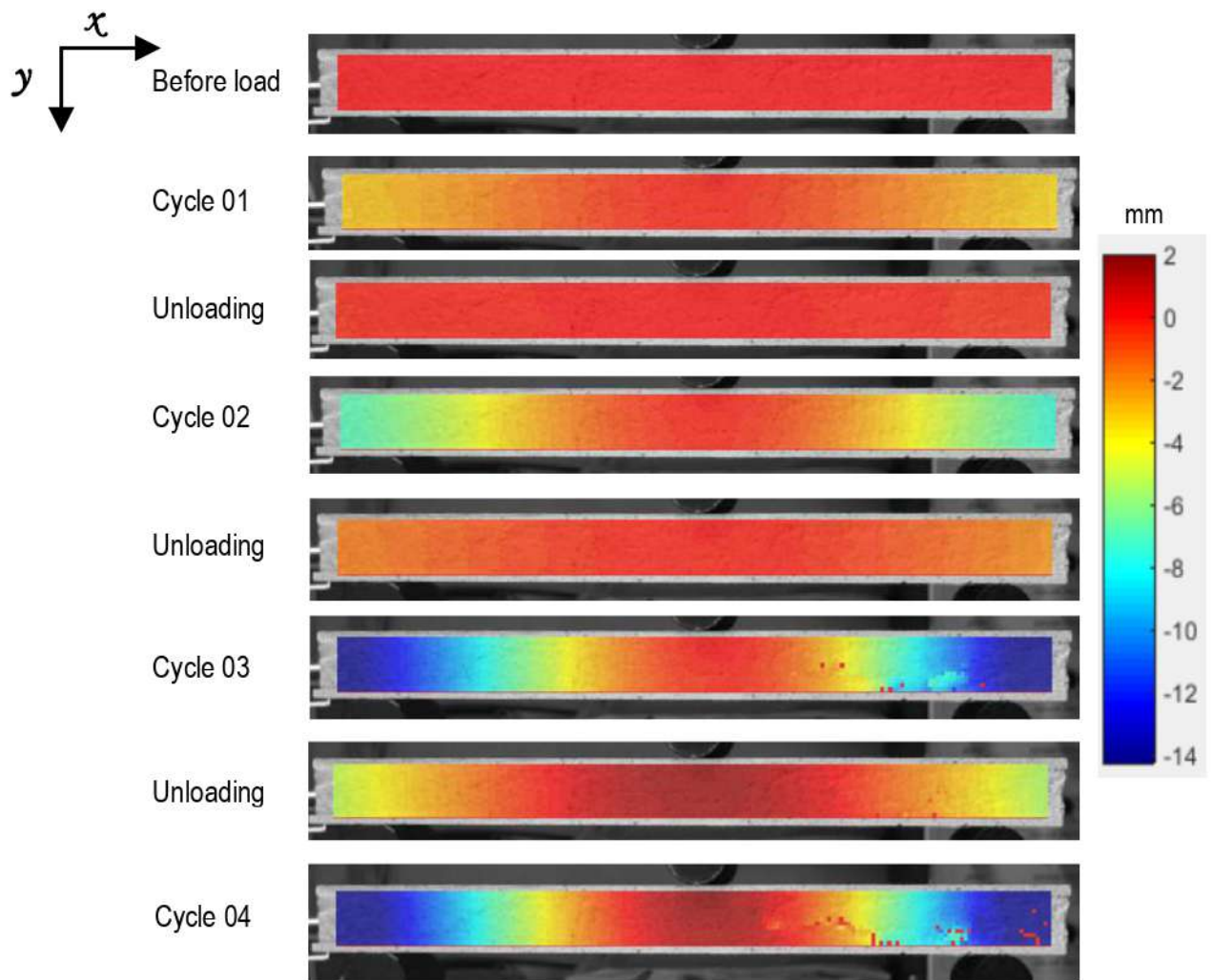


**Figure 5. 9:** DIC engineering of vertical displacement of SRP subjected to cyclic flexural loading.

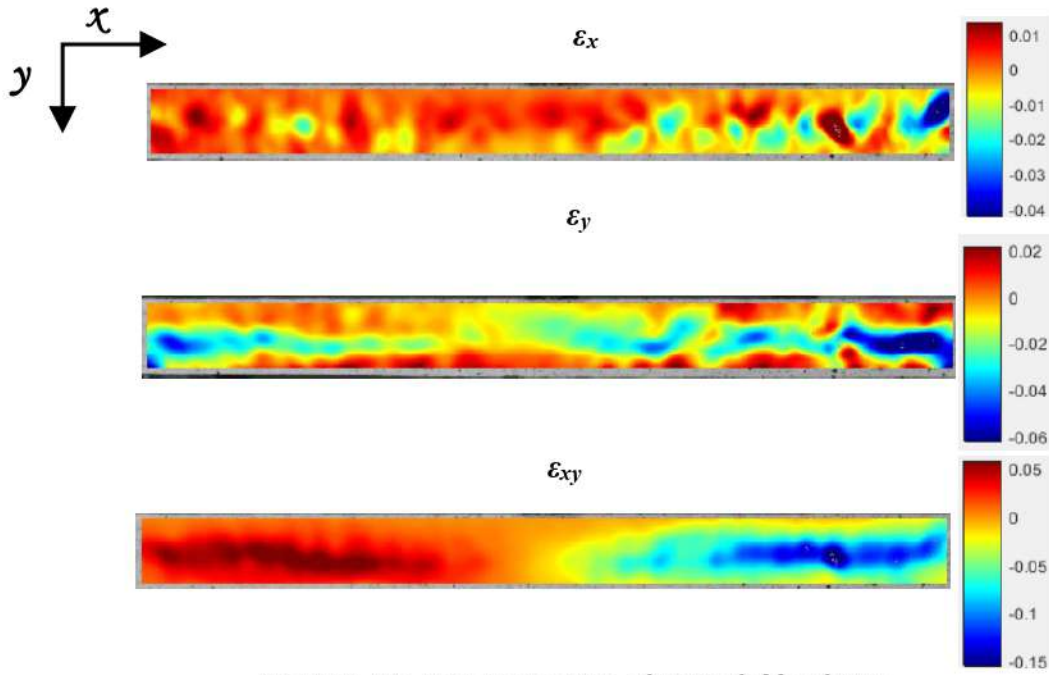


Figure 5.10: DIC engineering of strain fields of SRP.

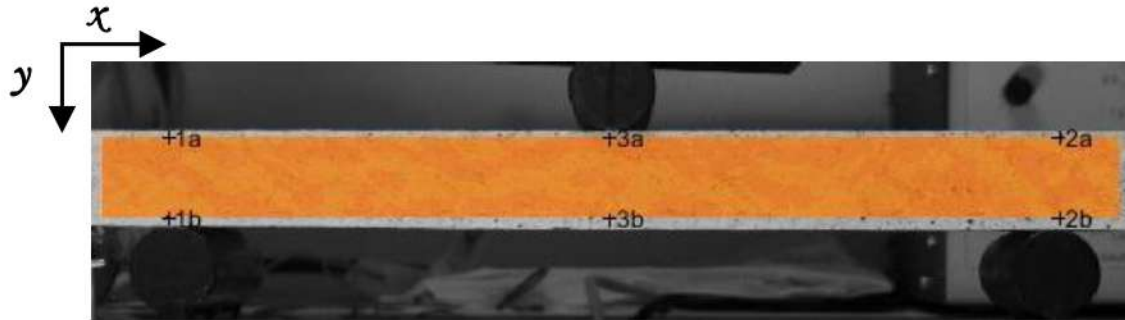


Figure 5.11: virtual extensometers to obtain vertical strain  $\epsilon_y$ .

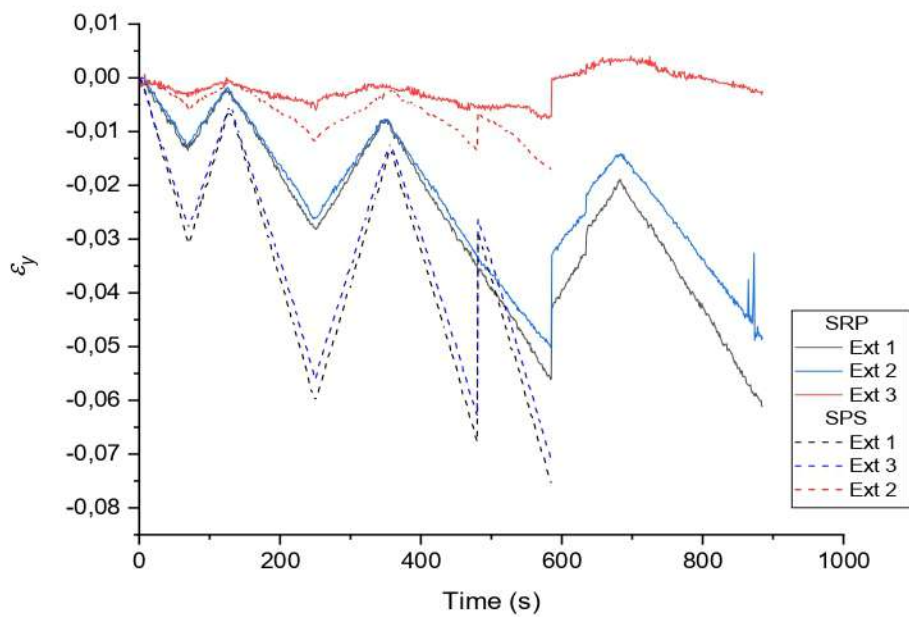


Figure 5.12: The vertical strain evolution of SRP and SPS specimens under cyclic loading.

## 5.4 Conclusion

This chapter explored the incorporation of reinforced pins in foamed sandwich composites and its impact on mechanical performance. To assess this influence, shear and flexural tests were conducted. A comparative analysis between foam core and hybrid reinforced core was presented. The results from both tests demonstrate that the addition of pins enhances key mechanical properties, including core shear stress, shear modulus, and flexural stiffness. The shear tests revealed that the reinforced core exhibited superior shear resistance, indicating improved load transfer within the structure. Similarly, the flexural tests showed a notable increase in stiffness. DIC technique was utilized to more comprehend the failure mode.



# GENERAL CONCLUSION AND PERSPECTIVES

---

## General conclusion

Sandwich structures have long been recognized for their ability to combine lightweight cores with strong, durable skins, providing excellent mechanical properties like high bending stiffness, impact resistance, and efficient load distribution. However, the efficiency of sandwich composites largely depends on the integrity of the bond between the skins and the core, as well as the material's response to various loading conditions. In this context, this thesis evaluated the mechanical performance of sandwich composites incorporating Glass Fiber Reinforced Polymer (GFRP) skins and various foam cores. Particular attention was given to the comparative behavior of polyurethane (PU) and polystyrene (PS) foam cores, as well as a hybrid core reinforced with vertical pins. The research aimed to assess how foam type and pin reinforcement influence the structural integrity and damage tolerance of the sandwich panels under several loading conditions.

The main results of the study are summarized as follows:

- The use of Digital Image Correlation (DIC) throughout all tests showed a high level of consistency with the mechanical testing results, further validating the accuracy and reliability of the DIC measurements.
- The GFRP plates exhibited distinct failure mechanisms under different loading conditions. Under tensile loading, the plates demonstrated a strength of 151.12 MPa, with failure characterized by fiber-matrix debonding, fiber breakage, and fiber pull-out. In compression, the material showed a combination of longitudinal splitting and interlaminar cracking. The three-point bending test revealed layer delamination and fiber breakage, primarily at the mid-span region. In contrast, the four-point bending test produced a more complex failure mode involving significant interlaminar shear failure and severe delamination within the load span region, attributed to high interlaminar shear stresses distributed at load span region.
- The mechanical tests on sandwich structure with PU and PS foams (SPU and SPS) almost responded similarly in edgewise and flatwise compression loadings. Different failure mechanisms were distinguished for sandwich structures under edgewise compression load. With length equal to the width the samples experienced skin-core debonding, shear sliding damage of the skin, and localized buckling in the mid-section

of the specimens followed by skin cracking on both sides and progressed throughout the width of the samples. While when length is much greater than the width the global buckling mode is the dominant collapse mode. The flatwise compression failure of SPU and SPS samples was dominated by foam cell collapse and densification, with no interfacial debonding observed due to strong adhesion between the GFRP skin and foam core.

- The shear test displayed severe damage to the core for both SPS and SRP. The core revealed significant deformation and fracture along planes parallel to the test fixture. The damage is mainly concentrated in the central region of the core. However, skin-core debonding in SRP specimens was slightly reduced compared to SPS, reflecting the positive impact of the reinforced pins on the material's integrity. The core shear stress and shear modulus nearly doubled for SRP compared to SPS, indicating a notable improvement in their shear resistance and stiffness.
- The flexural behavior of SPS and SRP specimens was assessed under static and cyclic loading conditions. A distinct difference in the responses of SPS and SRP specimens under both static and cyclic loading conditions underscores the substantial enhancement in stiffness achieved by incorporating reinforced pins into the sandwich structure. This improvement is particularly evident in a pronounced increase in flexural Young's modulus for the SRP specimens compared to SPS.
- The Ncorr post-processing tool was used to analyze the vertical strain of SPS and SRP specimens under cyclic loading by employing three virtual extensometers positioned at specific points in the support regions. The strain data revealed that the SRP specimen demonstrated a more consistent and gradual increase in strain over time, indicating greater stability, while the SPS specimen underwent significantly higher overall deformation, highlighting a more pronounced material response to cyclic loading.

## Perspectives

- Assess the long-term durability of sandwich composites under varying environmental conditions.
- Explore the design, materials and geometries of reinforced pins to improve load distribution, enhance resistance to shear failure, and boost overall stiffness and performance of sandwich structures.

- Full-scale study of mechanical behavior of sandwich panels with foam core and hybrid reinforced core.
- Numerical modelling and simulation of behavior of tested specimens and full-scale sandwich panels.
- Improve manufacturing technique to optimize the sandwich structures for better performance.
- Investigate methods for recycling GFRP skins and foam cores, focusing on reusability and reducing waste.

## BIBLIOGRAPHY

---

- [1] Kazemian, R., Fanaie, N., Mousavi-bafrouyi, S.M.S., Lee, J. (2024). Experimental investigation on flexural behavior and energy absorption of lightweight sandwich panels with aluminum honeycomb core embedded by thin-ply carbon-glass fibers / epoxy fac ... Experimental investigation on flexural behavior and energy absorptio, Structures, 60(January), pp. 105961, Doi: 10.1016/j.istruc.2024.105961.
- [2] Feng, Y., Qiu, H., Gao, Y., Zheng, H., Tan, J. (2020). Creative design for sandwich structures: A review, Int. J. Adv. Robot. Syst., 17(3), pp. 1–24, Doi: 10.1177/1729881420921327.
- [3] Osa-uwagboe, N., Silberschmidt, V. V., Aremi, A., Demirci, E. (2023). Mechanical behaviour of fabric-reinforced plastic sandwich structures : A state- of-the-art review, J. Sandw. Struct. Mater., 25(5), pp. 591–622, Doi: 10.1177/10996362231170405.
- [4] Aneta, K., Mazur, M., Gajewski, M., Drozd, K., Komorek, A., Przybylek, P. (2016). Sandwich Structured Composites for Aeronautics: Methods of Manufacturing Affecting Some Mechanical Properties, Int. J. Aerosp. Eng., ,.
- [5] Carlsson, L.A., Kardomateas, G.A. (2011). Structural and failure mechanics of sandwich composites, vol. 121.
- [6] Rajak, D.K., Pagar, D.D., Menezes, P.L., Linul, E. (2019). Fiber-Reinforced Polymer Composites :, Polymers (Basel), 11(10),.
- [7] Wei, X., Li, D., Xiong, J. (2019). Fabrication and mechanical behaviors of an all-composite sandwich structure with a hexagon honeycomb core based on the tailor-folding approach, Compos. Sci. Technol., 184, pp. 107878, Doi: 10.1016/j.compscitech.2019.107878.
- [8] Alein, J.S. (2021). THIN SANDWICH COMPOSITES : A REVIEW, XIII(5), pp. 468–73.
- [9] Goda, K., Sreekala, M.S., Malhotra, S.K., Joseph, K., Thomas, S. (2012).Part One Introduction to Polymer Composites. Polymer Composites, Biocomposites, vol. 1, pp. 1–16.
- [10] Wang, R.-M., Zheng, S.-R., Zheng, Y.-P. (2011).Introduction to polymer matrix composites. Polymer Matrix Composites and Technology, Elsevier, pp. 1–548.
- [11] Gu, H., Liu, C., Zhu, J., Gu, J., Wujcik, E.K., Shao, L., Guo, Z. (2018).Introducing advanced composites and hybrid materials. Advanced Composites and Hybrid Materials, pp. 1–5.
- [12] İşmal, Ö.E., Paul, R. (2017).Composite textiles in high-performance apparel. High-Performance Apparel: Materials, Development, and Applications, Elsevier, pp. 377–420.
- [13] Yang, Y., Boom, R., Irion, B., van Heerden, D.J., Kuiper, P., de Wit, H. (2012). Recycling of composite materials, Chem. Eng. Process. Process Intensif., 51, pp. 53–68, Doi: 10.1016/j.cep.2011.09.007.
- [14] Hsissou, R., Seghiri, R., Benzekri, Z., Hilali, M., Rafik, M., Elharfi, A. (2021).



- Polymer composite materials: A comprehensive review, *Compos. Struct.*, 262(December 2020), pp. 0–3, Doi: 10.1016/j.compstruct.2021.113640.
- [15] Park, S.J., Seo, M.K. (2011). *Element and Processing. Interface Science and Technology*, vol. 18, pp. 431–99.
- [16] Karim, M.A., Abdullah, M.Z., Deifalla, A.F., Azab, M., Waqar, A. (2023). An assessment of the processing parameters and application of fibre-reinforced polymers (FRPs) in the petroleum and natural gas industries: A review, *Results Eng.*, 18(March), pp. 101091, Doi: 10.1016/j.rineng.2023.101091.
- [17] Hunt, W.H. (n.d.). *Metal Matrix Composites.*, p. 6.
- [18] Chawla, K.K. (2012). *Composite materials: Science and engineering*, third edition, .
- [19] Kundu, S., Mitra, D., Das, M. (2022). Particulate-Reinforced Composites, Toughened Compos., (September), pp. 55–68, Doi: 10.1201/9780429330575-5.
- [20] Campbell, F.C. (2010). *Structural Composite Materials*, .
- [21] Ikhmayies, S. jamil. (2024). *Advances in Material Research and Technology*, Springer.
- [22] Qureshi, J. (2022). A Review of Fibre Reinforced Polymer Structures, *Fibers*, 10(3), pp. 4–6, Doi: 10.3390/fib10030027.
- [23] Mallick, P.K. (2007). *Fiber-reinforced composites: materials, manufacturing and design*, Taylor & Francis.
- [24] Prakash, S. (2019). Experimental investigation of surface defects in low-power CO<sub>2</sub> laser engraving of glass fiber-reinforced polymer composite, *Polym. Compos.*, 40(12), pp. 4704–15, Doi: 10.1002/pc.25339.
- [25] Rajak, D.K., Wagh, P.H., Linul, E. (2021). Manufacturing technologies of carbon/glass fiber-reinforced polymer composites and their properties: A review, *Polymers (Basel)*, 13(21), Doi: 10.3390/polym13213721.
- [26] Zhang, M., Matinlinna, J.P. (2012). E-Glass Fiber Reinforced Composites in Dental Applications, *Silicon*, 4(1), pp. 73–8, Doi: 10.1007/s12633-011-9075-x.
- [27] Elkafrawy, M., Gowrishankar, P., Aswad, N.G., Alashkar, A., Khalil, A., AlHamaydeh, M., Hawileh, R. (2024). GFRP-Reinforced Concrete Columns: State-of-the-Art, Behavior, and Research Needs, *Buildings*, 14(10), pp. 1–44, Doi: 10.3390/buildings14103131.
- [28] Keller, T., Haas, C., Vallée, T. (2008). Structural Concept, Design, and Experimental Verification of a Glass Fiber-Reinforced Polymer Sandwich Roof Structure, *J. Compos. Constr.*, 12(4), pp. 454–68, Doi: 10.1061/(asce)1090-0268(2008)12:4(454).
- [29] Keller, T., Rothe, J., De Castro, J., Osei-Antwi, M. (2014). GFRP-Balsa sandwich bridge deck: Concept, design and experimental validation, *Proc. 7th Int. Conf. FRP Compos. Civ. Eng. CICE 2014*, , pp. 1–10, Doi: 10.1061/(asce)cc.1943-5614.0000423.
- [30] Correia, J.R., Bai, Y., Keller, T. (2015). A review of the fire behaviour of pultruded GFRP structural profiles for civil engineering applications, *Compos. Struct.*, 127, pp. 267–87, Doi: 10.1016/j.compstruct.2015.03.006.
- [31] Bajpai, P.K., Singh, I. (2019). *Reinforced Polymer Composites Processing*,

- Characterization and Post Life Cycle Assessment, vol. 11, Wiley-VCH.
- [32] Ratna, D. (2022). Recent Advances and Applications of Thermoset Resins, Elsevier.
  - [33] De, B., Bera, M., Bhattacharjee, D., Ray, B.C., Mukherjee, S. (2024). A comprehensive review on fiber-reinforced polymer composites: Raw materials to applications, recycling, and waste management, *Prog. Mater. Sci.*, 146(February), pp. 101326, Doi: 10.1016/j.pmatsci.2024.101326.
  - [34] Suresha, B., Chandramohan, G. (2007). Three-body abrasive wear behaviour of particulate-filled glass – vinyl ester composites, 0, pp. 306–11, Doi: 10.1016/j.jmatprotec.2007.09.035.
  - [35] Sapkota, A. (2021). Fabrication and Investigation of Properties of Carbon Fibre Reinforced Epoxy Polymer Matrix Composites, (March 2020),.
  - [36] Marques, A.T. (2011). Fibrous materials reinforced composites production techniques, Woodhead Publishing Limited.
  - [37] Perna, A.S., Viscusi, A., Astarita, A., Boccarusso, L., Carrino, L., Durante, M., Sansone, R. (2019). Manufacturing of a Metal Matrix Composite Coating on a Polymer Matrix Composite Through Cold Gas Dynamic Spray Technique, *J. Mater. Eng. Perform.*, (February), Doi: 10.1007/s11665-019-03914-6.
  - [38] Frketic, J., Dickens, T., Ramakrishnan, S. (n.d.). Automated Manufacturing and Processing of Fiber-Reinforced Polymer ( FRP ) Composites : An Additive Review of Contemporary and Modern Techniques for Advanced Materials Manufacturing, ,.
  - [39] Zaïri, F., Naït-Abdelaziz, M., Gloaguen, J.M., Bouaziz, A., Lefebvre, J.M. (2008). Micromechanical modelling and simulation of chopped random fiber reinforced polymer composites with progressive debonding damage, *Int. J. Solids Struct.*, 45(20), pp. 5220–36, Doi: 10.1016/j.ijsolstr.2008.05.013.
  - [40] K, D., J, D., Beavers, D. (2013). Effect of f fabricatio on process ses on mec chanical p roperties of glass fib ber reinfo rced p olymer c omposites s for 49 me eter ( 160 f foot ) recre eational ya achts, (201 10),.
  - [41] Kim, S.Y., Shim, C.S., Sturtevant, C., Kim, D.D.W., Song, H.C. (2014). Mechanical properties and production quality of hand-layup and vacuum infusion processed hybrid composite materials for GFRP marine structures, *Int. J. Nav. Archit. Ocean Eng.*, 6(3), pp. 723–36, Doi: 10.2478/IJNAOE-2013-0208.
  - [42] Hatti, P.S., L., S.K., Somanakatti, A.B., Rakshith, M. (2022). Investigation on tensile behavior of glass-fiber reinforced polymer matrix composite with varying orientations of fibers, *Mater. Today Proc.*, 54(xxxx), pp. 137–40, Doi: 10.1016/j.matpr.2021.08.196.
  - [43] Mokhtar, D., Medjahdi, M., Benderdouche, N., Chemrak, M.A., Mechab, B., Bestani, B. (2024). Experimental study of the mechanical and optical properties of glass-polyester fiber composite based on response surface methodology Estudo experimental das propriedades mecânicas e ópticas do composto de fibra de vidro-poliéster com base na metodologia d, *Stud. Eng. Exact Sci.*, , pp. 1383–402, Doi: 10.54021/seesv5n1-071.
  - [44] Hota, G.R.V.S., Vijay, P. V., Abhari, R.S. (2010). Rehabilitation of Railroad Bridges using GFRP composites, *Proc. ASME Jt. Rail Conf. 2010, JRC2010*, 1, pp. 57–64, Doi: 10.1115/JRC2010-36053.

- [45] Coccia, S., Meda, A., Rinaldi, Z., Spagnuolo, S. (2017). Influence of GFRP skin reinforcement on the crack evolution in RC ties, *Compos. Part B Eng.*, 119, pp. 90–100, Doi: 10.1016/j.compositesb.2017.03.048.
- [46] Jabbar, S.A.A., Farid, S.B.H. (2018). Replacement of steel rebars by GFRP rebars in the concrete structures, *Karbala Int. J. Mod. Sci.*, 4(2), pp. 216–27, Doi: 10.1016/j.kijoms.2018.02.002.
- [47] Chen, Y. (2021). Glass Fiber-Reinforced Polymer Composites for Power Equipment, *Polym. Compos. Electr. Eng.*, , pp. 377–417, Doi: 10.1002/9781119719687.ch13.
- [48] Reddy, P.S., Inkulu Anil Kumar, S.S.& D.S. (2020). Failure Analysis of GFRP Composite Reinforced with Semimetals for Marine Applications. *Recent Trends in Mechanical Engineering*, Springer Singapore, pp. 261–280.
- [49] Du, B., Li, Z., Bai, H., Li, Q., Zheng, C., Liu, J., Qiu, F., Fan, Z., Hu, H., Chen, L. (2022). Mechanical Property of Long Glass Fiber Reinforced Polypropylene Composite: From Material to Car Seat Frame and Bumper Beam, *Polymers (Basel)*, 14(9), Doi: 10.3390/polym14091814.
- [50] Noor, A.K., Burton, W.S., Bert, C.W. (1996). Computational models for sandwich panels and shells, *Appl. Mech. Rev.*, 49(3), pp. 155–99, Doi: 10.1115/1.3101923.
- [51] Rheinfrank, G., Norman, W. (1944). Molded glass fiber sandwich fuselage for BT-15 airplane, .
- [52] Vinson, J.R. (2005). Sandwich Structures: Past, Present, and Future. *Sandwich Structures 7: Advancing with Sandwich Structures and Materials: Proceeding of the 7th International Conference on Sandwich Structures*, Aalborg University, Aalborg, Denmark, Springer-Netherlands, pp. 3–12.
- [53] Kausar, A., Ahmad, I., Rakha, S.A., Eisa, M.H. (2023). State-Of-The-Art of Sandwich Composite Structures : Manufacturing — to — High Performance Applications, .
- [54] Chróscielewski, J., Miśkiewicz, M., Pyrzowski, Ł., Sobczyk, B., Wilde, K. (2017). A novel sandwich footbridge - Practical application of laminated composites in bridge design and in situ measurements of static response, *Compos. Part B Eng.*, 126, pp. 153–61, Doi: 10.1016/j.compositesb.2017.06.009.
- [55] Obaid, A.H., Jaafer, A.A. (2022). Experimental investigation of ferrocement sandwich composite jack arch slab, *Asian J. Civ. Eng.*, 23(7), pp. 1155–68, Doi: 10.1007/s42107-022-00467-3.
- [56] Zhang, F., Lu, Z., Wang, D., Fang, H. (2024). Mechanical properties of the composite sandwich structures with cold formed profiled steel plate and balsa wood core, *Eng. Struct.*, 300(December 2023), pp. 117256, Doi: 10.1016/j.engstruct.2023.117256.
- [57] Karthi, N., Gokulkumar, S., Sathish, S., Rajkumar, U.S. (2022). Acoustical behavior of camellia sinensis/ananas comosus fiber based uni-directional corrugated panel for sound damping application, *Mater. Res. Express*, 9(12), pp. 125309, Doi: 10.1088/2053-1591/aca22.
- [58] (2013). *Composite Materials Handbook - Volume 6 Structural Sandwich Composites*, vol. 6.
- [59] Sahu, S.K., Sreekanth, P.S.R., Reddy, S.V.K. (2022). A Brief Review on Advanced

- Sandwich Structures with Customized Design Core and Composite Face Sheet, *Polymers (Basel)*, 14(20), Doi: 10.3390/polym14204267.
- [60] Kausar, A., Ahmad, I., Rakha, S.A., Eisa, M.H. (2023). State-Of-The-Art of Sandwich Composite Structures : Manufacturing — to — High Performance Applications, *J. Compos. Sci.*, , Doi: <https://doi.org/10.3390/jcs7030102> Academic.
  - [61] Andrews, E.W., Gibson, L.J., Ashby, M.F. (1999). Overview No. 132: The creep of cellular solids, *Acta Mater.*, 47(10), pp. 2853–63, Doi: 10.1016/S1359-6454(99)00150-0.
  - [62] Khan, T., Acar, V., Aydin, M.R., Hülägü, B., Akbulut, H., Seydibeyoğlu, M.Ö. (2020). A review on recent advances in sandwich structures based on polyurethane foam cores, *Polym. Compos.*, 41(6), pp. 2355–400, Doi: 10.1002/pc.25543.
  - [63] Gama, N. V., Ferreira, A., Barros-Timmons, A. (2018). Polyurethane foams: Past, present, and future, *Materials (Basel)*, 11(10), Doi: 10.3390/ma11101841.
  - [64] Szycher, M., Szycher, M., Szycher, M. (2021). *Szycher's Handbook of Polyurethanes*, .
  - [65] Cz, S., Bertino, M.F., Ko, J., Str, A., Mas, M. (2020). Industrial Crops & Products Linseed oil as a natural modifier of rigid polyurethane foams, 115(February 2018), pp. 40–51, Doi: 10.1016/j.indcrop.2018.02.019.
  - [66] Prociak, A., Kura, M., Szymon, B., Budny, P. (2018). Industrial Crops & Products Flexible polyurethane foams synthesized with palm oil-based bio-polyols obtained with the use of different oxirane ring opener, 115(February), pp. 69–77, Doi: 10.1016/j.indcrop.2018.02.008.
  - [67] Xu, Z., Tang, X., Gu, A., Fang, Z. (2007). Novel Preparation and Mechanical Properties of Rigid Polyurethane Foam / Organoclay Nanocomposites, , Doi: 10.1002/app.
  - [68] Mohamed, M., Anandan, S., Huo, Z., Birman, V., Volz, J., Chandrashekhara, K. (2015). Manufacturing and characterization of polyurethane based sandwich composite structures, *Compos. Struct.*, 123, pp. 169–79, Doi: 10.1016/j.compstruct.2014.12.042.
  - [69] Sharaf, T.A.M. (2010). Flexural Behaviour of Sandwich Panels Composed of Polyurethane Core and GFRP Skins and Ribs. 2010.
  - [70] Mocian, O., Constantinescu, D.M., Sandu, M., Sorohan, Ș. (2017). Impact response of polyurethane and polystyrene sandwich panels, *Procedia Struct. Integr.*, 5, pp. 653–8, Doi: 10.1016/j.prostr.2017.07.035.
  - [71] Fam, A., Sharaf, T. (2010). Flexural performance of sandwich panels comprising polyurethane core and GFRP skins and ribs of various configurations, *Compos. Struct.*, 92(12), pp. 2927–35, Doi: 10.1016/j.compstruct.2010.05.004.
  - [72] Xie, H., Wan, L., Wang, B., Pei, H., Liu, W., Yue, K., Wang, L. (2020). An Investigation on Mechanical Behavior of Tooth-Plate-Glass-Fiber Hybrid Sandwich Beams, *Adv. Polym. Technol.*, 2020,.
  - [73] Cui, Y., Hao, H., Li, J., Chen, W. (2021). Failure mechanism of geopolymer composite lightweight sandwich panel under flexural and edgewise compressive loads, *Constr. Build. Mater.*, 270, pp. 121496, Doi: 10.1016/j.conbuildmat.2020.121496.
  - [74] Mamalis, A.G., Manolacos, D.E., Ioannidis, M.B., Papapostolou, D.P. (2005). On the



- crushing response of composite sandwich panels subjected to edgewise compression: *Experimental, Compos. Struct.*, 71(2), pp. 246–57, Doi: 10.1016/j.compstruct.2004.10.006.
- [75] Silva, E.H.P. Da., Barros, S. De., Vieira, A.F.C., Costa, R.R.C. Da. (2023). Accelerated Aging on the Compression Properties of a Green Polyurethane Foam : Experimental and Numerical Analysis, (April), Doi: 10.3390/polym15071784.
- [76] Azmi, M.A., Abdullah, H.Z., Idris, M.I. (2013). Properties of polyurethane foam/coconut coir fiber as a core material and as a sandwich composites component, *IOP Conf. Ser. Mater. Sci. Eng.*, 50(1), Doi: 10.1088/1757-899X/50/1/012067.
- [77] Mostafa, A., Shankar, K., Morozov, E.. (2014). Behaviour of PU-foam / glass-fibre composite sandwich panels under flexural static load, *Mater. Struct.*, , Doi: 10.1617/s11527-014-0253-3.
- [78] Tuwair, H., Volz, J., ElGawady, M.A., Mohamed, M., Chandrashekhara, K., Birman, V. (2016). Testing and Evaluation of Polyurethane-Based GFRP Sandwich Bridge Deck Panels with Polyurethane Foam Core, *J. Bridg. Eng.*, 21(1), pp. 04015033, Doi: 10.1061/(asce)be.1943-5592.0000773.
- [79] Sharafi, P., Nemati, S., Samali, B., Bahmani, A., Khakpour, S., Aliabadizadeh, Y. (2018). Flexural and shear performance of an innovative foam-filled sandwich panel with 3-D high density polyethylene skins, *Eng. Solid Mech.*, 6(2), pp. 113–28, Doi: 10.5267/j.esm.2018.3.002.
- [80] Yadav, S.M., Arun, K. V., Basavarajappa, S., Narendranath, S., Kumar, S. (2011). Collapse mechanism of foam cored sandwich structures under compressive load, *Polym. - Plast. Technol. Eng.*, 50(13), pp. 1351–6, Doi: 10.1080/03602559.2011.584237.
- [81] Jahirul, M.I., Rasul, M.G., Schaller, D., Khan, M.M.K., Hasan, M.M., Hazrat, M.A. (2022). Transport fuel from waste plastics pyrolysis – A review on technologies, challenges and opportunities, *Energy Convers. Manag.*, 258, Doi: <https://doi.org/10.1016/j.enconman.2022.115451>.
- [82] Caliskan, U., Apalak, M.K. (2019). Bending impact behaviour of sandwich beams with expanded polystyrene foam core: Analysis, *J. Sandw. Struct. Mater.*, 21(1), pp. 230–59, Doi: 10.1177/1099636216689545.
- [83] Hossain, G.M.I., Hasan, M., Hasan, T., Azhar, A. (2024). Compressive Behavior of Lightweight Sandwich Structures Made of Perlite , Compressive Behavior of Lightweight Sandwich Structures Made of Perlite , Polystyrene and Formica Sheet, (June), pp. 8–14, Doi: 10.2139/ssrn.4854697.
- [84] Chakraborty, S., Reddy, S., Subramaniam, K.V.L. (2021). Experimental evaluation and analysis of flexural response of sandwich beam panels with an expanded polystyrene core, *Structures*, 33(April 2020), pp. 3798–809, Doi: 10.1016/j.istruc.2021.06.088.
- [85] Mocian, O., Mihai, D. (2017). ScienceDirect ScienceDirect Impact response of polyurethane polystyrene sandwich panels Thermo-mechanical modeling of a high pressure turbine blade of an airplane gas turbine engine, *Procedia Struct. Integr.*, 5, pp. 653–8, Doi: 10.1016/j.prostr.2017.07.035.
- [86] Cramer, S., Stojcevski, F., Usma-Mansfield, C. (2023). An Experimental Investigation

- of the Mechanical Performance of EPS Foam Core Sandwich Composites Used in Surfboard Design, *Polymers* (Basel), 15(12), Doi: 10.3390/polym15122703.
- [87] Caliskan, U., Apalak, M.K. (2019). Bending impact behaviour of sandwich beams with expanded polystyrene foam core: Analysis, *J. Sandw. Struct. Mater.*, 21(1), pp. 230–59, Doi: 10.1177/1099636216689545.
  - [88] Ramli Sulong, N.H., Mustapa, S.A.S., Abdul Rashid, M.K. (2019). Application of expanded polystyrene ( EPS ) in buildings and constructions : A review, 47529, pp. 1–11, Doi: 10.1002/app.47529.
  - [89] Giuliani, F., Autelitano, F., Garilli, E., Montepara, A. (2020). Expanded polystyrene (EPS) in road construction: Twenty years of Italian experiences, *Transp. Res. Procedia*, 45(2019), pp. 410–7, Doi: 10.1016/j.trpro.2020.03.033.
  - [90] Tabatabaiefar, H.R., Mansoury, B., Javad, M., Zand, K., Potter, D. (2015). Mechanical properties of sandwich panels constructed from polystyrene / cement mixed cores and thin cement sheet facings, , Doi: 10.1177/1099636215621871.
  - [91] Ahmad, A., Singh, Y. (2021). In-plane behaviour of expanded polystyrene core reinforced concrete sandwich panels, *Constr. Build. Mater.*, 269, pp. 121804, Doi: 10.1016/j.conbuildmat.2020.121804.
  - [92] Dalfi, H.K., Al-obaidi, A. (2025). Effect of core hybridization on the mechanical performance of sandwich composites, *J. Ind. Text.*, 55, pp. 1–18, Doi: 10.1177/15280837251321137.
  - [93] Abdi, B., Azwan, S., Abdullah, M.R., Ayob, A., Yahya, Y., Xin, L. (2014). Flatwise compression and flexural behavior of foam core and polymer pin-reinforced foam core composite sandwich panels, *Int. J. Mech. Sci.*, 88, pp. 138–44, Doi: 10.1016/j.ijmecsci.2014.08.004.
  - [94] Balıkoğlu, F., Demircioğlu, T.K., Yıldız, M., Arslan, N., Ataş, A. (2018). Mechanical performance of marine sandwich composites subjected to flatwise compression and flexural loading: Effect of resin pins, *J. Sandw. Struct. Mater.*, 22(6), pp. 2030–48, Doi: 10.1177/1099636218792671.
  - [95] Yan, L.L., Han, B., Yu, B., Chen, C.Q., Zhang, Q.C., Lu, T.J. (2014). Three-point bending of sandwich beams with aluminum foam-filled corrugated cores, *Mater. Des.*, 60, pp. 510–9, Doi: 10.1016/j.matdes.2014.04.014.
  - [96] Selver, E., Kaya, G. (2019). Flexural properties of sandwich composite laminates reinforced with glass and carbon Z-pins, *J. Compos. Mater.*, 53(10), pp. 1347–59, Doi: 10.1177/0021998318800146.
  - [97] Lei, H., Yao, K., Wen, W., Zhou, H., Fang, D. (2016). Experimental and numerical investigation on the crushing behavior of sandwich composite under edgewise compression loading, *Compos. Part B Eng.*, 94, pp. 34–44, Doi: 10.1016/j.compositesb.2016.03.049.
  - [98] Sayahlatifi, S., Rahimi, G., Bokaei, A. (2021). Experimental and numerical investigation of sandwich structures with balsa core and hybrid corrugated composite/balsa core under three-point bending using digital image correlation, *J. Sandw. Struct. Mater.*, 23(1), pp. 94–131, Doi: 10.1177/1099636218822333.
  - [99] Yungwirth, C.J., O'Connor, J., Zakraysek, A., Deshpande, V.S., Wadley, H.N.G.

- (2011). Explorations of hybrid sandwich panel concepts for projectile impact mitigation, *J. Am. Ceram. Soc.*, 94(SUPPL. 1), pp. s62–75, Doi: 10.1111/j.1551-2916.2011.04501.x.
- [100] Montazeri, A., Bahmanpour, E., Safarabadi, M. (2023). Three-Point Bending Behavior of Foam-Filled Conventional and Auxetic 3D-Printed Honeycombs, *Adv. Eng. Mater.*, , Doi: 10.1002/adem.202300273.
- [101] Djama, K., Michel, L., Gabor, A., Ferrier, E. (2019). Mechanical behaviour of a sandwich panel composed of hybrid skins and novel glass fibre reinforced polymer truss core, *Compos. Struct.*, 215(February), pp. 35–48, Doi: 10.1016/j.compstruct.2019.02.033.
- [102] Aisah, N., Fidyaningsih, R., Utami, W.T., Roseno, S., Rohman, S., Arjasa, O.P., Gustiono, D. (2022). Fabrication and characterization of glass fiber reinforced polymer (GFRP) composite skins. vol. 2708, AIP Publishing.
- [103] Islam, M.R., Arifuzzaman, M., Neon, A.K., Duzzaman, M.S., Islam, M.R. (2020). Flexural Behavior of Sandwich Composite Made of JFRP Honeycomb as Core and GFRP as Skin, *J. Eng. Adv.*, 01(04), pp. 111–5, Doi: 10.38032/jea.2020.04.001.
- [104] Al-fatlawi, A., Jármai, K., Kovács, G. (2021). Optimal design of a fiber-reinforced plastic composite sandwich structure for the base plate of aircraft pallets in order to reduce weight, *Polymers (Basel)*, 13(5), Doi: 10.3390/polym13050834.
- [105] Li, J., Wang, J., Yadav, B.P., Chen, J., Jin, Q., Liu, W. (2020). Flexural behavior of slab-rib integrated bridge decks with GFRP skin and polyurethane foam core, *Adv. Mater. Sci. Eng.*, 2020, Doi: 10.1155/2020/3597056.
- [106] Fang, H., Sun, H., Liu, W., Wang, L., Bai, Y., Hui, D. (2015). Mechanical performance of innovative GFRP-bamboo-wood sandwich beams: Experimental and modelling investigation, *Compos. Part B Eng.*, 79, pp. 182–96, Doi: 10.1016/j.compositesb.2015.04.035.
- [107] Ridlwani, M., Nurgasang, F.A., Riza, R., Syafi'i, N.M. (2022). Mechanical Properties of Sandwich Composite using Glass Fiber Reinforced Polymer as A Skin and 3D Printed Polylactic Acid as A Core, *J. Mech. Eng. Sci. Innov.*, 2(1), pp. 44–54, Doi: 10.31284/j.jmesi.2022.v2i1.2935.
- [108] Xie, H., Fang, H., Cai, W., Wan, L., Huo, R., Hui, D. (2021). Development of an innovative composite sandwich matting with GFRP facesheets and wood core, *Rev. Adv. Mater. Sci.*, 60(1), pp. 80–91, Doi: 10.1515/rams-2021-0016.
- [109] Lukkassen, D., Meidell, A. (2007). Advanced materials and structures and their fabrication processes, vol. 2.
- [110] Atiki, E., Khechai, A., Taallah, B., Feia, S., Almeasar, K.S., Guettala, A., Canpolat, O. (2023). Assessment of flexural behavior of compressed earth blocks using digital image correlation technique: effect of different types of date palm fibers, *Eur. J. Environ. Civ. Eng.*, 0(0), pp. 1–22, Doi: 10.1080/19648189.2023.2245868.
- [111] Bassir, D., Guessasma, S., Zheng, Y., Cai, Y., Salzenstein, P. (2024). Composite characterization using digital image correlation (DIC) approach for stress-strain prediction. *International Conference of Numerical Analysis and Applied Mathematics: Icnam2022*, vol. 3094, p. 230003.

- [112] Casavola, C., Del Core, L., Moramarco, V., Pappaletta, G., Patronelli, M. (2022). Full-field mechanical characterization of polyurethane foams under large deformations by digital image correlation, *Mech. Adv. Mater. Struct.*, 29(24), pp. 3540–55, Doi: 10.1080/15376494.2021.1905915.
- [113] Tekieli, M., De Santis, S., de Felice, G., Kwiecień, A., Roscini, F. (2017). Application of Digital Image Correlation to composite reinforcements testing, *Compos. Struct.*, 160, pp. 670–88, Doi: 10.1016/j.compstruct.2016.10.096.
- [114] Chakraborty, S., Reddy, S., Subramaniam, K.V.L. (2021). Experimental evaluation and analysis of flexural response of sandwich beam panels with an expanded polystyrene core, *Structures*, 33(April 2020), pp. 3798–809, Doi: 10.1016/j.istruc.2021.06.088.
- [115] Hosseini-Toudeshky, H., Navaei, A. (2023). Characterization of elastic modulus at glass/fiber interphase using single fiber composite tensile tests and utilizing DIC and FEM, *Mech. Adv. Mater. Struct.*, 0(0), pp. 1–13, Doi: 10.1080/15376494.2023.2225056.
- [116] Vervloet, J., Tysmans, T., Kadi, M. El., De Munck, M., Kapsalis, P., Itterbeeck, P. Van., Wastiels, J., Hemelrijck, D. Van. (2019). Validation of a numerical bending model for sandwich beams with textile-reinforced cement faces by means of digital image correlation, *Appl. Sci.*, 9(6), Doi: 10.3390/app9061253.
- [117] Hartmann, S., Sguazzo, C. (n.d.). Strain Analysis in Sandwich Structures using Digital Image Correlation 1 Introduction 2 Kinematical Description of Strains, ,.
- [118] Zhang, W., Xu, M., Yuan, T., Li, W., Dai, X., Zhang, Z., Yun, H., Wang, Y. (2023). 3D-digital image correlation for deformation measurement on sandwich structures under low velocity impact, ,.
- [119] Garcia de la Yedra, A., Erro, I., Vivas, J., Zubiri, O., Zurutuza, X., Sommemerhuber, R., Kettner, M. (2024). Applied sciences Acoustic Emission and Digital Image Correlation-Based Study for Early Damage Identification in Sandwich Structures, *Appl. Sci.*, 14(21),.
- [120] Fathi, A., Keller, J.H., Altstaedt, V. (2015). Full-field shear analyses of sandwich core materials using Digital Image Correlation (DIC), *Compos. Part B Eng.*, 70, pp. 156–66, Doi: 10.1016/j.compositesb.2014.10.045.
- [121] (1996).ISO 1172, Plastiques renforcés de verre textile — Préimprégnés, compositions de moulage et stratifiés — Détermination des taux de verre textile et de charge minérale par des méthodes calcination, 1996.
- [122] Blaber, J., Adair, B., Antoniou, A. (2015). Ncorr: Open-Source 2D Digital Image Correlation Matlab Software, *Exp. Mech.*, 55(6), pp. 1105–22, Doi: 10.1007/s11340-015-0009-1.
- [123] Zeroual, A., Bouaziz, A., Dadda, A., Feia, S., Khechai, A., Lamouri, B., El Hajjar, A. (2023). Experimental investigation on the desiccation cracking process in date palm fiber reinforced clayey soil using digital image correlation, *Eur. J. Environ. Civ. Eng.*, 0(0), pp. 1–22, Doi: 10.1080/19648189.2023.2244555.
- [124] (2014).ASTM D638-14 Standard Test Method for Tensile Properties of Plastics, 2014.
- [125] (N.d.). Modified ASTM D695 Compression Test Fixture (Boeing BSS 7260). Available at: <https://wyomingtestfixtures.com/products/compression/modified-astm-d->



- 695-compression-test-fixture-boeing-bss-7260/.
- [126] (2015).ASTM D695–15 Standard Test Method for Compressive Properties of Rigid Plastics, 2015.
  - [127] Instron. (2014). A Review of Current In-Plane Composites Compression Testing Methods & Standards, .
  - [128] British Standards Institution. (1998). BS EN ISO 14125:1998 Licensed, Order A J. Theory Ordered Sets Its Appl., 1998(July 2002), pp. 24.
  - [129] (2012).ASTM C364/364M-07 Standard Test Method for Edgewise Compressive Strength of Sandwich, 2012.
  - [130] (2003).ASTM C 365-00, Standard Test Method for Flatwise Compressive Properties of Sandwich Cores 1, 2003.
  - [131] ASTM. (2000). ASTM C273 (2000) Standard test method for shear properties of sandwich core materials, ASTM, West Conshohocken, 15, pp. 1–4.
  - [132] Barbara, G., Trampczynski, W., Tworzewska, J. (2020). Analysis of Crack Width Development in Reinforced Concrete Beams, Materials (Basel)., , pp. 126–126, Doi: <https://doi.org/10.3390/ma14113043>.
  - [133] Meiramov, D., Ju, H., Seo, Y., Lee, D. (2025). Correlation between deflection and crack propagation in reinforced concrete beams, Meas. J. Int. Meas. Confed., 240(May 2024), pp. 115527, Doi: 10.1016/j.measurement.2024.115527.
  - [134] Casavola, C., Del Core, L., Moramarco, V., Pappaletta, G., Patronelli, M. (2022). Experimental and numerical analysis of the Poisson's ratio on soft polyurethane foams under tensile and cyclic compression load, Mech. Adv. Mater. Struct., 29(28), pp. 7172–88, Doi: 10.1080/15376494.2021.1994061.
  - [135] Biswas, B., Bandyopadhyay, N.R., Sinha, A. (2019).Mechanical and dynamic mechanical properties of unsaturated polyester resin-based composites. Unsaturated Polyester Resins: Fundamentals, Design, Fabrication, and Applications, Elsevier Inc., pp. 407–34.
  - [136] Masmoudi, A., Bouaziz, A., Khechai, A., Zeroual, A., Adimi, Y. (2024). Mechanical analysis of polyester resin using digital image correlation and finite element method, , pp. 1–15, Doi: 10.54021/seesv5n2-326.
  - [137] Masmoudi, A., Khechai, A., Bouaziz, A., Belhi, G., Zeroual, A., Adimi, Y. (2025). Experimental investigation on mechanical behavior of sandwich structures using Digital Image Correlation ( DIC ), Frat. Ed Integrita Strutt., 19(73), pp. 41–58, Doi: 10.3221/IGF-ESIS.73.04.
  - [138] Kim, D. (Dae-W., Hennigan, D.J., Beavers, K.D. (2010). Effect of fabrication processes on mechanical properties of glass fiber reinforced polymer composites for 49 meter (160 foot) recreational yachts, Int. J. Nav. Archit. Ocean Eng., 2(1), pp. 45–56, Doi: 10.2478/ijnaoe-2013-0019.

# LIST OF PUBLICATIONS AND COMMUNICATIONS

---

## International publication

- Masmoudi, A., Bouaziz, A., Khechai, A., Zeroual, A., Adimi, Y., & Belhi, G. (2024). Mechanical analysis of polyester resin using digital image correlation and finite element method. *STUDIES IN ENGINEERING AND EXACT SCIENCES*, 5(2), e9130. <https://doi.org/10.54021/seesv5n2-326>
- Masmoudi, A., Khechai, A., Bouaziz, A., belhi, G., Zeroual, A., Adimi, Y., Experimental investigation on mechanical behavior of sandwich structures using Digital Image Correlation (DIC), *Fracture and Structural Integrity*, 73 (2025) 41-58. <https://doi.org/10.3221/IGF-ESIS.73.04>

## International communication

- Masmoudi, A., Zeroual, A., Bouaziz, A., Khechai, A., Adimi, Y. Mechanical Investigation of UP Resin: Experimental and Numerical Study. The 5th International Conference on Innovative Academic Studies October 10 – 11 2024 Konya/Turkey.
- Masmoudi, A., Zeroual, A., Bouaziz, A., Khechai, A., Adimi, Y. Experimental validation and numerical modeling of polymer mechanics. The 9<sup>th</sup> International Congress On Natural and Engineering Sciences (ICNES 2024), November 22-25-2024.

## National communication

- Masmoudi, A., Zeroual, A., Bouaziz, A., Khechai, A., Adimi, Y. Experimental and numerical investigation on mechanical behavior of thermosetting resin. The Second National Conference of Materials Sciences and Renewable Energy (CMSRE 2024) November, 09-10 Th ,2024/ Relizane, Algeria.
- Masmoudi, A., Zeroual, A., Bouaziz, A., Khechai, A., Adimi, Y. Etude du Comportement Mécanique De Résine Polyester Insaturé Utilisant Corrélation D'image Numérique. The First National Congress on Civil Engineering and Housing of Constantine (N2CEHC 2024)

- ZEROUAL A, MASMOUDI A, BOUAZIZ A, FEIA S, & DADDA A. Comportement de fissuration par dessiccation d'un sol argileux renforcé par des fibres de palmier dattier. The First National Congress on Civil Engineering and Housing of Constantine N2CEHC 2024

## ANNEX. PRODUCT DATASHEETS OF THE MATERIALS USED

### 1. Polyester resin used for skin.

#### Technical Data Sheet



## Polipol 353

Casting type high filler capacity polyester

#### Product Description

Polipol 353 is an orthophthalic, medium-high reactivity, high-quality unsaturated polyester resin for casting applications. Polipol 353 accepts high ratio of fillers such as calcite, aluminum hydroxide and dolomite up to 70-80%. Polipol 353 has very clear color and provides aesthetical results for clear castings of small items.

#### Highlights

- High-quality casting resin
- Low volumetric shrink
- Clear resin color and good casting color
- Good filler wetting
- Accept high filler ratio
- High mechanical test values

#### Typical Liquid Properties

Property	Value	Unit	Test Method
Appearance	Clear	-	-
Color	max.100	Hazen	-
Shelf Life*	6	months	-
Density	1,121	g/cm <sup>3</sup>	ISO 1675

\*See handling and storage conditions.

#### Liquid Specifications

Property	Value	Unit	Test Method
Viscosity <sup>1</sup>	600-800	cP	ISO 2555
Thixotropy	N/A	-	-
Monomer Content	35-38	%	IT 012
Acid Value	20	mg KOH/g	ISO 2114
Gel Time <sup>2</sup>	9-12	min	IT 004

#### Remarks

<sup>1</sup> Viscosity measured at 23 °C with Brookfield DV3T Rheometer (spindle 4, 50 rpm).

<sup>2</sup> Gel time measured at 23°C with 1 ml. Cobalt solution (1% Co conc.) and 1 ml. Mek-p (Butanox M 60 - 9,9 % Active oxygen) added to 100 gr. resin.

#### Customer Support

<http://www.poliya.com/en/>

Finizköy Bulvarı, No:46 Avolar  
34325 İstanbul, Turkey  
T +90 (212) 509 31 90  
F +90 (212) 509 31 94

#### Legal Disclaimer

Information in this document is subject to change without notice. This document is for informational purpose only and provided "as is" without warranty of any kind, whether express or implied, including but not limited to the implied warranties of merchantability, fitness for particular purpose, and non-infringement. Buyer must determine for himself, by preliminary tests or otherwise, the suitability of these products for his purposes. Poliya assumes no responsibility for editorial errors or omissions in this document.

Document Version:

R 01\_Polipol 353-24.01.2019

1

in every part of life...™



## Application and Use

Polipol 353 is suitable for the production of gelcoated artificial marble and sink productions as well as shower trays with addition of fillers (such as calcite, dolomite, aluminum hydroxide) at a high ratio, up to 70-80%. Polipol 353 can also be used for casting of bijouterie items and trinkets without fillers.

Starting formulation for artificial marble production given below; in certain cases, depending on production conditions and casting equipment filler ratio can be higher than 80%.

Sample Artificial Marble Formulation	%
Polijel 213 gelcoat	Film thickness (400-1000 mikron)
Polipol 353	29,30
Calcite/Dolomite	68,37
Cobalt,%6 Sol. (accelerator)	0,03
Mek-P (hardener)	0,30
Color Paste	2,00
Total	100,00

## Mechanical Properties of Cured Resin

### Typical Values of Cast Resin \*

Property	Value	Unit	Test Method
HDT (1.82 MPa)	61	°C	ISO 75-A
HDT (0.45 MPa)	70	°C	ISO 75-B
Tensile Strength	61	MPa	ISO 0527
Modulus of Elasticity in Tensile	3434	MPa	ISO 0527
Elongation at Break, Tensile	2,6	%	ISO 0527
Flexural Strength	115	MPa	ISO 0178
Modulus of Elasticity, Flexural	4083	MPa	ISO 0178
Elongation at Break, Flexural	3,0	%	ISO 0178
Izod Impact Strength	13	kJ/m <sup>2</sup>	ISO 0180
Barcol Hardness	47	-	ASTM-D 2583
Volumetric Shrink	7,6	%	ISO 3521
Water Absorption	0,155	%	ISO 0062

### \*Remarks

Resin casting prepared with addition of accelerator/hardener. Casting allowed to cure 24 hours at 25°C and then oven post cured.

## 2. Epoxy resin used as adhesive.

FICHE TECHNIQUE

01-16



**EPOTEK AUTO-NIVELANT (TRASP)**

Résine auto-nivelant et transparente à base d'époxy Produit spécifique pour sol en résine



### DESCRIPTION

**EPOTEK AUTO-NIVELANT (TRASP)** est une résine auto-nivelant bi-composant à base d'époxy pour la réalisation de sols en résine.

### COMPOSITION

Produits bi-composant à base de résine d'époxy sans solvant, et convenablement formulé pour résister aux rayons UV.

### CARACTÉRISTIQUES GÉNÉRALES

**EPOTEK AUTO-NIVELANT (TRASP)** est spécifique pour la réalisation de sols décoratifs - résine transparente Architectural d'une épaisseur de 2 à 3 mm, caractérisé par une excellente performance chimio-mécanique.

Ce produit est caractérisé par:

Résistance à la circulation piétonnière intense et aux véhicules;

Résistance à la 'usure;

Résistance au contact avec de nombreux produits chimiques à la fois acide et alcaline;

Facilite la décontamination;

Apparence esthétique excellente.

**EPOTEK auto-nivelant** présente de nombreux avantages:

Installation facile et rapide

Auto-nivelant Ne favorise pas le retrait,

**EPOTEK auto-nivelant** s'adapte aux différents types de supports:

Ciment, grès, tuiles, etc.

### CARACTERISTIQUES TECHNIQUES

Couleur.....Transparent  
Résidu sec RAL (en%) .....98 ± 2  
Poids spécifique à 20 °C (A + B) ....1,25 kg / dm<sup>3</sup> ± 0,05  
Poids spécifique à 20 °C (A + B + C) 1,7 kg / dm<sup>3</sup> ± 0,05  
Rapport de mélange en poids A: B .....20: 10  
15: 4,8: 16,2 (A = base, B = durcisseur, C = charge minérale)

Durée de vie (temps de traitement) à 20 °C 30-35 min

Résistance à la compression .....75,5 Mpa

Résistance à la flexion .....25,5 Mpa

Résistance à la traction .....14,0 Mpa

Module d'élasticité (DBV) .....6700 N / mm<sup>2</sup>

Allongement à la rupture (%) .....1,5-1,7

Température d'application.....de +7 °C à +35 °C

Inflammabilité.....non inflammable

### PREPARATION

Les composants sont livrés dans trois emballages séparés:

**A** - base

**B** - Catalyst

Remuer le contenu des composants A et B dans leurs contenants; puis verser le composant B dans le composant A et mélanger pendant 4-5 minutes jusqu'à homogénéisation complète de produits. Une fois bien mélangé, verser dans un récipient propre.

Ne pas utiliser des quantités partielles pour les erreurs de proportions qui causeraient un durcissement défectueux ou incomplet. Le mélange doit toujours être effectué mécaniquement à un faible nombre de tours (pas plus de 600 tours / min).

Après le mélange complet des composants, le produit est prêt à l'emploi, il ne nécessite aucune dilution.

### APPLICATION

Le produit doit être appliqué sur un support sec (pour éviter la formation des bulles et la desquamation de la surface), nettoyé et dégraissé, traité avec apprêt spécial, ancrage époxy sans solvant.

### CONDITIONNEMENT

Composant A = 20 kg (résine)

Composant B = 10 kg (durcisseur)

Page 1/2



#### Siège & Usine :

B.P. 203. Zone Industrielle de Sidi-Bel-Abbès  
Tél. : + 213 (0) 48 70 34 63  
Fax : + 213 (0) 48 70 34 62  
E-mail : info@teknachem.com  
WWW.TEKNACHEM.COM

#### Antenne d'Alger :

Rue de la Soummam lot N° 06 Z.I. Oued Smar Alger  
Tél./Fax : + 213 (0) 23 92 05 62

#### Antenne de Sétif :

Zone d'Activité Artisanale 6<sup>ème</sup> Tranche - Sétif  
Tél. : + 213 (0) 36 93 90 10 - Fax : + 213 (0) 36 93 90 60

Les informations contenues dans la présente fiche technique, bien que représentant le stade le plus avancé de la connaissance, ne dispensent pas l'utilisateur de procéder à des tests préliminaires dans ses propres conditions d'emploi ou à faire appel à l'assistance technique de la société. Par conséquent la **TEKNACHEM ALGERIE SARL** décline toutes responsabilités pour l'emploi inapproprié du produit.





# EPOTEK AUTO-NIVELANT (TRASP)

Résine auto-nivelant et transparente à base d'époxy Produit spécifique pour sol en résine



## CONSERVATION

Sous emballage d'origine et intact, à l'abri de la chaleur excessive, le produit se conserve pendant 12 mois.

## AVERTISSEMENTS

Dans les mesures d'utilisation régulière, le produit est sans danger pour les personnes qui le manipulent. Lors de l'application ne mange pas, ne pas boire et ne pas fumer, utiliser des vêtements de protection tels que des gants, des lunettes et un masque.

A notre connaissance, les informations fournies dans le présent document sont correctes et précises, mais nous ne fournissons aucune garantie, puisque les conditions d'utilisation ne sont pas sous notre contrôle direct.

En cas de doute, il est toujours conseillé d'effectuer des tests préliminaires ou consulter notre service technique.

**Siège & Usine :**

B.P. 203 Zone Industrielle de Sidi-Bel-Abbès

Tél. : + 213 (0) 48 70 34 63

Fax : + 213 (0) 48 70 34 62

E-mail : [info@teknachem.com](mailto:info@teknachem.com)

[WWW.TEKNACHEM.COM](http://WWW.TEKNACHEM.COM)

**Antenne d'Alger :**

Rue de la Soummam lot N° 06 Z.I. Oued Smar Alger

Tél./Fax : + 213 (0) 23 92 05 62

**Antenne de Sétif :**


Zone d'Activité Artisanale 6<sup>ème</sup> Tranche - Sétif


Tél. : + 213 (0) 36 93 90 10 - Fax : + 213 (0) 36 93 90 60

Les informations contenues dans la présente fiche technique, bien que représentant le stade le plus avancé de la connaissance, ne dispensent pas l'utilisateur de procéder à des tests préliminaires dans ses propres conditions d'emploi ou à faire appel à l'assistance technique de la société. Par conséquent la **TEKNACHEM ALGERIE SARL** décline toutes responsabilités pour l'emploi inapproprié du produit.



### 3. Polyurethane foam used as core.

Technical Data Sheet		 The Chemical Company
<b>Elastopor<sup>®</sup> H 2130/38</b>		
Page 1 / 3 Version 02/dw-Elfersiek Date of issue:01.03.2010		
<b>Application</b>		
Polyurethane system for the production of heat-resistant rigid foam according to EN 253. The range of application comprises the insulation of joints, fittings and moulded parts.		
<b>Chemical Characteristics</b>		
<b>Polyol-Component:</b> mixture of polyetherpolyol, stabilizer, catalyst, blowing agent cyclo-pentane <b>Iso-Component:</b> polymeric diphenylmethane diisocyanate (IsoPMDI 92140)		
<b>Supply</b>		
The type of supply for the components will be decided after consultation with our Sales Office.		
<b>Storage, Preparation</b>		
Polyurethane components are moisture sensitive. Therefore they must be stored at all times in sealed, closed containers. The A-component (Polyol) must be homogenised by basic stirring before processing. More detailed information should be obtained from the separate data sheet entitled "Information for in-coming material control, storage, material preparation and waste disposal" and from the component data.		
<b>Processing</b>		
For processing follow the information provided by our technical adviser.		
<b>Possible Hazards</b>		
The B-component (Isocyanate) irritates the eyes, respiratory organs and the skin. Sensitisation is possible through inhalation and skin contact. MDI is harmful by inhalation. On processing these, take note of the necessary precautionary measures described in the Material Safety Data Sheets (MSDSs). This applies also for the possible dangers in using the A-component (Polyol) as well as any other components. See also our separate information sheet "Safety- and Precautionary Measures for the Processing of Polyurethane Systems." Use our Training Programme "Safe Handling of Isocyanate."		
<b>Waste Disposal</b>		
More detailed information is provided in our country-specific pamphlet.		
<b>Consumer articles, medical products</b>		
There are national and international laws and regulations to consider if it is intended to produce consumer articles (e.g. articles that necessitate food or skin contact, toys etc.) or medical objects out of BASF Polyurethanes GmbH products. Where these do not exist, the current legal requirements of the European Union for consumer articles as well as medical products should be sufficient. Consultation with our Sales Office and our Ecology and Product Safety Department is strongly recommended.		





## Elastopor<sup>®</sup> H 2130/38

Page 2 / 3  
Version 02/dw-Elfersiek  
Date of Issue 01.03.2010



### Component Data

	Unit	Polyol-Comp	Iso-Comp.	Method
Density (20 °C)	g/cm <sup>3</sup>	1.07	1.24	G 133-08
Viscosity (20 °C)	mPa·s	950	300	G 133-07
Shelf life	days	90	180	AA S-10-03 22.011

### Processing Data

#### Cup Test:

	Unit	Value	Method
Component temperature	°C	20	
Quantity	g	A = 26.5 B = 42.4	
Mixing ratio		A : B = 100 : 160	
Stirring time	s	10	
Cream time	s	52	G 132-01
String time	s	252	G 132-01
Rise time	s	358	G 132-01
Density, free rise	kg/m <sup>3</sup>	50	G 132-01

## Elastopor<sup>®</sup> H 2130/38

Page 3 / 3  
Version 02/dw-Elfersiek  
Date of Issue 01.03.2010



### Physical Properties

	Unit	Measured value	Method
Specimen produced by means of high pressure machine (p = 150 bar).			
Density / core	kg/m <sup>3</sup>	60	DIN EN ISO 845
Compressive stress	N/mm <sup>2</sup>	0.40	DIN 53 421
Compression	%	7	DIN 53 421
Closed cells	%	90	ISO 4590
Water absorption	Vol.-%	5	EN 253
Thermal lifetime (CCOT)	°C	161 test report MPA No. 20050724/L/3/D	EN 253
Thermal conductivity	mW/m·K	27.1 test report IMA No. B 85/5-1	EN 253

® = registered trade mark of BASF

The data contained in this publication is based on our current knowledge and experience. In view of the many factors that may affect processing and application of our product, this data does not relieve processors from carrying out their own investigations and tests; neither does this data imply any guarantee of certain properties, or the suitability of the product for a specific purpose. Any descriptions, drawings, photographs, data, proportions, weights etc. given herein may change without prior notice and do not constitute the agreed contractual quality of the product. It is the responsibility of the recipient of our products to ensure that any proprietary rights and existing laws and legislation are observed. (Date of publication).

**BASF Polyurethanes GmbH**

Rheinstraße 1140  
44139 Dortmund  
Germany

Tel.: +49 (0) 5443/12-0

Fax: +49 (0) 5443/12-2474  
E-Mail: [pu-hartschaum@basf.com](mailto:pu-hartschaum@basf.com)  
Internet: [www.pu.basf.eu](http://www.pu.basf.eu)

